

DEVELOPMENT OF A NOVEL RADIATION DOSIMETER:
THE STEMLESS PLASTIC SCINTILLATION DETECTOR

by

M. Allan Hupman

Submitted in partial fulfillment of the requirements
for the degree of Doctor of Philosophy

at

Dalhousie University
Halifax, Nova Scotia
August 2021

© Copyright by M. Allan Hupman, 2021

Table of Contents

List of Tables	vii
List of Figures	vii
Abstract	xii
List of Abbreviations and Symbols Used	xiii
Acknowledgements	xvii
Chapter 1 Introduction	1
1.1 Preamble	1
1.2 Radiation Therapy Physics Background	2
1.3 Photon and Electron Interactions with Matter	5
1.3.1 Photon Interactions	5
1.3.2 Electron Interactions	11
1.3.3 KERMA and Absorbed Dose	13
1.4 Small Field Dosimetry	18
1.4.1 Rationale for using small fields in radiation therapy	18
1.4.2 What Constitutes a Small Field?	19
1.4.3 Field Output Correction Factors	22
1.5 Detecting Radiation	23
1.5.1 Ideal Dosimeter Characteristics	23
1.5.2 Currently Used Detectors	25
1.6 Scintillator Physics	32
1.6.1 Scintillation Light	32

1.6.2	Quenching of Scintillation Light	34
1.6.3	Cerenkov Radiation	36
1.6.4	Fluorescence of Optical Fiber	39
1.7	Organic Photodiodes	39
1.7.1	Signal Generation	40
1.7.2	Photodiode Architecture	41
1.7.3	P3HT/PCBM BHJ Photodiode	42
1.7.4	Operating Characteristics of Organic Photodiodes	42
1.8	Detector Design and Motivation	43
1.9	Research Objectives	46
Chapter 2	Methods	49
2.1	Stemless Plastic Scintillator Detector (SPSD) Fabrication Techniques	50
2.1.1	Substrate Preparation and ITO Etching	50
2.1.2	Spin Coating	50
2.1.3	Physical Vapour Deposition	51
2.1.4	Full Fabrication Process	53
2.1.5	Scintillator Preparation	54
2.2	Detector Setup	55
2.2.1	Measurement of Detectors	55
2.2.2	Extraction of Photocurrent	56
2.3	Irradiation Setup	58
Chapter 3	Manuscript 1: Radiation Induced Photocurrent in the Active Volume of P3HT/PCBM BHJ Photodiodes	64
3.1	Prologue	64
3.2	Abstract	64

3.3	Introduction	65
3.4	Methods	67
3.4.1	Fabrication of Diodes	67
3.4.2	Irradiation Setup	69
3.4.3	Photocurrent Extraction	70
3.5	Results	72
3.6	Discussion	77
3.7	Conclusion	81
Chapter 4	Manuscript 2: Method for the Differentiation of Radiation-Induced Photocurrent from Total Measured Current in P3HT/PCBM BHJ Photodiodes	83
4.1	Prologue	83
4.2	Abstract	84
4.3	Methods Details	84
4.3.1	Introduction	84
4.3.2	Device Fabrication	85
4.3.3	Extraneous Signal	86
4.3.4	Correction Method	87
4.3.5	Validation of Method and Quantification of Compton Current	91
4.3.6	Signal Change with Device Thickness	93
4.3.7	Suggestions to Reduce Compton Current	94
4.4	Conclusion	95
Chapter 5	Manuscript 3: Fabrication and Characterization of a Stemless Plastic Scintillation Detector	96

5.1	Preamble	96
5.2	Abstract	96
5.3	Introduction	98
5.4	Methods	100
	5.4.1 SPSD Fabrication	100
	5.4.2 SPSD Characterization	101
5.5	Results	104
	5.5.1 Linearity	104
	5.5.2 Dose Per Pulse	104
	5.5.3 Output Factors	105
	5.5.4 Output Factors with non-scintillation signal subtracted	106
	5.5.5 PDD	107
	5.5.6 Energy Dependence	107
	5.5.7 Impact of Cerenkov radiation	110
5.6	Discussion	110
5.7	Conclusion	113
5.8	Acknowledgements	114
Chapter 6	Manuscript 4: Measuring Small Field Profiles and Output Factors with a Stemless Plastic Scintillator Array	115
6.1	Preamble	115
6.2	Abstract	115
6.3	Introduction	117
6.4	Methods	118
6.5	Results	123

6.6	Discussion	126
6.7	Conclusion	130
6.8	Acknowledgements	130
Chapter 7	Conclusion	131
7.1	Summary	131
7.2	Future Work	134
7.3	Conclusions	137
	Bibliography	138
	Appendix Appendix A Copyright Permission	149
A.1	Permission for: Radiation Induced Photocurrent in the Active Volume of P3HT/PCBM BHJ Photodiodes	149
A.2	Permission for: Method for the Differentiation of Radiation-Induced Photocurrent from Total Measured Current in P3HT/PCBM BHJ Photodiodes	151
A.3	Permission for: Fabrication and Characterization of a Stemless Plastic Scintillation Detector	153

List of Tables

I Common detector types and their characteristics. 29

List of Figures

1.1	Mass energy absorption coefficient ratio of various materials to water.	3
1.2	Schematic of the photoelectric effect. An incident photon is absorbed and transfers all its energy to an orbital electron, which results in a photoelectron with kinetic energy (T) equal to the incident photon energy minus the binding energy (E_b).	6
1.3	Mass attenuation coefficient of water, silicon, and lead as a function of energy.	8
1.4	Schematic of the Compton effect.	9
1.5	A schematic of pair production.	9
1.6	Mass attenuation coefficients for water.	10
1.7	Inelastic collisions of an incident electron with an orbital electron resulting in either excitation (left) or ionization (right).	12
1.8	Schematic of a Bremsstrahlung photon being created.	13
1.9	Stopping power ratio of a few materials to that of water.	14
1.10	Depiction of an incident photon on a volume, V	17
1.11	Schematic of source occlusion effect.	21
1.12	Energy levels of an organic molecule.	34
1.13	The angle the Cerenkov radiation is emitted depends on the velocity of the charged particle and the index of refraction of the medium.	38
1.14	Various architectures of organic photodiodes.	42
1.15	I-V curve of a typical photodiode in the dark and a typical photodiode while illuminated.	44
1.16	a) The mass attenuation coefficient ratio of several materials to that of water.	45
2.1	Spin coating is a technique for evenly depositing a thin film of material.	51

2.2	Physical vapour deposition is a technique used to deposit a material onto a substrate in a precise pattern.	52
2.3	a) A photo of the photodiode.	54
2.4	a) A photo of the polystyrene (PS) device.	55
2.5	a) On the left is a picture of the SPSD.	56
2.6	a) Alligator clips attached to a couple wires connected to a single SPSD device.	57
2.7	On the left is a picture of the orthovoltage unit setup for irradiations using kV photon beams.	59
2.8	On the left is a picture of the setup used to irradiate our devices with a TrueBeam Linac.	59
2.9	Calibration for converting percent colour to dose for each colour channel of red, green, and blue.	63
3.1	The top left shows a schematic of a Linac with the device placed at depth by placing solid water on top of the device. . .	71
3.2	Schematic diagram of bulk heterojunction (BHJ) diode with electrometers connected.	72
3.3	The average current collected from the BHJ diodes (~200 nm thick) and the PS devices (~220 nm thick) was measured at various dose rates and showed a linear increase indicating there was no dependence of average dose rate.	73
3.4	The absolute photocurrent flowing through each electrode as a function of dose rate was found by subtracting the average current flowing through the PS devices from each of the four BHJ diodes.	74
3.5	The total current flowing through the aluminum electrode for a BHJ diode when irradiated at 600 cGy/min for 100 s.	75
3.6	The charge collected by the diode irradiated with 1 Gy and normalized at an energy of 6 MV.	76
3.7	The range of sensitivities of four BHJ diodes are plotted for three thicknesses.	77

3.8	The dose per pulse was varied by varying the SSD between 80-125 cm and the charge normalized to an SSD of 95 cm.	78
3.9	The output factor was measured for a 6 MV photon beam and compared to ion chamber measurements.	79
3.10	Schematic of BHJ and PS device fabricated side by side to allow the measurement of photocurrent with a single measurement.	82
4.1	Schematic diagrams of the BHJ photodiodes (left) and PS control devices (right).	87
4.2	Picture of the device holder with and without the top to allow easy electrical contact.	88
4.3	Schematic showing the two circuits used for the correction method.	90
4.4	The current is plotted as a function of the field size for the bulk heterojunction (BHJ) photodiode, polystyrene (PS) device, and the corrected current (PS current subtracted from BHJ).	92
4.5	The percent of the total current comprised of Compton current (PS current divided by BHJ current from figure 4) is plotted as a function of field size.	93
4.6	The output factor (detector response normalized to a 10x10 cm ² field size) was measured for a 6 MV photon beam and compared to ion chamber measurements.	94
4.7	Current measured for three different thicknesses for the BHJ diode and the PS device.	95
5.1	On the left is a schematic representation of the layers making up the stemless plastic scintillation detector (SPSD).	102
5.2	A schematic representation of the setup used to irradiate the SPSPD with 6 and 10 MV photon beams (left) and using 100 kVp, 180 kVp, and 300 kVp photon beams (right).	103
5.3	The charge collected as a function of dose for the three SPSPDs.	105
5.4	The dose per pulse was measured by varying the SSD from 80 cm to 125 cm and normalizing to 95 cm SSD.	106

5.5	a) Output factors for the five SPSDs are plotted.	107
5.6	Output factors for the five SPSDs are plotted after the current measured using a PS device was subtracted.	108
5.7	PDDs with the five SPSDs compared to an ion chamber for 6 MV (left) and 10 MV (right).	108
5.8	The energy dependence was observed by irradiating with 100 kVp, 180 kVp, 300 kVp as well as 6 MV and 10 MV.	109
5.9	Directional dependence measured using a 16 MeV electron beam with the large scintillators with and without the use of reflective tape on the scintillator and compared to measurements with a diamond detector.	110
6.1	a) Picture of the photodiode array with the square (5 x 5 cm ²) and 5 mm thick scintillator placed on top.	120
6.2	The charge (uncorrected) is plotted as a function of device location for an irradiation of 200 cGy using a 10 x 10 cm ² field size.	123
6.3	The charge (uncorrected) collected for each pixel is plotted when irradiated with 200 MU for field sizes of a) 0.5 x 0.5 cm ² b) 1 x 1 cm ² and c) 2 x 2 cm ²	124
6.4	The signal is normalized to the center pixel for each data point is plotted for field sizes of a) 0.5 x 0.5 cm ² b) 1 x 1 cm ² and c) 2 x 2 cm ²	125
6.5	Output factors are plotted for field sizes ranging from 0.5 x 0.5 cm ² to 25 x 25 cm ² on the left and 0.5 x 0.5 cm ² to 4 x 4 cm ² on the right.	127

Abstract

Radiation detectors are fundamental tools for the quantitative characterization of therapeutic fields of ionizing radiation. Dosimetry measurements aim to quantify the amount of energy deposited in the body (dose). Therefore, an ideal detector would respond to radiation the same way the human body does. However, the fact that most radiation detectors are not tissue equivalent poses a major challenge. Organic electronics are attractive candidates for radiation detectors due to their potential to be made flexible, configuration highly customizable, wide selection of materials, and tissue equivalence. In this thesis we investigate a novel detector (stemless plastic scintillation detector - SPSD), which couples an organic photodiode to a plastic scintillator. Plastic scintillation detectors (PSDs) offer characteristics that are ideal for the measurement of small fields (high spatial resolution, real-time measurements, tissue equivalence, etc.). However, PSDs suffer from Cerenkov radiation (created in the optical fiber) contaminating the signal and must be corrected. The SPSD detector eliminates the need for an optical fiber to carry the signal. Such a detector could have the advantages of a PSD, while removing the main drawback.

A series of four manuscripts form the basis for this thesis. The first manuscript showed an organic photodiode had potential as a radiation detector directly (linearity with dose rate and output factors agreed with a commercial detector). The second explained and validated a novel method for the correction of an extraneous signal (Compton current) in organic photodiode detectors. The third manuscript investigated a single-element SPSD, which was fabricated by coupling an organic photodiode to an organic scintillator. The SPSD was characterized by measuring various dependencies of the detector including: instantaneous dose rate dependence, energy dependence, directional dependence, and linearity with dose. Furthermore, Cerenkov radiation was shown to be minimal and the directional dependence it caused could be effectively eliminated by using reflective tape. The dependencies were encouraging for use as a detector. The culmination of the work was the fourth manuscript, which presented the fabrication of a 1D array SPSD, which demonstrated the accurate measurement of small field profiles and output factors.

List of Abbreviations Used

Abbreviations

1D	One-Dimensional
2D	Two-Dimensional
3D	Three-Dimensional
AAPM	American Association of Physicists in Medicine
Al	Aluminum
BHJ	Bulk Heterojunction
CSDA	Continuous Slowing Down Approximation
DI	Deionized
DNA	Deoxyribonucleic acid
EA	Electron Affinity
EQE	External Quantum Efficiency
HCl	Hydrochloric acid
IA	Ionization Potential
IAEA	International Atomic Energy Agency
ICRU ments	International Commission on Radiation Units and Measure-
IMRT	Intensity Modulated Radiotherapy
Inc.	Incorporated
IV	Current-Voltage
KERMA	Kinetic Energy Released in the Medium
KeV	Kilo Electron-Volt

KV	Kilovoltage
LiF	Lithium Fluoride
Linac	Linear Accelerator
LUT	Look Up Table
MeV	Mega Electron-Volt
MLC	Multileaf Collimator
MOSFET	Metal-Oxide-Semiconductor Field-Effect Transistor
MV	Megavoltage
OSLD	Optically Stimulated Luminescent Dosimeter
P3HT	Poly(2-hexylthiophene-2,5-diyl)
PCBM	Phenyl-C61-Butyric Acid Methyl Ester
PCE	Power Conversion Efficiency
PDD	Percent Depth Dose
PEDOT:PSS	Poly (3,4-ethylenedioxythiophene) Polystyrene Sulfonate
PET	Polyethylene Terephthalate
PS	Polystyrene
PSD	Plastic Scintillation Detector
PVT	Polyvinyl Toluene
QA	Quality Assurance
SABR	Stereotactic Ablative Radiotherapy
SMU	Source Measurement Unit
SPSD	Stemless Plastic Scintillation Detector
SRS	Stereotactic Radiosurgery
SRT	Stereotactic Radiotherapy
SSD	Source-to-Surface Distance

TG	Task Group
TLD	Thermoluminescent Dosimeter
TRS	Technical Report Series
VMAT	Volumetric-Modulated Arc Therapy

Symbols

ϵ	Energy Imparted
ϵ_{tr}	Energy Transferred
λ	Wavelength
κ/ρ	Pair Production mass attenuation coefficient
σ_R/ρ	Rayleigh mass attenuation coefficient
σ/ρ	Compton mass attenuation coefficient
τ/ρ	Photoelectric mass attenuation coefficient
c	Speed of Light
D	Dose
D_{Det}	Dose to Detector
D_{med}	Dose to medium
E	Energy
E_{Th}	Threshold Energy
E_b	Binding Energy
$h\nu$	Photon Energy
I	Current
I_L	Illumination Current
I_{SC}	Short-Circuit Current
K	KERMA
kB	Birks Constant

K_c	Collision KERMA
K_r	Radiative KERMA
L	Fluorescent Energy Emitted
$m_o c^2$	Rest Mass Energy
n	Index of Refraction
$N(Q)$	Detector Correction Factor
R	Radiant energy
RS	Relative Slope
S	Scintillation Efficiency
T	Kinetic energy
Z	Atomic Number

Acknowledgements

There are many people who have contributed both directly and indirectly to the completion of this thesis over the past four years.

First, thank you to Dr. Alasdair Syme for guiding me through every step of this process. I appreciate that your door was always open and that you answered any and all questions. I have learned so much from you.

Thank you to Dr. Ian Hill for all the time you have spent helping me. I value the insights and guidance you have given me.

I am grateful to my committee members, Dr. Thalath Monajemi and Dr. Mike Sattarivand for their time, feedback, and support of the work.

Thank you to all my fellow grad students (in Medical Physics and in the lab) for the various things that you have taught me and for making this a much more fun experience.

I would like to thank my friends for the much needed distractions and fun times.

To Dad, Mom, Courtney, and Brianna, I am grateful for your love, support, and encouragement. To the rest of my family, thank you for the immeasurable support and the unwavering confidence in me.

Lastly, and most importantly, I want to thank my wife, Maddy, for your love, encouragement, understanding, patience, and so much more. You have helped me more than you know.

Chapter 1

Introduction

1.1 Preamble

This thesis describes a body of work in which organic electronic devices were studied in the context of radiation dosimetry. The work resulted in the development of a new class of detector that we have called the stemless plastic scintillation detector - SPSD. This detector is defined by the coupling of an organic scintillator to an organic photodiode. The SPSD maintains the well-documented benefits of plastic scintillation detectors (PSDs), while eliminating their greatest shortcoming: the contaminating Cerenkov light signal produced in the optical fiber stem of conventional PSDs.

In each of the major bodies of work in this thesis, parts of the detector (photodiode, electrical contacts, scintillator) are evaluated for their contribution to signal generated by the detector. The aim of the work is to create an array detector capable of accurately measuring profiles and output factors of small radiation fields in real-time.

This research has direct application for the improvement of radiation therapy. Recent advances in technology have allowed highly focused treatments that make use of small fields, which use large doses per fraction and steep dose gradients outside the target volume. To ensure an effective treatment and the safe use of these techniques, accurate measurements used to characterize the fields are essential. An SPSD array could be a valuable tool to ensure the safe and accurate delivery of small radiation fields.

1.2 Radiation Therapy Physics Background

Ionizing radiation is widely used for the benefit of society in diverse applications such as: airport security, nuclear power, food safety, medical imaging, radiotherapy, and others. The use of ionizing radiation for these purposes is not without risk, however, as ionizing radiation is a known carcinogen and can cause other serious injuries or death if not used appropriately. The deleterious effects of radiation are primarily driven by the nature of the energy transfer process in a biological medium; in particular, its ability to disrupt critical molecular bonds – particularly in cellular DNA [1].

Approximately half of all cancer patients should receive some form of radiotherapy as part of their treatment [2]. Radiotherapy represents a balancing act between delivering a radiation dose large enough to a target to produce a high probability of controlling the disease progression and not too large to incur a significant risk of severe complications to the surrounding healthy tissues. Consequently, the detection and accurate quantification of fields of ionizing radiation are required for its safe use.

Radiation dosimetry is the determination of the absorbed dose (a concept explored in greater detail below) [3]. Dosimeters are the instruments used to perform dosimetry measurements. In clinical settings, dosimetry measurements are intended to quantify the amount of energy deposited in the human body, or a surrogate for the body, such as water. A major challenge in radiation dosimetry arises from the fact that most radiation detectors are not tissue (or water) equivalent. The photon cross section ratio of various materials to that of water are shown in figure 1.1. The materials shown represent common materials used for dosimeters (air for ionization chambers, carbon for diamond detectors, LiF for thermoluminescent dosimeters (TLD), polyvinyl toluene for organic scintillators, and silicon for

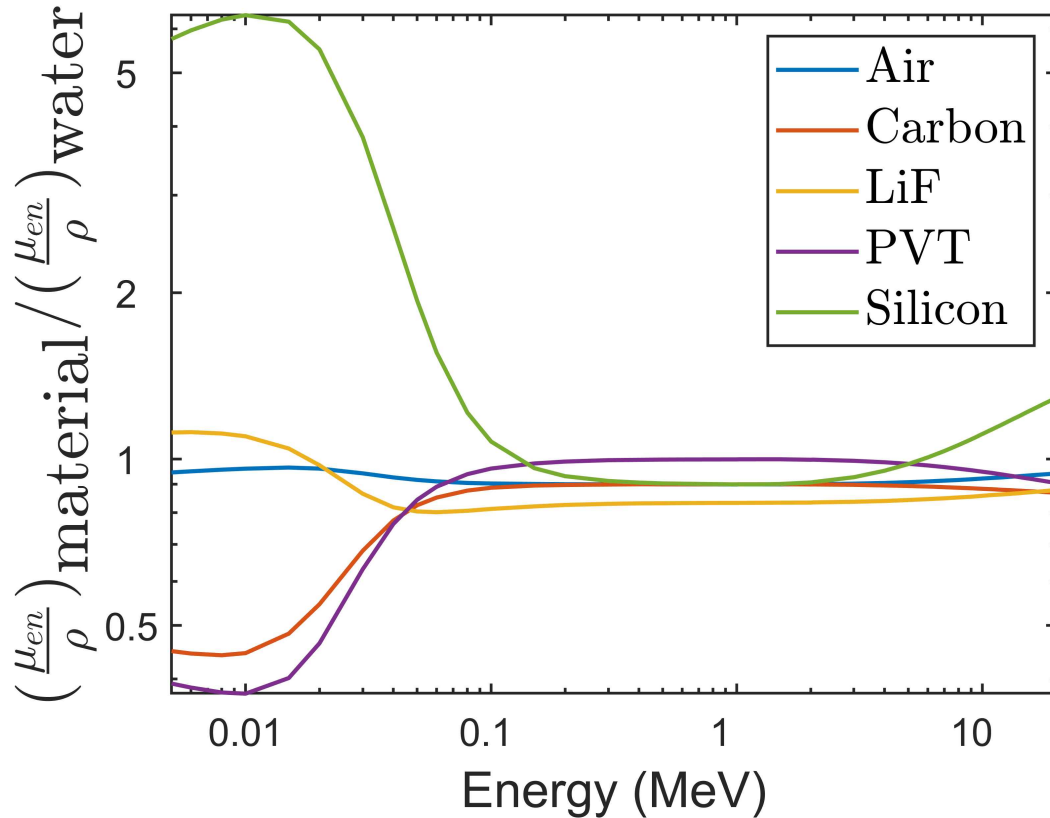


Figure 1.1: Mass energy absorption coefficient ratio of various materials to water. The materials are the active volume of common dosimeters. Air for ionization chambers, carbon for diamond detector, LiF for TLDs, polyvinyl toluene for organic scintillators, and silicon for MOSFETs and diodes. Data retrieved from NIST [4].

MOSFETs and diodes). The presence of a radiation dosimeter in a tissue-equivalent medium (e.g. a water tank) then perturbs the radiation field and introduces uncertainties to the determined value of the absorbed dose. It is often the ionization process itself that forms the basis of the measured signal in a radiation detector and differences in composition between the detector and the body can change the magnitude of the ionization signal.

The perturbation caused by the presence of the detector can be corrected for using Monte Carlo simulations. The correction factor is calculated using two simulations. In one simulation the dose to the detector (D_{Det}) for a given radiation

quality Q (energy), for a setup is determined. In the second simulation the detector is removed and the dose to medium in the absence of the detector D_{med} , is determined. A correction factor $N(Q)$ can then be calculated using the equation:

$$N(Q) = \left(\frac{D_{med}}{D_{Det}} \right)_Q \quad (1.1)$$

The Monte Carlo calculated correction factor is used to correct a measurement using the detector [5]. This is done by multiplying the factor $N(Q)$ by the measured signal to find the actual dose in absence of the detector (i.e. the dose to water or tissue can be determined). One of the challenges of the simulations is that the correction factor can differ significantly due to small deviations in detector design, making it very important to have the exact dimensions and composition of the detector [6]. Furthermore, the correction factor for a detector can differ depending on the irradiation setup parameters (field size, depth of detector, beam quality, etc.). Therefore, it would be preferable to find a detector that does not perturb the beam and thus have a correction factor of 1 for every setup.

A non-exhaustive list of the applications of dosimeters includes: patient specific dose verifications, commissioning of radiotherapy machines (linear accelerators (linacs), Cobalt-60 units, etc.), routine quality assurance (QA) measurements to ensure machine stability over time, and occupational dose monitoring.

There are many types of dosimeters that are suitable for particular tasks. A few of the commonly utilized detectors include: ionization chambers (commissioning and QA), TLDs (brachytherapy, diagnostic radiology, and personal dosimetry), optically stimulated luminescent dosimeters (OSLDs) (surface dosimetry, brachytherapy, and personal dosimetry), film (2D dose distributions, brachytherapy, and QA), diodes (electron beam dosimetry and in vivo dosimetry), and MOSFETs (in vivo dosimetry).

In the subsequent sections a brief description of photon and electron interactions is provided to illustrate how radiation interactions in various materials compares to water to show why our SPSSD design could be advantageous. Following that KERMA and absorbed dose are explained.

1.3 Photon and Electron Interactions with Matter

1.3.1 Photon Interactions

The four most common photon interactions relevant in diagnostic imaging and radiotherapy are: Rayleigh scattering, photoelectric effect, Compton scatter, and pair production. Each will be discussed briefly, but a more detailed description can be found elsewhere [3].

Rayleigh scattering is an elastic process, meaning that no energy is lost by the photon when it scatters. The oscillating electric field of the photon acts on particles within the medium, causing them to oscillate at the same frequency. The particle becomes a radiating dipole and the resulting radiation is seen as scattered light. The mass attenuation coefficient for Rayleigh scattering, σ_R/ρ , depends on the atomic number through which the material is travelling Z , and the energy of the photon, $h\nu$, as:

$$\frac{\sigma_R}{\rho} \propto \frac{Z}{(h\nu)^2} \quad (1.2)$$

The photoelectric effect occurs when a photon interacts with an atom that contains orbital electrons with binding energy less than the incident photon (figure 1.2). The atom absorbs the photon energy and then releases an orbital electron (most often an inner shell electron) with kinetic energy of the photon energy minus the binding energy of the electron:

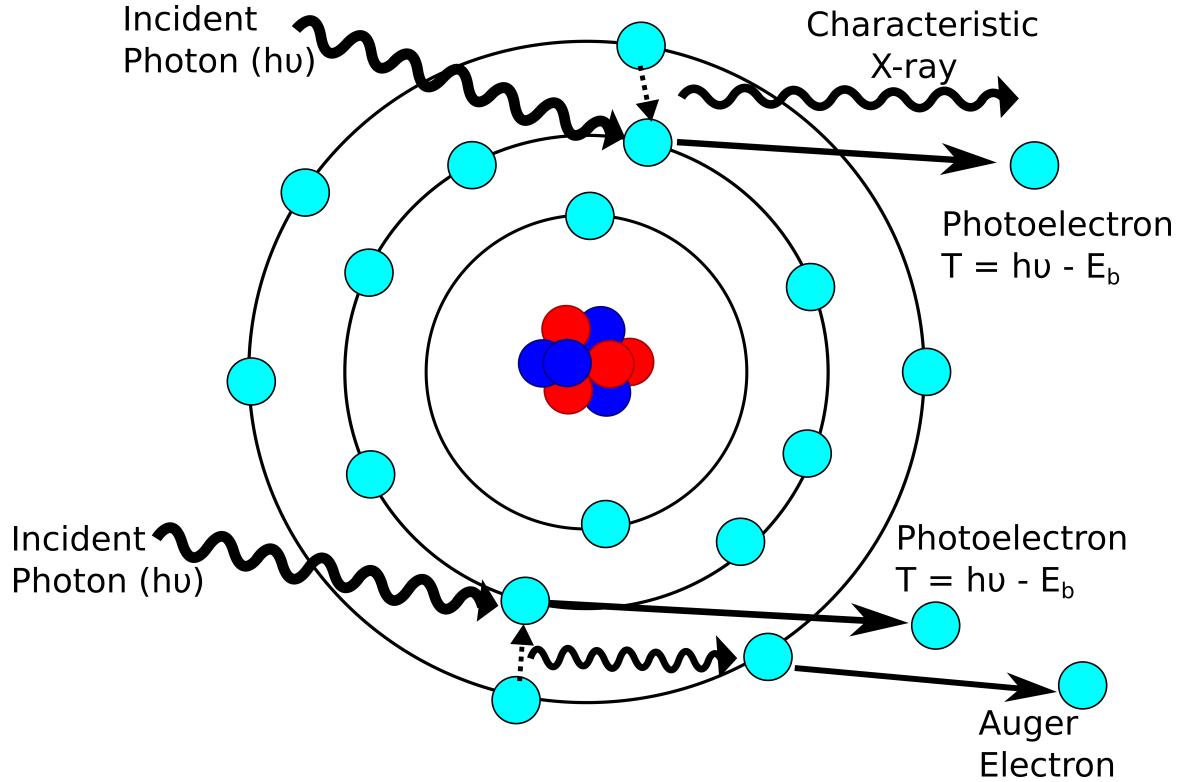


Figure 1.2: Schematic of the photoelectric effect. An incident photon is absorbed and transfers all its energy to an orbital electron, which results in a photoelectron with kinetic energy (T) equal to the incident photon energy minus the binding energy (E_b). This results in a vacancy, which is filled by an outer shell electron, which is accompanied by either the emission of an outer shell electron (Auger electron) or a characteristic X-ray.

$$T = h\nu - E_b \quad (1.3)$$

Where T is the kinetic energy of the resulting electron, E_b is the binding energy, and $h\nu$ is the energy of the incoming photon.

The vacancy left by the electron is filled with another electron from a higher energy shell, which is accompanied by the emission of an outer shell electron known as an Auger electron or the emission of a characteristic X-ray whose energy is given by the difference in the binding energies of the outer and inner shells. The mass attenuation coefficient for the photoelectric effect, τ/ρ , depends on the atomic number

of the medium and the incident photon energy as:

$$\frac{\tau}{\rho} \propto \frac{Z^n}{(h\nu)^m} \quad (1.4)$$

Where the value of n ranges from ~ 3 at 0.1 MeV and rises to ~ 3.6 at 3 MeV and m ranges from ~ 3 at 0.1 MeV and decreases to ~ 1 at 5 MeV (Attix 2008). Below approximately 0.1 MeV where the photoelectric effect is the most dominant n and m are both ~ 3 . At kV energies the mass attenuation coefficients between water and silicon or lead have large discrepancies largely due to the differences in atomic numbers (figure 1.3). Discontinuities in the photon cross-section arise at the binding energies for each energy shell (known as an absorption edge).

Compton scatter occurs when a photon has a much greater energy than the binding energy of the electron. The photon gives up some of its energy to the electron and scatters (figure 1.4). The Compton mass attenuation coefficient, σ/ρ , depends on the electron density of the medium:

$$\frac{\sigma}{\rho} \propto \sigma_e \quad (1.5)$$

Where σ_e is the electron density of the medium. At MV energies where the Compton effect is the dominate interaction type, there is very little difference between the mass attenuation coefficients of water to either silicon or lead (showing that it is independent of the atomic number) (figure 1.3). The cross section is a slowly varying function of energy.

Pair production occurs when a photon interacts with the Coulombic field of a nucleus (figure 1.5). This absorptive interaction results in the disappearance of the photon and the conversion of its energy into an electron and a positron pair and their associated kinetic energies. The energy threshold for this interaction is 1.022 MeV. The pair production mass attenuation coefficient, κ/ρ , depends on the atomic

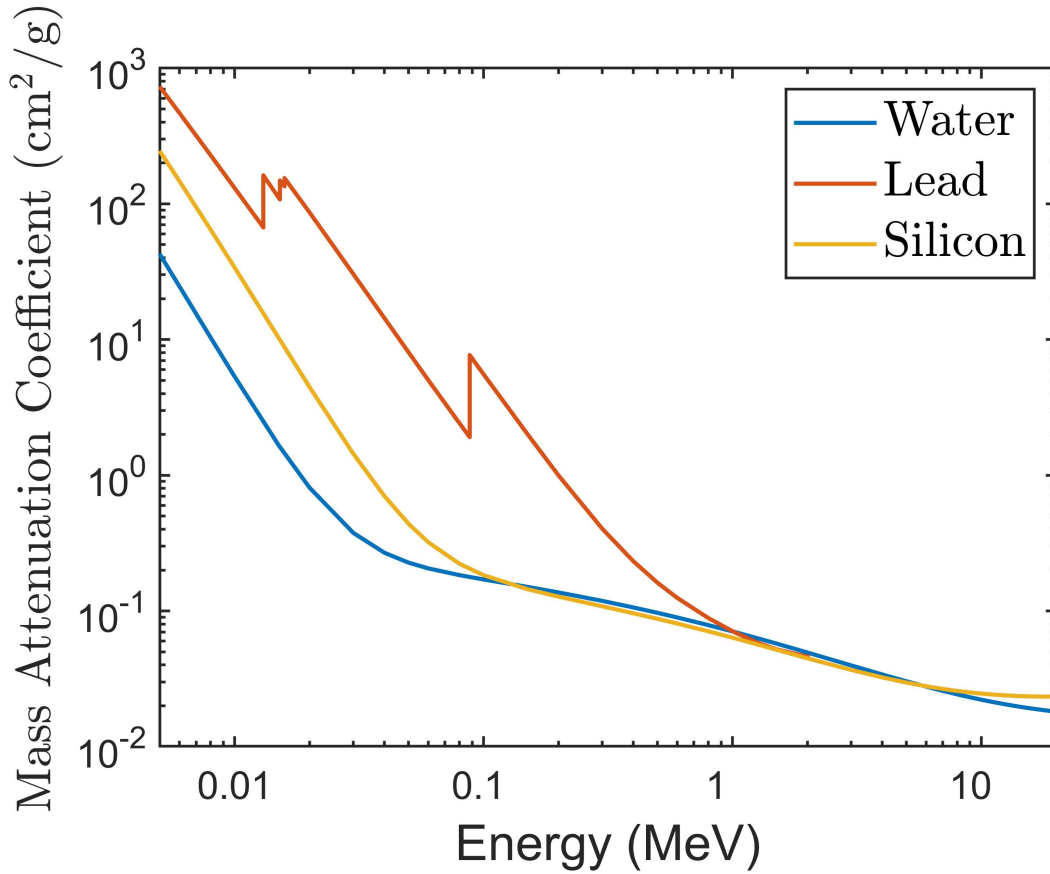


Figure 1.3: Mass attenuation coefficient of water, silicon, and lead as a function of energy. In the kV energy range there is large discrepancies due to the strong dependence of the photoelectric effect with the atomic number. For MV energies the discrepancies are small because the Compton effect is independent of the atomic number. Data retrieved from NIST [4].

number of the medium:

$$\frac{\kappa}{\rho} \propto Z \quad (1.6)$$

The nucleus of the atom receives negligible kinetic energy, but does participate in the conservation of momentum. Figure 1.6 shows the cross-sections of each interaction type and the total cross-section for water. Illustrated is the complex energy dependence for pair production.

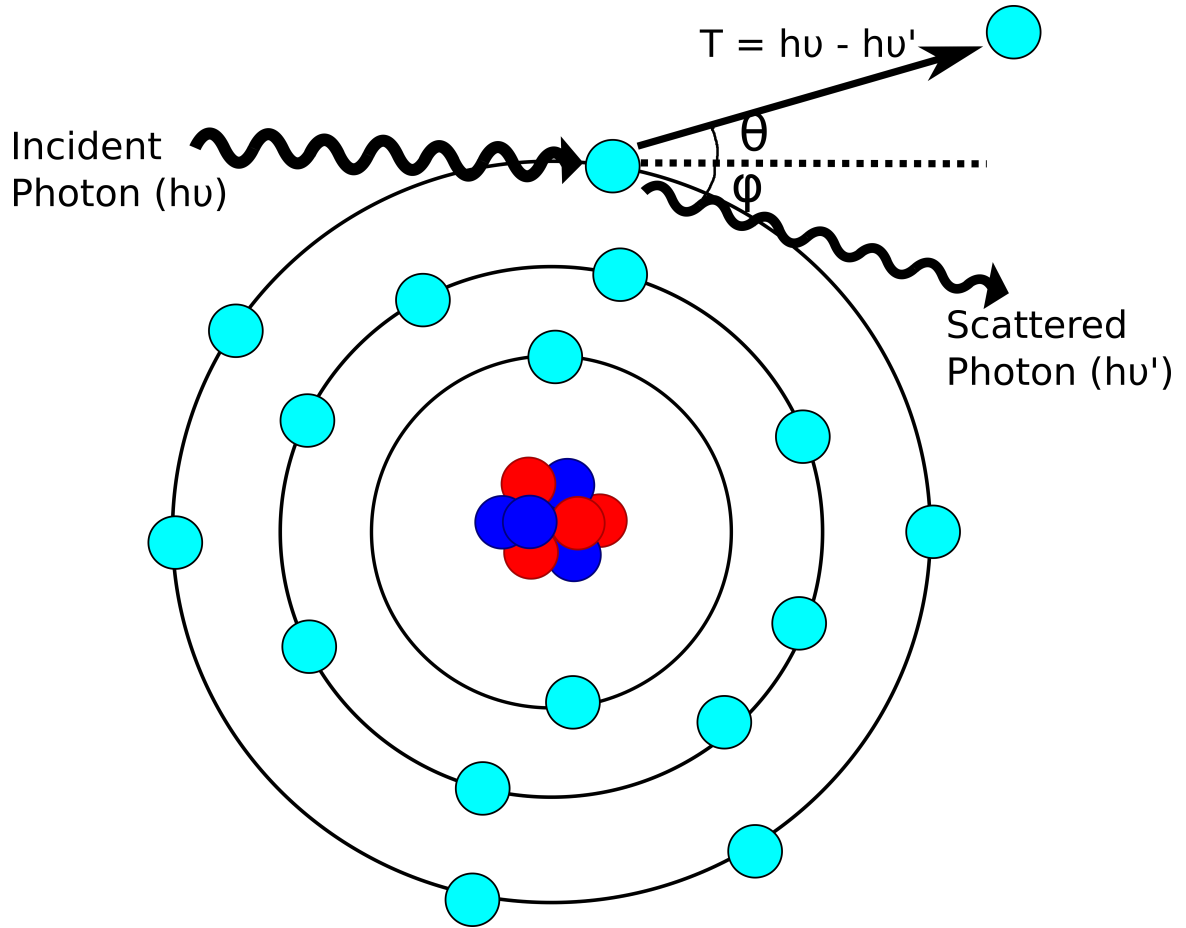


Figure 1.4: Schematic of the Compton effect. An incident photon interacts with a free electron (electron bound with much less energy than the incident photon), which results in a scattered photon at angle ϕ and an electron at angle θ .

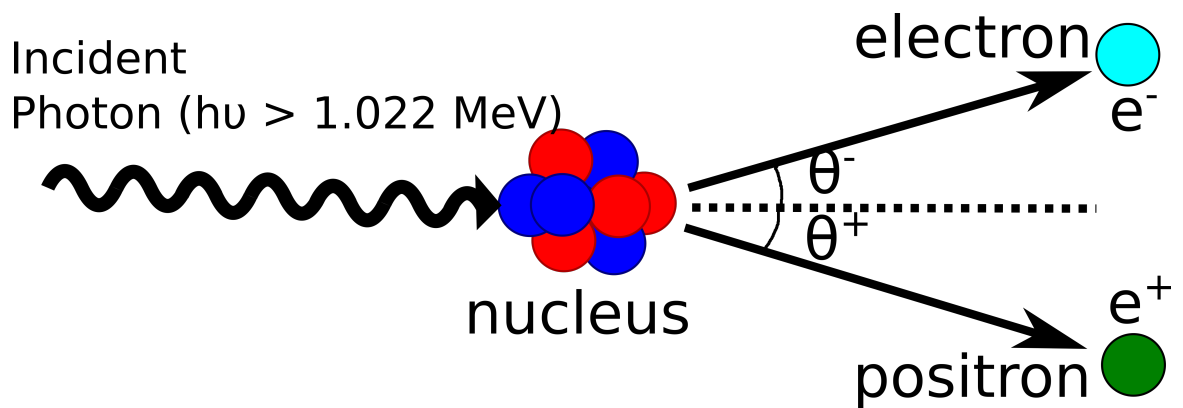


Figure 1.5: A schematic of pair production. An incident photon interacts with the coulombic field of the nucleus, which results in the photon energy being converted into an electron and a positron.

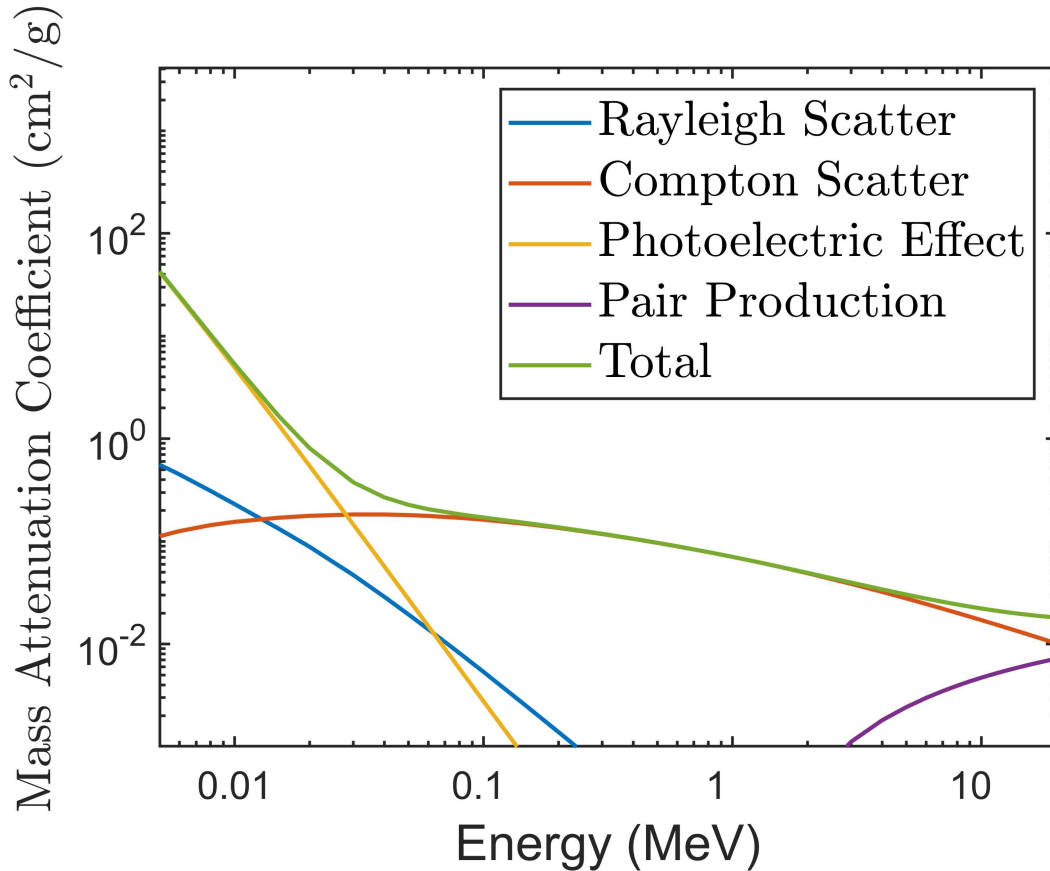


Figure 1.6: Mass attenuation coefficients for water. The various photon interactions are shown individually and the total. This shows the energy range where each interaction type is most prevalent. Data retrieved from NIST [4].

When selecting a radiation detector it is important to think of the irradiation setup and the composition of the detector. Any detector can be calibrated and provided the detector does not change, the calibration factor can be used to determine the dose if the measurement conditions do not differ significantly from the calibration conditions. In a radiotherapy setting, however, differences in measurement conditions from calibration conditions (e.g. field size, the presence of absorbers, etc.) are common and can change the photon and electron spectra incident on the detector, which can, in turn, change the sensitivity of the detector. However, if the detector responds like human tissue, the calibration factor and thus dose measurement may be more accurate for unknown conditions.

The photoelectric effect has a strong dependence on atomic number, whereas Compton effect does not. In radiation fields that produce a significant number of photoelectric interactions in the detector (e.g. diagnostic x-ray beams), the composition of the detector should be similar to tissue. In general, the atomic number of the materials making up the detector is not as important in radiotherapy beams where the dominant interaction is Compton scatter. The photon cross section ratios of several materials to that of water are shown in figure 1.1. Below about 100 keV all of the materials exhibit some change in the ratio of photon cross-section which implies that radiation will not interact with the detection system in an identical manner to the way in which it interacts in water (or tissue). In the therapeutic energy range the ratio is closer to a constant for all of the materials suggesting that a tissue-equivalent elemental composition may not be a necessary condition for successful dosimeter design. Further complicating the picture is that cross section ratio alone is not sufficient to predict the degree of tissue equivalence since other factors can affect the magnitude of signal produced per unit dose (e.g. quenching – described below).

1.3.2 Electron Interactions

Due to the charge of an electron and the $1/r^2$ nature of the Coulomb Force, electrons interact via Coulombic interactions with every atom it passes (either the nucleus of an atom or the electrons). Most of the interactions result in only a small transfer of the incident particle's kinetic energy, causing the electron to slow gradually. Electrons can interact in the medium elastically where they lose no energy, or inelastically where the electron loses some kinetic energy (figure 1.7). Elastic collisions deflect the electron, but no energy is deposited in the tissue meaning it is less important for dosimetry. Inelastic collision with an orbital electron can result in either an excitation (orbital electron moves to higher energy shell) or ionization

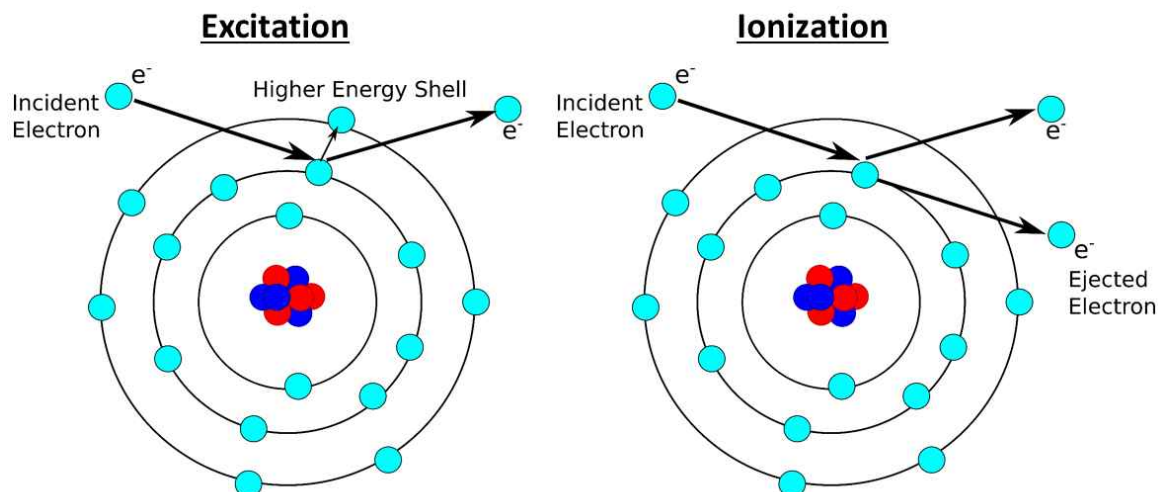


Figure 1.7: Inelastic collisions of an incident electron with an orbital electron resulting in either excitation (left) or ionization (right).

(orbital electron escapes the atom). The amount of energy transferred to the orbital electron can range from negligible to half of the incident electron energy [3]. The term delta ray describes the electrons resulting from an ionization event that have sufficient energy to go on to produce their own track of excitations and ionizations. An inelastic collision with the nucleus of an atom is known as Bremsstrahlung (figure 1.8). The electron decelerates when deflected by a charged particle and the loss of kinetic energy is converted into a photon.

The rate of energy lost by electrons as they travel through a material is given by the stopping power and the stopping power ratio of various materials to water are shown in figure 1.9. Silicon detectors are used with the assumption that the ratio of the stopping power of silicon to water is approximately constant. Although this is not strictly correct, it is a reasonable approximation and silicon diodes are routinely used for relative dose measurements (e.g. percent depth dose) in electron beams.

The range of electrons present strongly depends on the energy of the incident photon beam. When the incident photon beam is of low energy, the electrons

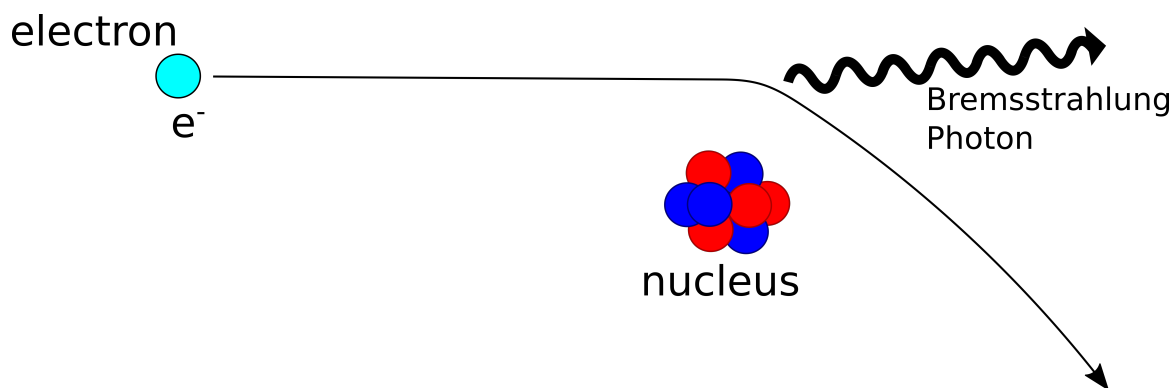


Figure 1.8: Schematic of a Bremsstrahlung photon being created. An electron decelerates when deflected by a charged particle and the loss of kinetic energy is converted into a photon.

set in motion have a small range (smaller than the size of the active layer of the detector). For example, electrons set in motion by a 100 keV photon beam will have an average energy of approximately 14.8 keV in water, which will result in a range of approximately $5 \mu\text{m}$ [7]. Therefore, when modeling the detector for a low energy photon beam, the photon interactions are of paramount importance. However, electrons set in motion by MV photon beams have ranges that can be longer than the dimensions of the detector. For example, electrons set in motion by a 2 MeV photon beam will have an average energy of approximately 1.06 MeV in water, which will result in a range of approximately 4.4 mm [7]. Furthermore, photon interactions within the active volume are not as likely (especially for ionization chambers) as the low energy case. Therefore, stopping power ratios (detector material to water) are more important. There is an intermediate energy region where both interactions are important.

1.3.3 KERMA and Absorbed Dose

In the previous sections, photon and electron interactions were presented to show how the energy from an ionizing beam of photons can transfer their energy

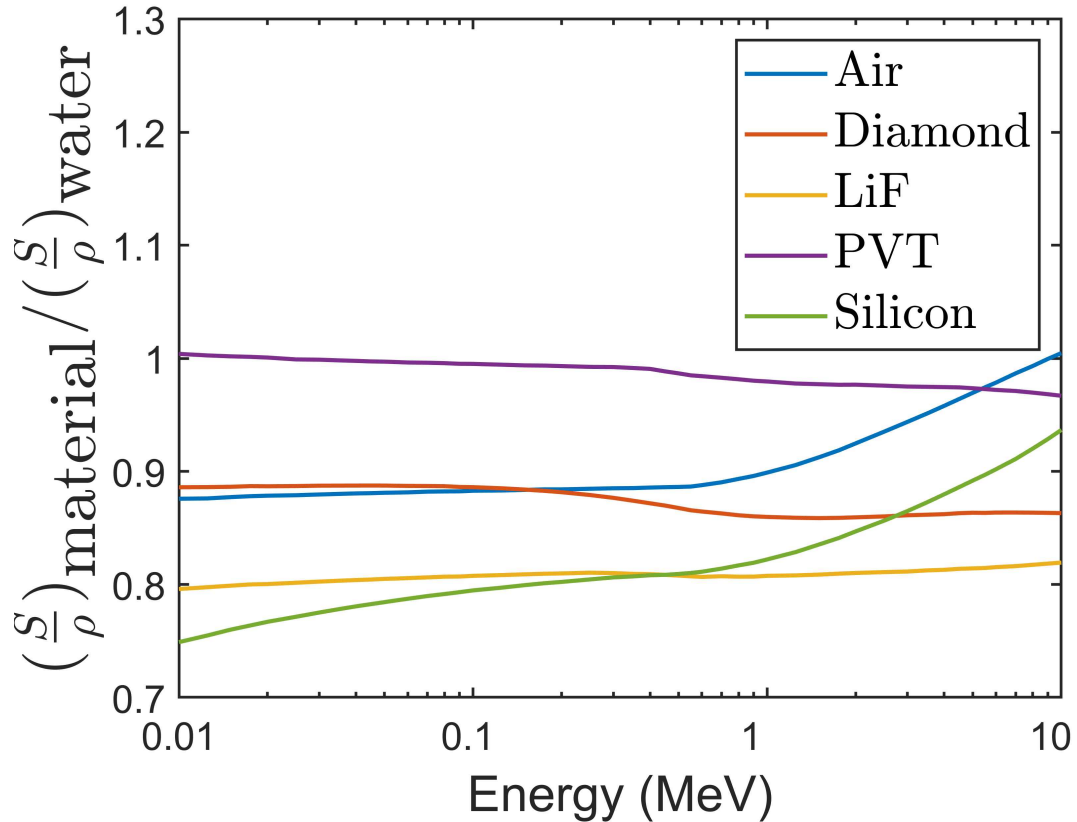


Figure 1.9: Stopping power ratio of a few materials to that of water. The materials are the active volume of common dosimeters. Air for ionization chambers, carbon (3.52 g/cm³) for diamond detector, LiF for TLDs, PVT for plastic scintillators, and silicon for diodes and MOSFETs. Data retrieved from NIST [8].

to a medium and subsequently cause damage, or generate a signal, through ionizations. This section will briefly explain two quantities used to describe the interactions of a radiation field with matter. The quantities are KERMA (kinetic energy released in the medium), and absorbed dose. KERMA describes the first step of energy dissipation by indirectly ionizing radiation such as photons. Absorbed dose describes the energy imparted to matter by ionizing radiation. For a more thorough explanation, see Attix [3]. These quantities will be expressed in terms of expectation values for an infinitesimal sphere at a point of interest.

First, consider a volume V with an incident beam of uncharged particles

which carry radiant energy into the volume, $(R_{in})_u$, and uncharged particles which carry radiant energy out of the volume, $(R_{out})_u$. Radiant energy is defined by the ICRU as the energy of particles (excluding rest mass) emitted, transferred, or received (ICRU-33, 1980) [9]. The difference between these values will give the radiant energy remaining in the volume. However, some of the liberated charged particles can convert their kinetic energy into uncharged particle energy, through bremsstrahlung production or in-flight annihilation of positrons (figure 1.10). This energy contributes to KERMA because KERMA relates to the energy transferred, which is just the kinetic energy received by charge particles in a volume V , regardless of how the charged particles spend that energy (Attix). Since this energy (radiative from bremsstrahlung and in-flight annihilation) has been first given to charged particles it is included in KERMA even though the resulting uncharged particles leave the volume. For the calculation of energy transferred, this changes the fraction of radiant energy leaving V from $(R_{out})_u$, to $(R_{out})_u^{nonr}$, where nonr stands for non-radiative. Furthermore, any transfer of energy to mass, or mass to energy, should be considered for the same reasons. In this case a conversion of energy to mass is subtracted from the energy transferred, and vice versa. Thus the energy transferred ϵ_{tr} , is:

$$\epsilon_{tr} = (R_{in})_u - (R_{out})_u^{nonr} + \Sigma Q \quad (1.7)$$

Where ΣQ is the net energy derived from rest mass within the volume. In an infinitesimal sub-volume dV , with mass dm , inside the volume V , the KERMA, K , is:

$$K = \frac{d\epsilon_{tr}}{dm} \quad (1.8)$$

KERMA is expressed in energy per unit mass, J/kg or Gray (Gy).

KERMA can be further characterized by how the charged particles spend

their energy in the volume. There is collisional KERMA, K_c , and radiative KERMA, K_r :

$$K = K_c + K_r \quad (1.9)$$

First, charged particles can spend their energy through Coulomb-force interactions with the atomic electrons of the material, which results in ionizations and excitations (local dissipation of energy). This fraction is collisional KERMA. Second, charged particles can spend their energy with radiative interactions with the electromagnetic field of the nucleus, which results in photons (relatively more penetrating than electrons and capable of carrying energy far away from the charge particle track) being emitted as the charge particle decelerates. Additionally, positrons can lose kinetic energy through in flight annihilations, where the kinetic energy appears as energy in the resulting photons and is a type of radiative loss of kinetic energy. This fraction of KERMA, is radiative KERMA.

Absorbed dose is relevant to ionizing radiation fields of charged and uncharged particles. With this parameter, it is not the energy transferred to the medium, but the energy imparted. In equation form the imparted energy is:

$$\epsilon = (R_{in})_u - (R_{out})_u + (R_{in})_c - (R_{out})_c + \Sigma Q \quad (1.10)$$

Where $(R_{in})_u$ is the radiant energy of the uncharged particles entering a volume V , $(R_{out})_u$ is the radiant energy of the uncharged particles leaving volume V , $(R_{in})_c$ is the radiant energy of the charged particles entering volume V , $(R_{out})_c$ is the radiant energy of the particles leaving volume V , and ΣQ is the net energy derived from rest mass in V (figure 1.10).

The same way KERMA was related to the energy transferred in a volume the absorbed dose is related to the energy imparted by ionizing radiation to matter

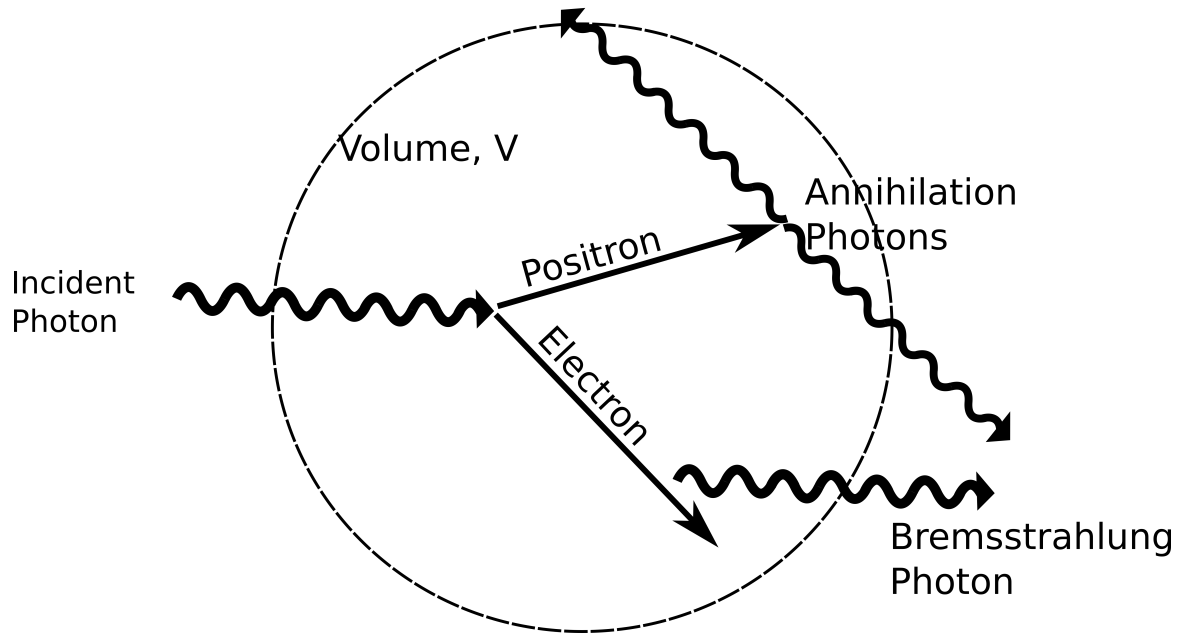


Figure 1.10: Depiction of an incident photon on a volume, V . The photon undergoes pair production, which creates a positron which annihilates, and an electron which give off a Bremsstrahlung photon and loses the rest of its kinetic energy within volume. In this scenario the energy transferred (term in KERMA) is the entire incident photon energy, even though some of that energy is eventually carried outside of the volume. However, the imparted energy (term in dose calculation) is the incident energy minus all of the energy escaping the volume (annihilation photon energy and Bremsstrahlung photon energy).

by:

$$D = \frac{d\epsilon}{dm} \quad (1.11)$$

Where D is the absorbed dose, $d\epsilon$ is the infinitesimal energy imparted in an infinitesimal volume dV , with mass dm . The units of absorbed dose are energy per unit mass, J/kg or Gy.

This derivation gives us the absorbed dose for an infinitesimal volume. Since a detector has a finite size the measurement will be an average measurement over the sensitive volume of the detector. This phenomenon is known as volume averaging and can be problematic if the dose varies considerably over the dimensions

of the detector. What we want then is a detector where the radiation creates a response in the detector proportional to the dose in the absence of the detector.

1.4 Small Field Dosimetry

1.4.1 Rationale for using small fields in radiation therapy

In recent years, there has been a significant increase in adoption of stereotactic treatment delivery techniques for the treatment of small lesions (e.g. brain or liver metastases; function disorders such as trigeminal neuralgia) with large doses delivered in one or a small number of fractions [10, 11, 12, 13, 14]. These complex treatments involve highly non-uniform dose distributions with steep dose gradients outside of the targets. In these cases, even a small error in positioning can lead to a large error in the dose delivered to the target and surrounding healthy tissues. Furthermore, the steep dose gradients make accurate dosimetry more difficult. The ability to quantify the output of a small field and characterize its profile are both critical requirements for accurate treatment planning. These treatment techniques include: intensity modulated radiotherapy (IMRT), volumetric-modulated arc therapy (VMAT), stereotactic radiosurgery (SRS), stereotactic radiotherapy (SRT), and stereotactic ablative radiotherapy (SABR). A variety of treatment machines are used to perform these techniques, such as Gamma Knife, CyberKnife, and a conventional LINAC equipped with multileaf collimators (MLC) or cones.

Studies have shown large discrepancies between detectors for output factors of small fields [15]. The differences depend on the field size and the detector type and can be significant if the active volume of the detector is large compared to the field size or if the composition of the phantom material has radiological properties very different from water.

Until recently no national or international guidance was given about how to

perform accurate dosimetry for small fields and patients have suffered serious consequences as a result [6]. The use of an inappropriate detector (farmer type ion chamber with air cavity of 0.65 cm^3) for measuring small field output factors led to an overdose of 145 patients (maximum overdose approximately 200 %) being treated with micro-MLCs [16]. Another instance resulted in 76 patients being treated with an average dose exceeding the prescribed dose by 50 % when treated with micro-MLCs [17]. These errors emphasize the need for a standard protocol, which makes use of appropriate detectors for small fields. A joint task group was formed between IAEA and AAPM, which resulted in a document, TRS-483, which gives guidelines about how to perform dosimetry for small fields and which detectors are best suited from data collected over a vast collection of research. Furthermore, the report defines what is meant by a small field, which will be defined in the next section.

1.4.2 What Constitutes a Small Field?

For a field to be considered small, one of the following three conditions needs to be met: 1. loss of lateral charged particle equilibrium along the central axis, 2. partial occlusion of the primary photon source along the central axis by collimators in the machine, or 3. the detector size is similar or larger than the cross-sectional measurement at beam depth [6]. If one of these conditions is met, then the detector volume will overlap with the field penumbra even at the center of the field.

The loss of lateral charged particle equilibrium occurs if the beam width is smaller than the lateral range of the majority of secondary electrons. Recall that dose deposition from an incident photon beam is a two-step process. First, photons transfer their energy to secondary charged particles in the medium. Second, the secondary charged particles interact with the medium, which results in the dose deposition. These secondary charged particles will deposit dose along the track they travel as they come to rest some distance from the initial photon interaction point.

Lateral charged particle equilibrium is said to exist on the central axis if for every secondary charge particle that is created along the central axis and is displaced laterally, there is another one created somewhere else and makes its way to the central axis. As the field size is decreased, photons are collimated that would have otherwise interacted in the medium and set into motion electrons that could have made their way to the central axis. Therefore, lateral charged particle equilibrium no longer exists. As beam energy increases, the maximum range of the secondary electrons increases, which leads to a loss of lateral charged particle equilibrium at larger field sizes. A relationship has been derived by fitting an equation to Monte Carlo calculations to determine when a field becomes small in regards to loss of lateral charged particle equilibrium based on the energy of the beam. Using this relationship a beam of ~ 6 MV is small for field sizes smaller than approximately ~ 1.1 cm radius or a 2.2×2.2 cm² field size and a field size of $\sim 3.2 \times 3.2$ cm² is considered small for a 10 MV beam[6].

The second condition which can be met to classify a small field is partial source occlusion (figure 1.11). A photon beam has a finite source size which is usually defined as the full width at half maximum of the bremsstrahlung photon fluence distribution exiting the target. If the collimators shaping the field blocks part of the primary photon source at the center of the field then the output of the beam will be lowered and this is known as source occlusion. This effect becomes important when the field size is comparable or smaller than the photon source size, which is smaller than 5 mm (projected at isocenter) [18]. Therefore, primary source occlusion usually occurs for field sizes smaller than where lateral charged particle equilibrium occurs [6].

The third condition that characterizes a small field is related to the size of the detector relative to the radiation beam. The detector signal is proportional to

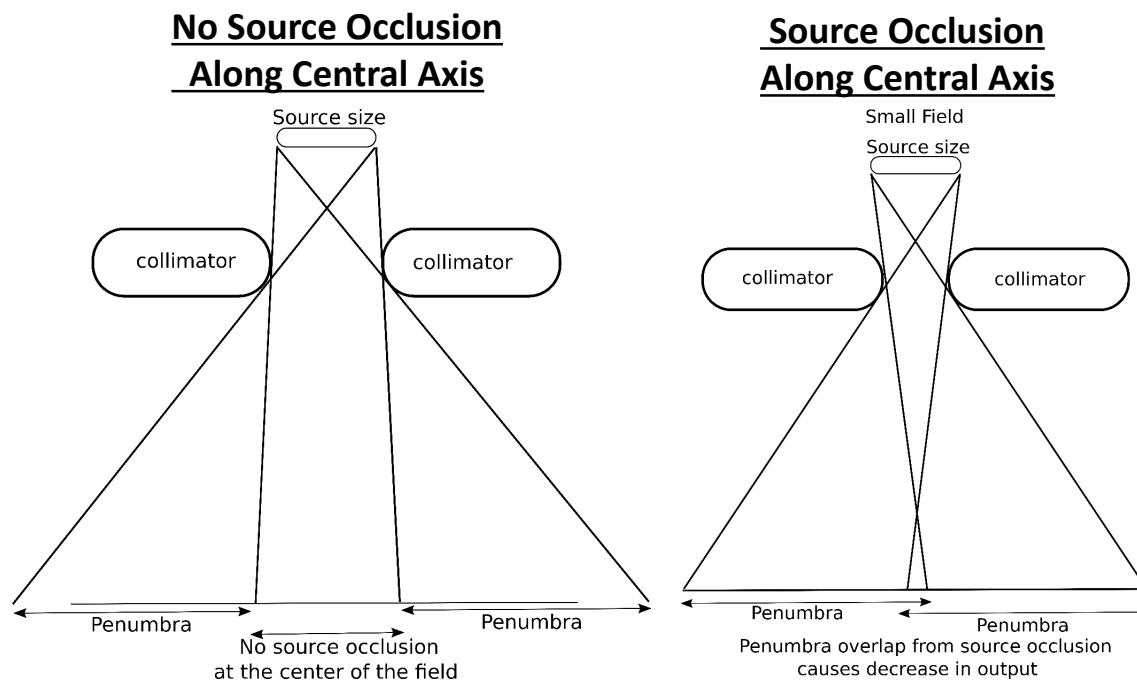


Figure 1.11: Schematic of source occlusion effect. In the left schematic none of the photon fluence is blocked by the collimators at the center of the field. On the right schematic, the output is lower at the center of the field due to the fluence being partially blocked by the collimators.

the mean absorbed dose over the sensitive volume of the detector creating a volume averaging effect. If the detector is placed at the center of a small field, it will give an average reading over the volume of the detector. For large fields the dose changes very little a small distance from the center of the field, but for small fields the volume averaging effect can be significant. To determine the dose at a point a deconvolution process would be necessary. Another problem is the perturbation of the charged particle fluence created by the presence of the detector. With large dose gradients and loss of lateral charged particle equilibrium, the perturbations become large. Furthermore, it is difficult to model and correct because even minor variations in detector design that are within engineering tolerances can cause large

differences [6]. These difficulties start to present when charged particle disequilibrium occurs at any point in the detector volume even if there is still charged particle equilibrium at the center of the detector. Therefore, to be considered a small field the detector effect can be combined with the loss of lateral charged particle equilibrium effect. Doing so means a field can be considered small when the external edge of the detector volume is at a distance from the edge of the field that is less than the lateral charged particle equilibrium range. To avoid this condition along the beam center, the beam width has to be larger than half the size of the detector plus the range of the charged particles.

1.4.3 Field Output Correction Factors

As the field size decreases, the fraction of scattered photons contributing to the central axis photon energy distribution spectrum decreases as well, which causes the average energy of the photons to increase. There are two components to scatter. First, are photons scattered within the Linac head, which includes the flattening filter and primary collimator. Thus as the collimator opening decreases the number of scattered photons reaching the center of the small field is reduced. Second, are photons scattered within the phantom. As the field size decreases the number of photons incident on the phantom decreases and therefore so do the number of scattered photons in the patient to reach the beam central axis. These effects result in an increased average photon energy at the center of the beam. This can affect the ratio of the mass energy-absorption coefficients and stopping power ratios between water and the detector material relative to reference conditions. Furthermore, when the field is too small for lateral charge particle equilibrium, there will be a deficit of low energy electrons reaching the center of the radiation field. These effects have been shown to cause an error in the response of diode detectors and small ionization chambers with high-Z electrodes, which may be even worse for flattening filter free

beams [19, 20, 21, 22].

Due to the reasons listed above, the response of a detector at small fields may lead to inaccurate quantification of dose. In response, TRS-483 introduced a field output correction factor, which accounts for the differences in the detector response for a non-reference (clinical) field to a reference field. The report gives tables of correction factors for a variety of detectors, for various radiation machines as a function of field size. Standard Imaging's Exradin W1 (plastic scintillator based detector) performs the best, with a correction factor of 1.000 over a wide range of field sizes and machines (has a value of 1.000 for a 6 MV beam at the smallest field size listed of $0.4 \times 0.4 \text{ cm}^2$). Other detectors have a correction factor that varies with field size, which will cause an error if the field size is not exact. For example, for a 6 MV photon beam the PTW 31010 Semiflex micro ion chamber has a correction factor of 1.001 for a $3 \times 3 \text{ cm}^2$ field size, 1.025 for a $1.5 \times 1.5 \text{ cm}^2$ field size, and no values are provided for smaller field sizes (if the correction factor exceeds 5 % it is not recommended to be used and thus the values are not provided). For a 6 MV photon beam the PTW 60016 shielded diode has a correction factor of 0.999 for a $4 \times 4 \text{ cm}^2$ field size, 0.956 for a $1.2 \times 1.2 \text{ cm}^2$ field size, and no values are provided for smaller field sizes. The accuracy of a plastic scintillation based detector for small fields is one of the motivating factors behind the design of our SPSD detector. The next section will go over ideal characteristics of radiation detectors and go over some detectors that are used clinically (mechanism of detection, advantages, disadvantages, etc.).

1.5 Detecting Radiation

1.5.1 Ideal Dosimeter Characteristics

When measuring a radiation field it is often the ionization process that forms

the basis of the measured signal in a radiation detector. By calibrating the detector appropriately, the measured signal can be converted into the amount of energy absorbed per unit mass to a small mass of tissue if it were positioned at the same location as the detector. Characteristics an ideal dosimeter would possess include:

- Linearity: Dosimeter response should be proportional to the absorbed dose to the detector.
- Sensitivity: Dosimeter should have a large signal to noise ratio even for measurements of low doses.
- Reproducibility: Dosimeter response should be consistent when irradiated with the same conditions.
- Stability: Dosimeter response to absorbed dose should be consistent over time.
- Temperature and humidity: Dosimeter response should be independent of temperature and humidity.
- Real time readout: Dosimeter response and thus absorbed dose should be measurable during irradiation.
- Dose rate: Dosimeter response should be proportional to absorbed dose independent of dose rate. Includes both instantaneous dose rate and average dose rate.
- Energy independence: Dosimeter response should be proportional to absorbed dose, independent of the energy or type of radiation.
- Directional independence: Dosimeter response should be proportional to absorbed dose independent of the angle of incident radiation.
- High spatial resolution: Dosimeter dimensions should be small enough that the dose does not vary significantly over the sensitive volume of the detector.

Currently no dosimeter can be considered ideal. Some currently used dosimeters include ionization chambers, radiochromic film, diodes, diamond, metal-oxide-semiconductor field-effect transistors (MOSFETs), Thermoluminescent Dosimeters (TLDs), Optically Stimulated Luminescent Dosimeters (OSLDs), and scintillators.

1.5.2 Currently Used Detectors

An ionization chamber consists of a gas filled chamber with two electrodes [23]. Incident electrons can interact and create ion-pairs in the gas chamber. By applying a potential difference between the two electrodes, positive ions move toward the negative electrode and vice versa. This creates an ionization current proportional to the number of ion pairs created that can be measured with an electrometer. Since the active volume is a gas, it requires a larger volume to produce a measurable signal in comparison to solid state dosimeters. Furthermore, the reading is the average dose to the active volume which can be problematic for small field dosimetry where the dose changes with positional changes smaller than the size of the detector, creating a partial volume effect. Another limitation is the energy dependence of ionization chambers which can be problematic at diagnostic energies. TG-61 lists the average mass energy-absorption coefficient ratios of water to air, which are necessary to calculate the dose to water using an ion chamber at kV energies [24]. At 100 kV the ratio is approximately 1.018 and at 300 kV it is approximately 1.109, which is approximately a 9% change in response.

Radiochromic film consists of a layer of organic monomers on a polyester base with a transparent coating [25]. When irradiated, the film changes colour due to the monomers polymerizing in the film. A scanner is used to measure the colour change, which is used to convert to a dose measurement. Advantages of radiochromic film in comparison to radiographic film is that it is relatively insensitive to room light and does not need to be developed. Other advantages include near water equivalency, low dose rate dependence, and the film can be cut for easy integration into a range of measurement conditions and phantoms. Film exhibits low energy dependence in the therapeutic energy range, but is not energy independent for kV energies [26]. One of the main drawbacks of film is that readout occurs 12-24 hours

after irradiation to allow the film to fully develop. The optical density of the Radiochromic film can be affected by the orientation of the film (i.e. the film must be placed in the scanner with the same orientation before and after irradiation), temperature, and has shown inconsistencies from batch to batch, and across a single piece of film [27, 28]. Furthermore, the exact positioning of the film in the scanner can affect the readout. Therefore, it is of utmost importance to have a consistent film preparation and readout protocol [29].

A diode dosimeter operates using a p-n junction, which is created in the region where a lightly doped silicon substrate (either n-type or p-type) and a heavily doped surface region of opposite doping (p-type or n-type) come together. The p-n junction produces an electric field which allows the collection of current with no external bias applied. An electric current proportional to dose rate is generated when exposed to ionizing irradiation, which is measured using an electrometer [30]. Limitations of diode dosimeters include energy dependence, temperature dependence, and accumulated dose dependence [31, 32, 33, 34]. Strengths of the diode dosimeter include their small active volume and as electron dosimeters they are approximately energy independent since the electron stopping power of silicon to water is approximately constant over a wide energy range.

Most recent diamond detectors use synthetic diamond that have an ohmic contact that makes the diamond function as a Schottky diode and allows it to operate without a bias applied [35, 36]. Diamond detectors have a small active volume. However, the detector is contained in a housing that can be much larger. Diamond detectors have low angular dependence, are energy independent in the therapeutic range of energies, and negligible dose rate dependence [35]. Diamond detectors have exhibited good linearity and stability, but do require a pre-irradiation of 5-10 Gy to ensure the stability. Another drawback is that due to the small detector size and low signal, the stem effect can significantly contribute to the signal depending on

orientation of the detector and the beam.

A MOSFET is a voltage-controlled current source. Exposure to ionizing radiation results in the creation of electron-hole pairs in the silicon-dioxide layer [37]. Holes become trapped at the silicon-dioxide/silicon interface, which changes the current that will flow through the MOSFET for a given applied voltage. After calibrating the rate of change of a particular metric (e.g. threshold voltage) as a function of the absorbed dose, the MOSFET can be used as a dosimeter. Limitations of MOSFET dosimeters include energy dependence, the signal fades with time, and they have a short lifetime (approximately 80 Gy) [38, 39]. The strengths of MOSFETs include permanent dose storage, small active volume and they can be made to have negligible temperature dependence [40].

TLDs consist of a crystalline dielectric material containing trace impurities. The impurities are introduced to create trapping centers whose energy levels lie within the forbidden gap of the pure crystal. A portion of the absorbed energy from ionizing irradiation is stored in the TLD due to electrons and holes stuck in the trapping centers [41]. When the TLD is heated the electrons are excited from the traps into the conduction band. The electrons then recombine with the holes in the valence band resulting in a release of visible light proportional to the amount of absorbed dose [42]. Since the emitted photons do not have enough energy to promote electrons from the valence band to the conduction band the light is not absorbed by the crystal. TLDs exhibit excellent energy dependence down to 20 keV [43]. Other advantages are that they can be made small (1 mm^3 or smaller) and can be reused after annealing. Limitations of TLDs are their lack of real time readout, they exhibit a supralinear response with dose, they require specialized hardware for readout, and need precise procedures for calibrating, reading, and annealing [44].

OSLDs are similar to TLDs in their mechanism for use as a radiation detector. However, OSLEDs are readout by illuminating the crystal as opposed to heating

it. OSLDs have various chemical compositions with $\text{Al}_2\text{O}_3:\text{C}$ being the most common one. The higher atomic composition relative to TLDs gives it a larger energy dependence at low energies. One advantage to OSLDs is that they can be readout multiple times. The readout of a nanoDOT OSLD (Landauer, Glenwood, Illinois) can be achieved using a short stimulation where less than 0.05% of the trapped charge is release for each readout [45, 46]. This allows multiple readouts to reduce uncertainty or a more permanent dose measurement record. Although a few measurements can be done without drastically changing the signal, there is a depletion to the trapped electrons with each readout and a systematic reduction of signal. OSLDs have low temperature, angular, and dose rate dependence, allowing them to be placed directly on the patient for in vivo dosimetry for a variety of treatment modalities.

Plastic scintillation detectors (PSDs) emit light proportional to the radiation dose deposited. A more thorough explanation of the underlying physics will be given in section 1.6.1 due to its pertinence to the detectors described in this thesis. The light emitted from the PSD is carried using an optical fiber to a detector which converts the light into an electrical signal. Advantages of PSDs include: small size, dose rate independence (in conventional MV radiotherapy applications), temperature independence, low energy dependence in the therapeutic energy range, and a linear response with dose. However, there is an energy dependence for kV imaging due to quenching and the difference of mass energy-absorption coefficients between the PSD and water [47, 48]. The Exradin W1 (commercial PSD) has a field output correction factor of 1.000 down to the smallest field sizes listed in TRS-483, making them ideal for small field detectors [6]. The main drawback to PSDs is Cerenkov radiation which contaminates the scintillation light due to its production in both the scintillator and the optical fibre. Cerenkov light is created when a charged particle moves through a medium at a speed faster than the speed of light

of that medium. The Cerenkov light emitted depends on, the angle of the beam, the amount of optical fiber exposed to the beam, the type of radiation, the energy of particles, and other dependencies. A further explanation and description of how Cerenkov is normally corrected is given in section 1.6.3.

Table I: Common detector types and their characteristics. Exact dependences (characteristics) can vary within a type of detector based on materials of the detector, surrounding housing, etc. Dependencies are given for a common commercial product in brackets for each type of detector.

	Ionization Chamber (Exradin A12)	Radiochromic Film (EBT3 Gafchromic Film)
Linearity	Excellent	Non-linear – requires calibration curve (Dose range varies depending on the product (typical 0.1 cGy-10 Gy))
Sensitivity	Depends on the design (mainly active volume) of the detector. (active volume 0.64 cc and sensitivity of 23 nC/Gy)	The minimum detectable dose is 1 cGy. The sensitivity varies with dose due to a non-linear calibration curve.
Reproducibility	Excellent	Can vary batch to batch (a new calibration is required for each batch)
Stability	Excellent	Signal continues to develop for up to 24 hours post exposure
Temperature	Easy to correct	Signal depends on temperature of the scanning bulb
Real Time Read-out	Yes	No
Dose Rate	No dose rate dependence over the typical therapeutic range	No dose rate dependence over the typical therapeutic range

Energy	Depends on the design, but usually needs correction for kV energies	Energy dependence for kV energies
Directional	Excellent in radial direction, can vary in longitudinal direction depending on design and amount of stem in field (for cylindrical chambers)	Low (depends on the design of film)
High Spatial Resolution	Depends on design	Excellent (depends on scanner resolution)
	Silicon Diode (PTW 60023 Microsilicon)	Diamond (PTW 60019 microDiamond)
Linearity	Linear over dose ranges usually encountered in radiotherapy. Due to decrease of signal with accumulated dose it needs to be recalibrated occasionally	Excellent (need to pre-irradiated)
Sensitivity	Depends on construction of diode (10-20 nC/Gy)	(1nC/Gy)
Reproducibility	Excellent	Excellent
Stability	Loses sensitivity with accumulated dose (0.1%/kGy for 6 MV photons)	Very good
Temperature	Can be corrected for (0.1%/K)	Can be corrected for (≤ 0.8 %/K)
Real Time Read-out	Yes	Yes
Dose Rate	Yes, diodes often have a dose per pulse dependence that needs to be corrected for	Very little
Energy	Varies greatly with design. Large energy dependence for kV photons. (Can be used for small fields down to 0.4 cm with correction factor)	Low (Useful energy range 100 keV – 25 MV photons, 6-25 MeV electrons)

Directional	Yes, depends on the housing of the diode. ($\leq 1\%$ for rotation around chamber axis, $\leq 1\%$ for tilting of the axis up to $\pm 20^\circ$)	($\leq 1\%$ for tilting $\pm 40^\circ$ in longitudinal direction)
High Spatial Resolution	Very high (active volume 0.03 mm^3)	Very high (active volume 0.004 mm^3)
	MOSFET	TLDs (Thermo Fisher TLD-100)
Linearity	Sub-linear	Supralinear (can measure up to 10 Gy with correction)
Sensitivity	Decreases with dose	($\pm 10\%$ uncertainty for a single measurement)
Reproducibility	Can vary between devices by up to 5%	($\pm 10\%$ uncertainty for a single measurement)
Stability	Signal fades over time	Signal fades with time. Need a consistent protocol for readout
Temperature	A single MOSFET will need a temperature correction. A dual-MOSFET dual-bias detector has very little temperature dependence	TLDs should be stored at room temperature (avoid high temperatures) to minimize fading
Real Time Read-out	Can be read out in real-time or after irradiation	No
Dose Rate	Excellent	Excellent
Energy	Energy dependent due to use of silicon and highly depends on the construction of the MOSFET	Excellent energy dependence down to 20 keV
Directional	Yes, due to asymmetry of materials of transistor and packaging	Excellent
High Spatial Resolution	Very high	($1 \times 1 \times 1 \text{ mm}^3$)
	OSLDs (Landauer nanoDot)	PSDs (commercial product Exradin W1)

Linearity	(linear up to 300 cGy, non-linear calibration needed up to 1500 cGy)	Excellent
Sensitivity	Lowest detectable dose below 10 mGy	60 pC/Gy
Reproducibility	Reproducibility 2-3%	Excellent
Stability	Signal fades with time. Most fading happens in first 10 minutes, followed by gradual (1% every 3 months) after that	Loses 2%/kGy
Temperature	Yes (should be calibrated near temperature it will be used)	Small dependence (can be calibrated at temperature of application or apply a correction factor)
Real Time Read-out	No	Yes
Dose Rate	Excellent (for conventional MV radiotherapy applications)	Excellent (for conventional MV radiotherapy applications)
Energy	Energy dependence for kV energies (can be operated from 5 keV to 20 MeV with appropriate corrections)	Energy dependence at kV energies
Directional	Minimal with appropriate calibration	Excellent after Cerenkov correction
High Spatial Resolution	Can vary (active volume: diameter 5 mm and thickness 0.3 mm)	Good (active volume: diameter 1 mm and length 3mm)

1.6 Scintillator Physics

1.6.1 Scintillation Light

A scintillator is a material that, when excited by ionizing irradiation, will emit some of the absorbed energy in the form of light. For high energy photons and

electrons the light produced in plastic scintillators is proportional to the energy absorbed. To determine the dose deposited in the scintillator the light output is measured. Principle scintillation light (or prompt fluorescence) in organics arises from transitions in the energy level structure in a single molecule [36]. Most practical organic scintillators are based on organic molecules which have a pi-electron structure. Energy levels of a pi-electronic structure for a molecule are shown in figure 1.12. Singlet states (spin 0) are labeled as S_0 , S_1 , S_2 etc. and triplet states (spin 1) are labelled T_1 , T_2 , T_3 etc. For most organic molecules of interest the energy spacing between S_0 and S_1 is approximately 3 or 4 eV. Each electronic configuration is then subdivided further with much finer energy spacing (on the order of 0.15 eV) that correspond to various vibrational states of the molecule. The second subscript is used to distinguish the various vibrational states with S_{00} being the ground electronic state.

Before excitation, nearly all molecules are in the S_{00} state at room temperature because the spacing between vibrational states is large compared to the average thermal energies (0.025 eV). When energy is absorbed, it can result in an electron going from the ground state S_{00} into any number of excited states (represented by upward arrows in the figure). When excited to the higher singlet states they de-excite on the order of picoseconds through radiationless internal conversion to the S_1 state [49]. Furthermore, any state with excess vibrational energy such as S_{11} or S_{12} will not be in thermal equilibrium with its neighbours and quickly loses the vibrational energy. The overall effect is after a short time in comparison to fluorescence all excited states will be in the S_{10} state. The scintillation light is emitted from transitions from the S_{10} state to one of the vibrational states of the ground state which typically happens in a few nanoseconds. Through a transition called intersystem crossing, some excited singlet states may convert to triplet states. The lifetime of the triplet states may be as long as milliseconds before de-exciting to S_0 .

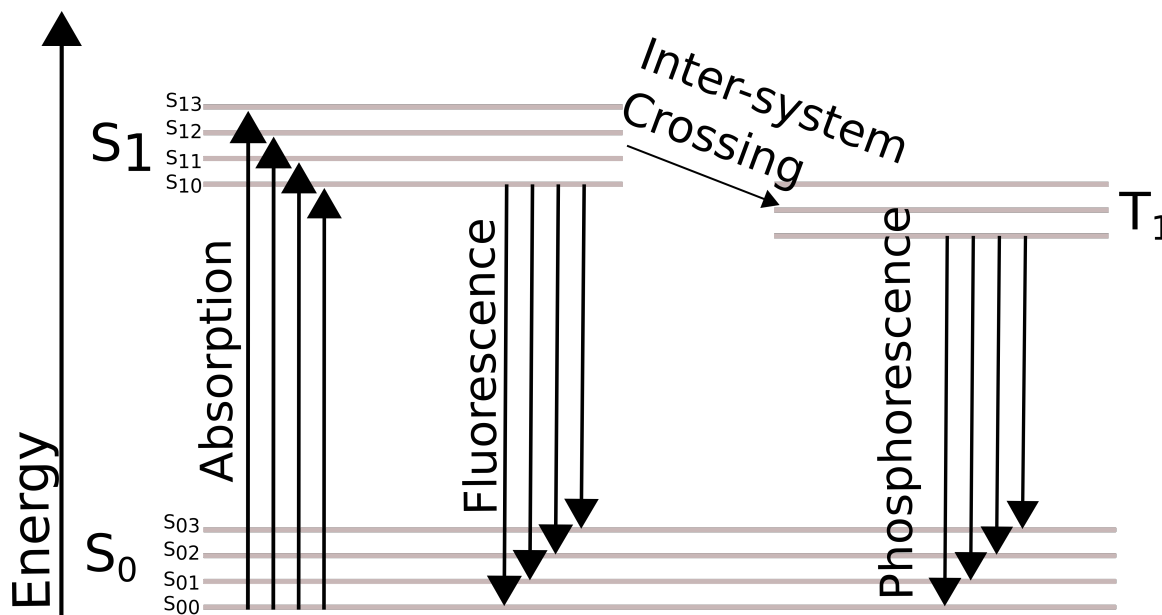


Figure 1.12: Energy levels of an organic molecule. When energy is absorbed from the ionizing radiation it can cause electrons to go into an excited state (S_{1X}). When the electrons transition back to the ground state they do so by giving off a photon (fluorescence). Electrons can also transfer from the singlet state (S_1) to a triplet state (T_1) in a process called inter-system crossing. Phosphorescence results in the emission of a photon when the electron transitions from the triplet state to the ground state and the photon has lower energy than fluorescence.

The light given off by this delayed transition, known as phosphorescence, will have longer wavelength than fluorescence since T_1 lies below S_1 . There is little self-absorption since all fluorescence transitions (exception of S_{10} to S_{00}) have lower energy than the minimum required for excitation, meaning there is very little overlap between the absorption and emission spectra (Stokes shift).

1.6.2 Quenching of Scintillation Light

The scintillation efficiency of a scintillator is the fraction of the incident particle energy that is converted into visible light. An ideal scintillator would convert all of the absorbed energy into light. However, there are alternate de-excitation modes that do not involve the emission of light, which will result in the energy mainly being dissipated as lattice vibrations or heat [49]. All radiationless de-excitation

processes are combined under the term quenching. The amount of quenching depends on the incident particle type and energy. Quenching in organic scintillators is most commonly described using Birks model [50]. The model relates the fluorescent energy emitted per unit path length dL/dx , and the specific energy loss of the charged particle dE/dx . This model uses the assumption that a high ionization density along the track of the particle leads to quenching due to damaged molecules. From this assumption the density of damaged molecules is $B(dE/dx)$ where B is a proportionality constant. Some fraction of these, k , will result in quenching. Another assumption is that in the absence of quenching, light yield and energy loss are proportional:

$$\frac{dL}{dx} = S \frac{dE}{dx} \quad (1.12)$$

where S is the scintillation efficiency. To account for the probability of quenching:

$$\frac{dL}{dx} = \frac{S(\frac{dE}{dx})}{1 + kB(\frac{dE}{dx})} \quad (1.13)$$

which is referred to as Birks model. The term kB is often called Birks constant as is modelled as one adjustable parameter to fit experimental data. When excited by high energy electrons (directly or from photon beam), dE/dx is small for large values of E and Birks model reduces to:

$$L = SE \quad (1.14)$$

Which shows that the light output is related to the initial particle energy. In practice it has been seen that for many plastic scintillators such as anthracene and stilbene, the response to electrons is linear for initial particle energies above 125 keV, but deviates at lower energies [50, 51]. Furthermore, the model has had success for

proton and alpha beams [49]. However, Birks model does not fit experimental data well for low energy photon beams (below approximately 200 keV) [48, 52].

1.6.3 Cerenkov Radiation

Conventional PSDs are fabricated by coupling a scintillating element to an optical fiber which carries the light from the scintillator to an optical sensor (e.g. CCD, photodiode, spectrophotometer, etc.) to be converted to an electrical signal and measured. The main downside of this technique is that Cerenkov radiation produced in the optical fiber stem contaminates the signal (figure 1.13). Cerenkov radiation is radiation produced when a charged particle passes through a medium at a speed greater than the speed of light in that medium. Therefore, in equation form the threshold velocity is:

$$\beta = \frac{v}{c} = \frac{1}{n} \quad (1.15)$$

Where β is the phase velocity of the charged particle and n is the refractive index of the medium. For an electron, the resulting threshold energy can be derived and is given by the equation:

$$E_{Th} = m_0c^2 \left(\frac{1}{\sqrt{1 - (\frac{1}{n^2})}} - 1 \right) \quad (1.16)$$

Where E_{Th} is the threshold energy and m_0c^2 is the rest energy of the electron. For water (refractive index ~ 1.33), glass (refractive index ~ 1.5), and polystyrene (refractive index ~ 1.59), this results in threshold energies of approximately 260 keV, 175 keV, and 146 keV respectively. The angle of emission is:

$$\theta = \cos^{-1}\left(\frac{1}{\beta n}\right) \quad (1.17)$$

Where θ is the angle of emission. The Cerenkov emission spectrum peaks in the blue-violet region and intensity follows as λ^{-3} [36]. Cerenkov radiation in the optical fiber adds to the scintillation light, contaminating the signal and must be removed for accurate dosimetry. The intensity of the light produced by the scintillator is up to 2 orders of magnitude higher per mm than the Cerenkov light [53]. However, due to the light guide within the radiation field usually being much longer than the scintillator it can make up a significant fraction of the light detected. Furthermore, the fraction of Cerenkov radiation detected depends on the irradiation geometry because its directionality is determined by the direction of motion of the electron causing its production. Cerenkov radiation can produce dosimetric errors greater than 10% depending on beam energy, beam angle, correction method, scintillation efficiency, and depth of the detector [54]. Further complicating the correction is the fact that Cerenkov can be produced in the scintillator itself [54].

To remove the Cerenkov signal, several correction techniques have been tested to various degrees of success. These include two-fiber subtraction, basic spectral filtering, and chromatic removal [55, 56, 57]. Two-fiber subtraction consists of two optical fibers placed directly next to one another [47, 57]. One optical fiber has a scintillator on the end and the other does not. After irradiation, the signal measured in the fiber without the scintillator (Cerenkov radiation) is subtracted from the fiber with the scintillator on the end (scintillation light and Cerenkov radiation). The main assumption of this technique is that both optical fibers receive the same fluence. Therefore, the main limitation of the technique is that it does not work well in high gradient regions. Basic spectral filtering is a technique that measures the light away from the blue region (where Cerenkov is highest) by using an optical filter or a photodetector sensitive to longer wavelengths. The main downside of this technique is that Cerenkov is emitted at all wavelengths and therefore

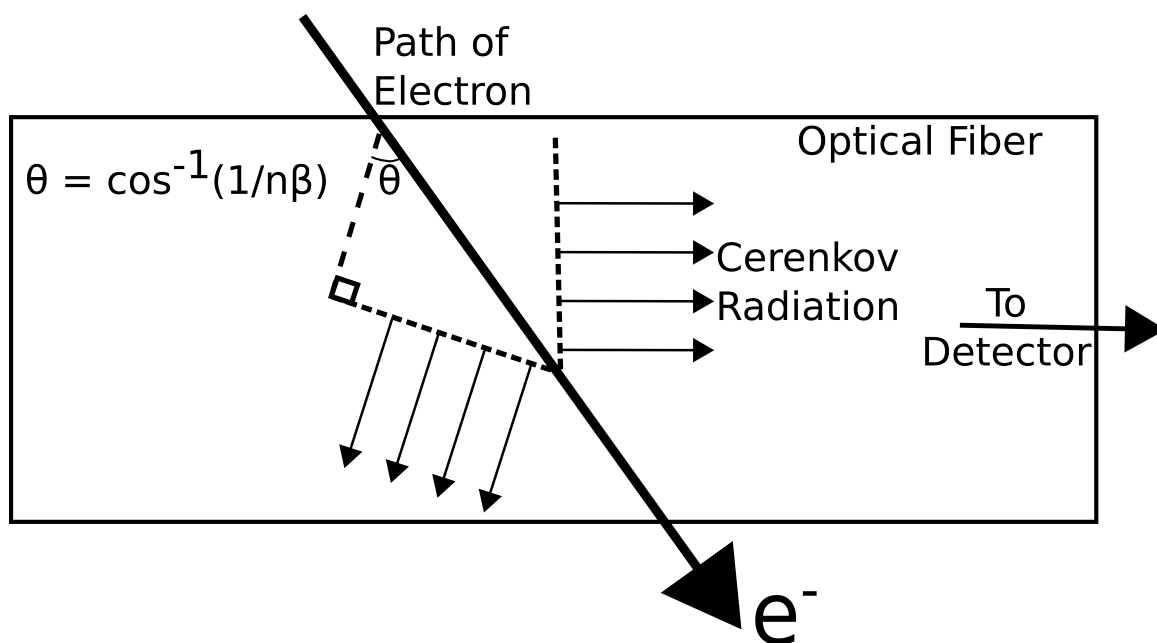


Figure 1.13: The angle the Cerenkov radiation is emitted depends on the velocity of the charged particle and the index of refraction of the medium. The Cerenkov radiation is emitted in a cone in the wake of the electron. Cerenkov initially directed toward the detector will preferentially be detected. The probability of detecting Cerenkov decreases with the number of reflections necessary to reach the detector.

can never be fully removed [55]. The chromatic removal technique consists of filtering the measured light into two or more spectral channels. The measured signal is a linear superposition of two signals (scintillation light and Cerenkov) for each channel. By irradiating the detector with the same dose but in two different conditions to allow differing amounts of Cerenkov, calibration factors can be determined. As long as the detector is used in setup conditions that do not differ substantially from calibration conditions, an accurate dose measurement can be achieved [52, 55]. The main downsides of this technique are that the detector may need a different calibration depending on its use (small fields may need a different calibration from large fields) and it requires specialized equipment to separate and measure the signal on two channels.

1.6.4 Fluorescence of Optical Fiber

Another possible stem effect is fluorescence from the plastic optical fiber due to direct excitation. It has been found to be orders of magnitude lower than Cerenkov, but at low energies (where Cerenkov is not possible) it is the dominant stem effect [53]. In most cases it is negligible compared to the light emitted by the scintillator [58].

1.7 Organic Photodiodes

As discussed above the main limitation of PSDs is the Cerenkov radiation produced in the optical fiber contaminating the signal. An attractive proposition to avoid Cerenkov contamination is to remove the optical fiber and couple the scintillator directly to an optical sensor to measure the light output of the scintillator. Photodiodes make a suitable light detector. However, silicon-based photodiodes would likely introduce perturbations of the radiation field in a manner similar to previously described for silicon diodes that are used in certain dosimetry applications [31]. Furthermore, silicon diodes would introduce a substantial signal due to interactions within the silicon. Organic photodiodes offer a promising alternative as the organic semiconductors making up the active layer of the photodiode has a composition that is similar to human tissue in terms of their radiological characteristics (i.e. effective atomic number, electron density, etc.). Organic photodiodes are commonly used as solar cells. There is a large volume of research characterizing organic photodiodes (absorption spectrum, efficiency, etc.) which will allow us to select a suitable composition for our needs. Although we expect a significantly smaller signal will be generated directly in the photodiode by ionizing radiation compared to silicon diodes, the magnitude of this contribution to the measured signal will need to be quantified.

Light emitted from the scintillator needs to be absorbed by the organic diode and converted into an electrical signal. The processes inherent to this signal generation include: light absorption, exciton (bound electron-hole pair) creation and diffusion, charge separation, charge transport, and charge collection.

1.7.1 Signal Generation

For light to be converted into a signal, it first needs to be absorbed by the organic semiconductors of the photodiode. The wavelengths of light that can be absorbed by the organic semiconductors is determined by the bandgap. The percentage of light absorbed depends on the thickness of the film as well. Unfortunately, due to the low charge carrier and exciton mobilities of organic semiconductors the film has to be made thin and so cannot collect all of the incident light. Upon the absorption of light, an exciton (an electron and hole pair bound together due to electrostatic Coulomb force) is created [59]. Exciton diffusion is needed for the bound exciton to reach a dissociation site. In many polymers, the diffusion length (the average length a carrier travels from generation to recombination) is only 10 nm [59, 60]. If the exciton does not reach a dissociation site in time, it will recombine and the absorbed photon will not produce a measurable signal. Charge separation can occur at a semiconductor/metal interface or at the interface of two materials with sufficiently different electron affinities (EA) and ionization potentials (IA). In the latter case one material acts as an electron acceptor, while the other material acts as an electron donor since it transferred an electron to the acceptor. If the difference in EA and IA is insufficient, the exciton may migrate to the material with the lower bandgap without splitting its charges and will eventually recombine. Next, the separated charge starts to transport to the electrodes. As the charge moves it may interact with atoms or other charges, slowing down its travel. Furthermore, recombination can happen along the journey and is worse

when one material serves as the transport medium for both electrons and holes. For the charge to enter the electrode material it may have to overcome a potential barrier of a thin oxide layer.

1.7.2 Photodiode Architecture

The efficiency with which an organic photodiode absorbs light and generates a current depends on the device architecture. Various architectures have been studied, including: single layer, double layer heterojunction, and a bulk heterojunction (BHJ). A single layer photodiode consists of one semiconductor sandwiched between two electrodes (figure 1.14). Exciton dissociation occurs near the interface between the semiconductor and one of the electrodes. Since electrons and holes flow through one material there is a high rate of recombination. A double-layer diode consists of two semiconductors layered between the electrodes. One semiconductor acts as an electron acceptor which will allow electrons to flow to the low work function electrode and one will act as an electron donor and allow holes to flow to the higher work function electrode. Using a donor-acceptor heterojunction greatly increases the efficiency of exciton dissociation. However, for the excitons to be harvested they must be within a diffusion length of the interface, otherwise they will recombine and not contribute to photocurrent. To increase the probability of exciton dissociation, a BHJ photodiode is made by mixing the two semiconductors together, either by spin-coated solution of both materials, or by co-evaporation in vacuum deposition. This results in domains of the two materials which will increase the interface area, decrease the mean distance between exciton generation and an interface, and can still form a network to provide a path for the charges to transport to the electrodes. The photocurrent generation highly depends on the domain sizes of the two semiconductors, which depends on the deposition method, the solvent used, the annealing conditions, etc.

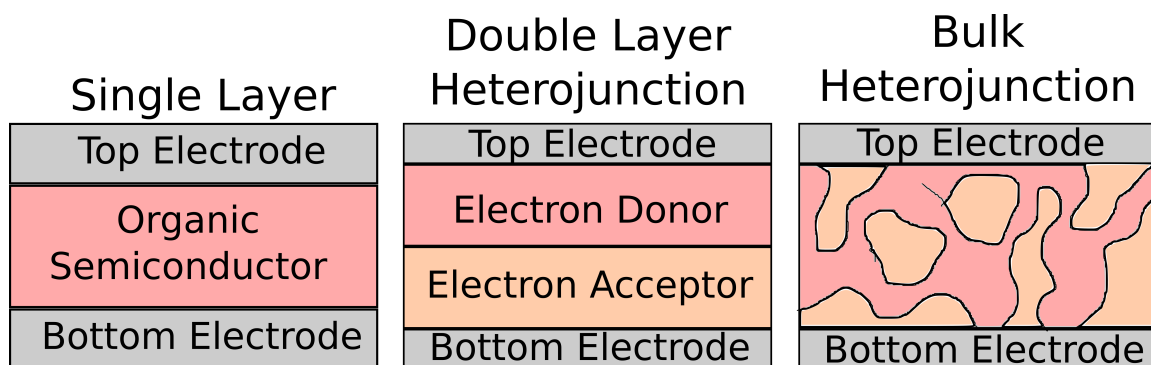


Figure 1.14: Various architectures of organic photodiodes. In our work we use a bulk heterojunction which is designed to increase the probability of exciton dissociation, by increasing the interface area between the electron donor and acceptor materials.

1.7.3 P3HT/PCBM BHJ Photodiode

In our work we fabricated P3HT/PCBM BHJ organic photodiodes. These devices have been shown to have power conversion efficiencies (PCE) of approximately 2 – 4 % [61, 62, 63]. When selecting a photodiode for our detector, it is more important to select a photodiode that has high efficiency at the wavelengths of light emitted by the scintillators. The external quantum efficiency (EQE) gives a ratio of the number of charge carriers collected by the photodiode to the number of photons shining on the photodiode at each energy. For P3HT/PCBM BHJ photodiodes the EQE is approximately 40 - 60 % at wavelength of 350 - 600 nm, which covers most of the light emitted from the scintillators used in this work [64, 65].

1.7.4 Operating Characteristics of Organic Photodiodes

Figure 1.15 shows a current-voltage (I-V) curve for a typical photodiode in the dark and a typical photodiode when illuminated. A typical photodiode in the dark has some threshold voltage that needs to be applied to conduct a current. The

current increases exponentially with the bias applied. When the photodiode is illuminated, photons are absorbed creating charge carriers (electron-hole pairs). Separating and collecting the charge carriers creates a current as discussed above. This illumination current (I_L) has the effect of shifting the I-V curve down. A term for the current flowing through the photodiode while unbiased is the short-circuit current (I_{SC}). In the dark it would be zero and when illuminated the magnitude would increase with the intensity of the illumination (i.e. proportional to the number of incident photons). In our work we operate the photodiode unbiased (i.e. we measure the short-circuit current).

1.8 Detector Design and Motivation

Radiotherapy should be used as part of treatment for approximately half of all cancer patients [2]. Radiotherapy is a balancing act between sparing healthy tissue and delivering a high enough dose to control the disease. Radiotherapy treatments are becoming increasingly complex with small fields and high dose gradients to deliver larger doses to the disease while sparing healthy tissue. Therefore, it is of paramount importance to have accurate detection and quantification of small radiation fields to ensure effective and safe use of radiation treatment.

Two areas of potential application for the devices studied in this work include patient specific dose verifications, and linear accelerator quality assurance in stereotactic radiosurgery (SRS) applications. Patient specific dose verifications involve recalculating a patient's treatment plan on a phantom into which a detection system has been inserted. The plan is then delivered on the treatment unit and the measured dose distribution is compared to the calculated plan. Differences between the two can identify failure modes that include poor treatment beam modeling in the planning system and imperfections in the mechanical delivery (e.g. MLC leaf

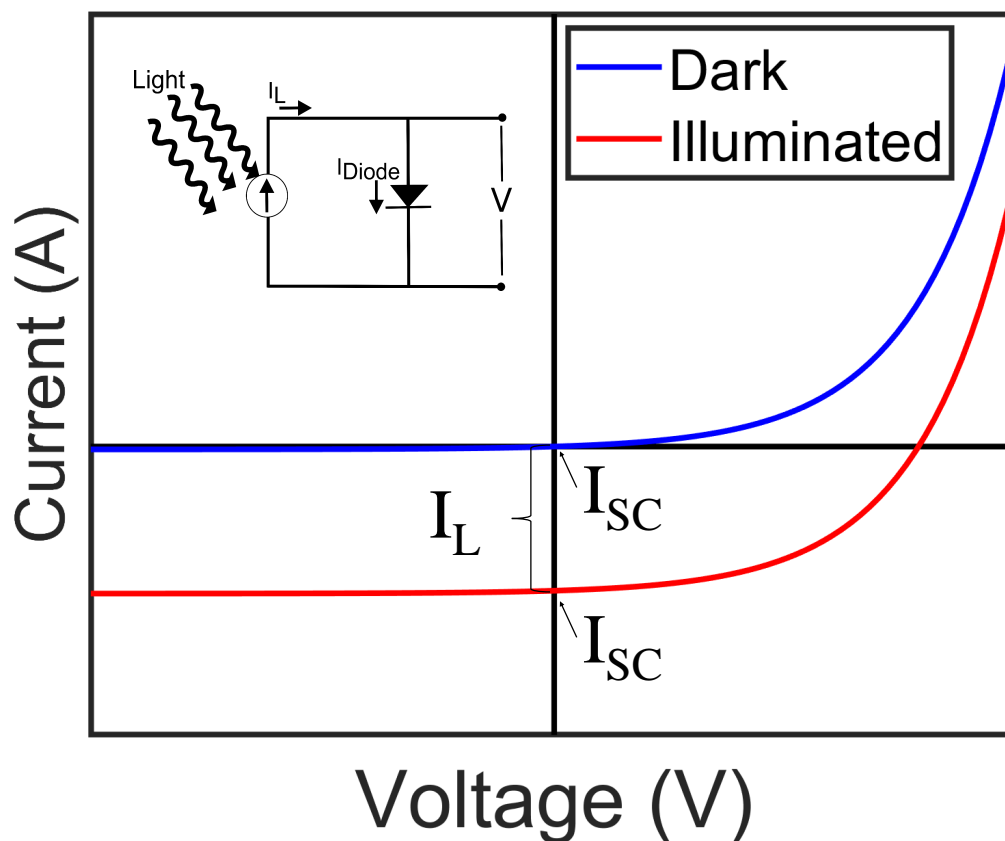


Figure 1.15: I-V curve of a typical photodiode in the dark and a typical photodiode while illuminated. Illumination creates a current (I_L), which shifts the I-V curve down in the diagram. The current measured with no applied bias is the short circuit current (I_{SC}) and depends on the intensity of the illumination (i.e. the number of incident photons).

position issues, potentially caused by high levels of aperture modulation). Such failures can result in adjustments to the plan before the patient is treated, which gives greater confidence the patient is receiving an acceptable treatment plan.

The SPSD is a detector that is well positioned to address the specific needs of SRS applications because it could maintain the benefits of PSDs, remove the Cerenkov contribution, and no significant signal is expected from the photodiode. Studies have shown PSDs may not have some of the same limitations as other dosimeters mentioned [36]. PSDs are advantageous as high energy dosimeter because they

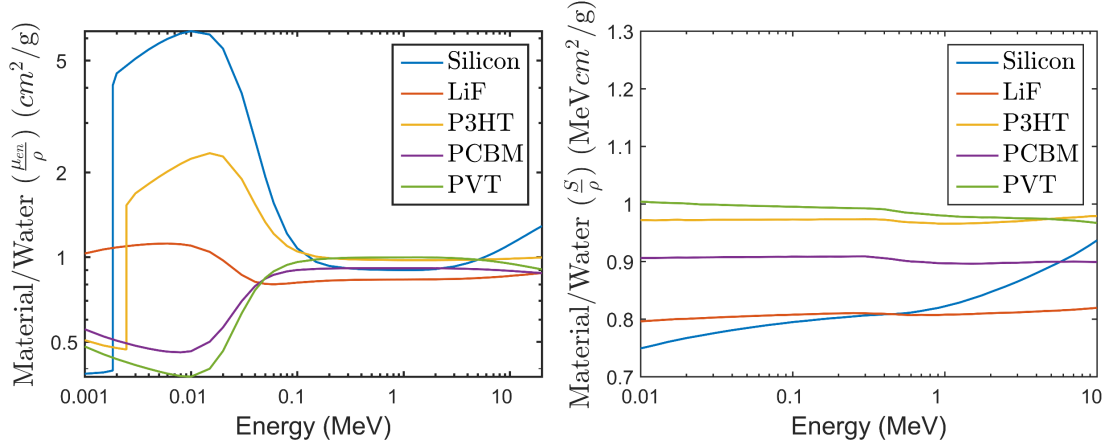


Figure 1.16: a) The mass attenuation coefficient ratio of several materials to that of water. b) The stopping power ratio of several materials to that of water. The materials P3HT, PCBM, and PVT will be used in the construction of our SPSD and Si and LiF make up some commonly used dosimeters for comparison. Data retrieved from NIST [4]

have immediate response, are nearly water-equivalent, long usable lifetime, and have high spatial resolution [47, 57]. Furthermore, PSDs have a field output correction factor of 1.000 down to the smallest field sizes listed in TRS-483 (0.4 x 0.4 cm²), making them ideal for small field dosimetry. The main limitation of PSDs is the Cerenkov radiation which can contaminate the signal. By removing the optical fiber our SPSD could reduce the amount of Cerenkov produced.

We employ an organic photodiode to reduce the perturbation of the radiation beam (i.e. the organic materials are more water-equivalent than a silicon photodiode). The photon cross-section ratios and stopping power ratios of the materials present in our detector (P3HT and PCBM) show less of an energy dependence than silicon, suggesting their performance should not be inferior to that of silicon diodes (figure 1.16). These characteristics mean that this detector could be ideal for use in small field radiation beams.

1.9 Research Objectives

This thesis presents novel work on a detector comprising of an organic photodiode coupled to an organic scintillator. Using this design eliminates the need of an optical fiber to measure the response of the organic scintillator and could drastically reduce the Cerenkov (contaminating signal) produced. This thesis methodically explores each element of the detector system and culminates with the evaluation of a functional 1D array of SPSSDs. This thesis consists of a series of manuscripts, each address a key research objective:

- Manuscript 1 presented in chapter 3. This manuscript investigates the use of an organic photodiode as a radiation detector directly. Presented is a novel method for correcting the current produced in the electrodes, wires etc. (stem current), of a photodiode by replacing the semiconducting layers of the photodiode with a dielectric layer. Various radiation dependencies are presented before and after the correction. Reference [66]:

– Hupman, Michael A, Irina Valitova, Ian G. Hill, and Alasdair Syme. 2020. “*Radiation Induced Photocurrent in the Active Volume of P3HT/PCBM BHJ Photodiodes.*” *Organic Electronics* 85:105890.

- Manuscript 2 presented in chapter 4. This work is a more detailed explanation behind the methods used to remove the stem effect from the signal generated by a diode in a radiation beam presented in manuscript 1. A device where the active volume of the diode is replaced with a dielectric polystyrene which should have no measureable current due to the separation of radiation induced charged in the active layer. Therefore, any current measured should be due to interactions in the connecting electrodes, wires, etc. Reference [67]:

- Hupman, Michael A, Irina Valitova, Ian G. Hill, and Alasdair Syme. 2020. “Method for the Differentiation of Radiation-Induced Photocurrent from Total Measured Current in P3HT/PCBM BHJ Photodiodes.” *MethodsX* 7:101125.

- Manuscript 3 presented in chapter 5. In this work an organic scintillator was coupled to an organic photodiode to fabricate a novel radiation detector: stemless plastic scintillation detector (SPSD). This work makes use of the low sensitivity of the diodes characterized in Manuscripts 1 and 2. Although the thin active volume of the diode means its sensitivity to ionizing radiation is low, it is still thick enough to absorb a high percentage of the light emitted by the scintillator. Various dependencies of the detector are presented including: instantaneous dose rate dependence, energy dependence, directional dependence, and linearity with dose. Reference [68]:

- M. A. Hupman, T. Monajemi, I. Valitova, I. G. Hill, and A. Syme, “Fabrication and Characterization of a Stemless Plastic Scintillation Detector,” *Medical Physics*, vol. 47, pp. 5882–5889, Nov 2020

- Manuscript 4 presented in chapter 6. This work is an extension of the work presented in manuscript 3, but the detector was extended into a 1D array for the use in small fields. First, an array of diodes were fabricated with a long piece of scintillator placed on top and the response measured, particularly profiles of small fields. This design was then improved upon by laser etching the scintillator to create septa in the scintillator between pixels to decrease the cross-talk. Manuscript “Measuring Small Field Profiles and Output Factors with a Stemless Plastic Scintillator Array”, authored by Michael Hupman, Ian Hill, and Alasdair Syme, has been submitted to the journal of *Medical Physics* (April 20, 2021).

In chapter 2 the methods used for the fabrication of the diodes, the cutting

and polishing of the scintillators, and the irradiation setup and measurement conditions used to measure various dependencies of the detectors are presented. Chapter 7 concludes the thesis by summarizing the key findings of the manuscripts and hypothesizes on the future directions of this work.

Chapter 2

Methods

In this chapter the methodologies used for the work in this thesis are described. First, the techniques used to fabricate the stemless plastic scintillation detector (spin coating, physical vapour deposition, scintillator cutting and polishing) will be explained. Next, the setup used to irradiate the detector and measure various dependencies (dose per pulse, energy dependence, etc.) will be explained. Several commercial detectors were used in this work to compare the response of our detector to and there setup will be described. Furthermore, the rationale behind the choice of detector for a given task will be explained.

An organic photodiode was fabricated in this work. Organic photodiodes are appealing for radiation detection because they offer a high degree of customization when it comes to the choice of materials (absorption spectrum, atomic number, density, etc.) and the geometry of the device. The materials used for our semiconductor are a well-studied design selected partly due to the good overlap of the absorption spectrum of the semiconductors with the emission spectrum of the scintillators. In the future organic photodiodes can be made on flexible substrates which could lead to novel applications such as in vivo dosimetry.

2.1 Stemless Plastic Scintillator Detector (SPSD) Fabrication Techniques

2.1.1 Substrate Preparation and ITO Etching

Fabrication started with an ITO coated glass substrate. The ITO was etched by placing electroplating tape over the desired electrode area. The substrate was placed in hydrochloric acid (HCl) for 6-8 minutes which removed the ITO that was not covered by the tape. The tape was then removed and the substrate cleaned to remove any adhesive residue and other contaminants. The substrate was sonicated in successive solutions of Sparkleen (Thermo Fisher Scientific, Waltham, USA) and deionized (DI) water, DI water, acetone, and ethanol for approximately 20 minutes each, followed by UV-ozone for 20 minutes to complete the cleaning procedure.

2.1.2 Spin Coating

Spin coating is used to deposit a thin film of material evenly across a substrate [69]. The typical first step is to dissolve the material to be deposited into a solvent. Next, the substrate is placed in the spin coater on a pedestal and held in place using a vacuum. The solution is deposited onto the substrate (usually with a pipette) and then spun at high speeds which flings the majority of the solution off of the substrate (figure 2.1). Decreasing spin speed (typical range of approximately 500 – 8000 rpm) or increasing the concentration of the solution creates a thicker film. The combination of centripetal force and surface tension leaves the substrate evenly covered by the film (root mean square surface roughness ≤ 1 nm) [70]. Air flow assists the drying of the solvent, leaving only a film of the desired material. The duration of spin coating depends on how long it takes for the solvent to evaporate (usually 1 minute, but can be longer depending on the solvent). The parameters of spin coating (spin speeds, concentration, temperature, solvent choice, etc.)

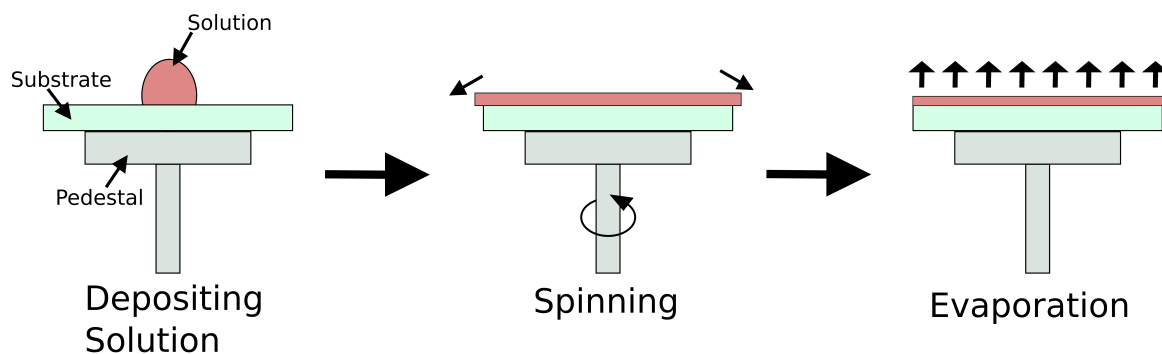


Figure 2.1: Spin coating is a technique for evenly depositing a thin film of material. First the material is dissolved in a solvent and placed onto the substrate (substrate held on pedestal using a vacuum). Next, the substrate is spun quickly which flings off much of the material and leaves an even covering of the surface. Air flow and a hot plate may be used to aid in the dissolving of the solvent to leave only the desired material behind.

have been optimized in the solar cell literature and established methods were used.

2.1.3 Physical Vapour Deposition

Physical vapour deposition is a technique used for precisely depositing films of a material (aluminum for our SPSPD) (figure 2.2) [71]. This process takes place in a vacuum of less than 6×10^{-6} Torr. The material to be deposited is placed into a basket (often tungsten), which has a higher evaporation temperature. To heat the material, a current is passed through the basket via a power supply. The current is increased to heat up the deposition material and basket until the material evaporates. The evaporated material flows in straight lines until it contacts a cool surface and condenses. By placing a mask in front of the substrate to block areas where the deposited material is unwanted, a precise pattern of material is deposited onto the substrate. A shutter is placed in front of the substrate during the heating stage to prevent deposition until the desired rate of deposition is reached (usually 1 \AA/s). Furthermore, the shutter blocks the substrate until approximately 50 \AA of material is wasted to ensure any contaminants on the surface are evaporated off. When the desired thickness is reached the shutter is used to block the substrate again.

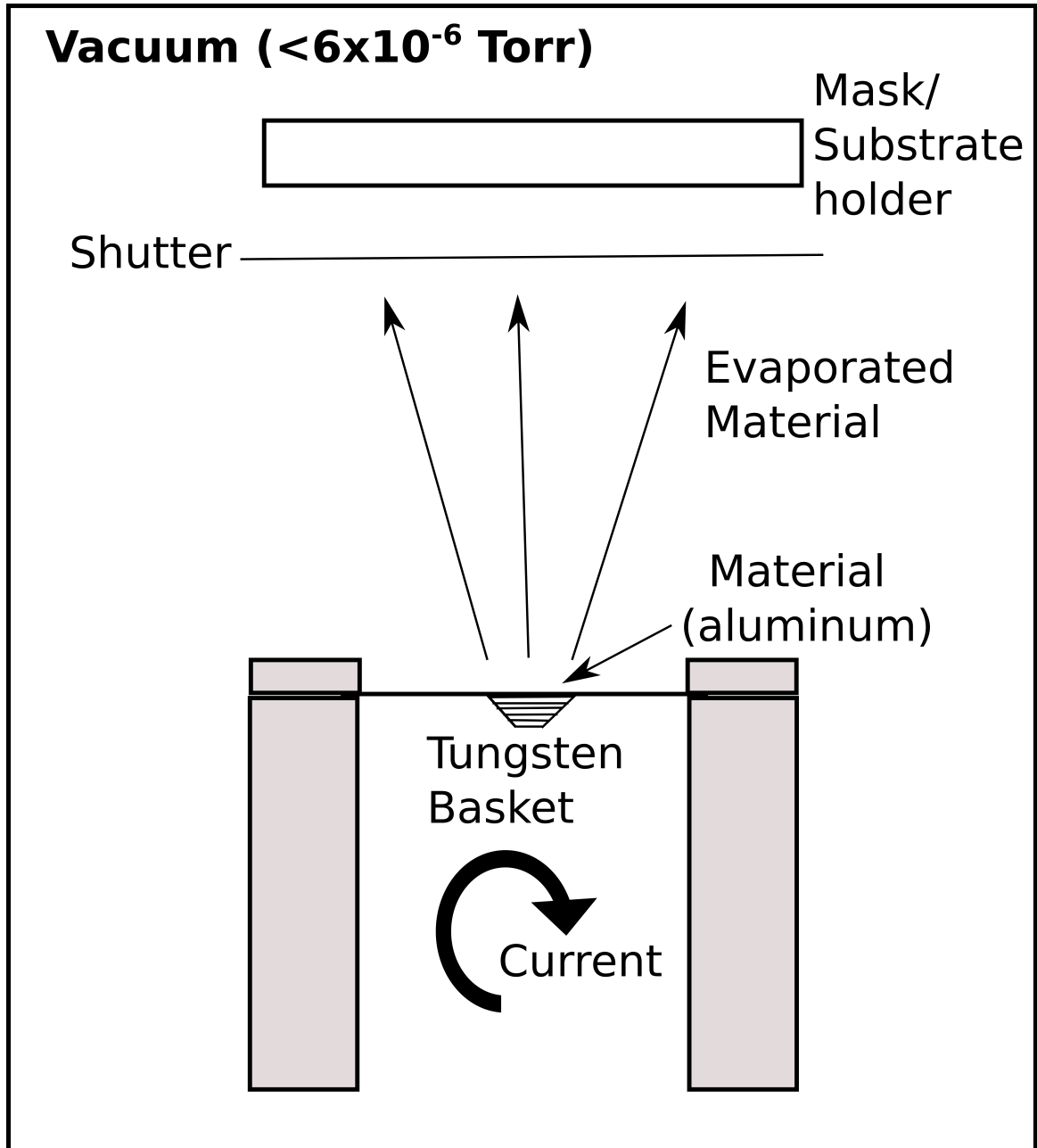


Figure 2.2: Physical vapour deposition is a technique used to deposit a material onto a substrate in a precise pattern. The material is placed in a basket, which, is heated by flowing a current through it. The material evaporates and flows in straight lines until it makes contact with a cool surface and condenses. By placing a mask in front of the substrate a precise pattern of material is deposited onto the substrate.

2.1.4 Full Fabrication Process

Fabrication of P3HT/PCBM BHJ photodiodes followed established procedures from the literature [61, 62, 63]. The photodiodes were fabricated on a glass substrate with an indium tin oxide (ITO) bottom electrode (figure 2.3). The glass substrate was initially coated with ITO. The ITO electrode was patterned by placing electroplating tape over contact areas and the substrate is placed in 12 M HCl for approximately 6 minutes to etch away the uncovered ITO. The substrates were cleaned by placing them for 20 minutes in successive solutions of deionized water with Sparkleen (Thermo Fisher Scientific, Waltham, USA), deionized water, acetone, and ethanol, followed by 20 minutes in UV-ozone. Next PEDOT:PSS (Clevious P VP Al 4083, Heraeus, Hanau, Germany) was spin coated on the substrate for 60 s at 5000 rpm and placed on a hot plate at 150 °C for approximately 30 minutes. Next a solution of equal parts P3HT (Brilliant Matters, Quebec City, Canada) /PCBM (Solenne BV, Groningen, Netherlands) in chlorobenzene was spin coated (concentration and spin speeds differed based on the desired thickness) and placed on a hot plate at 110 °C for 1 hour. To make contact with the underlying ITO, a razor was used to scratch through the P3HT/PCBM layer at one end (the ITO extended beyond the top electrode laterally to allow the connection). Next, aluminum top contacts were deposited using physical vapour deposition of 1 Å/s to a thickness of 80 nm. Lastly, the devices were encapsulated using an epoxy (ossila, Sheffield, UK), which was cured using a UV light for 20 minutes (50-100 μm). The thickness of the epoxy was done in an uncontrolled way leading to a large uncertainty in the exact thickness, but yielded reproducible devices.

As a control, devices were made by replacing the P3HT/PCBM semiconductors with the dielectric polystyrene (PS) (Sigma-Aldrich, St. Louis, USA) (figure 2.4). This was done by spin coating a solution of PS in toluene (the concentration

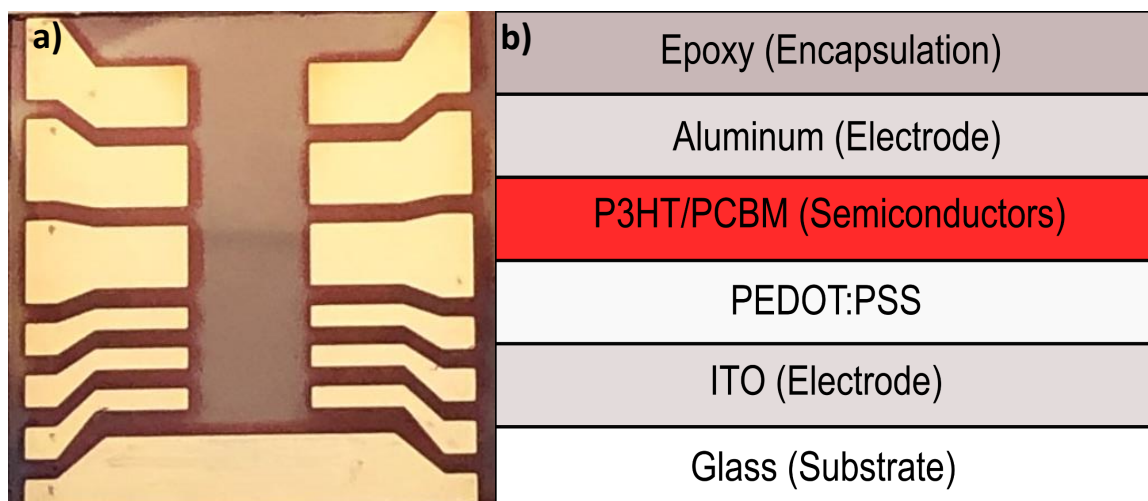


Figure 2.3: a) A photo of the photodiode. The red colour is due to the semiconductors (P3HT/PCBM), and each of the silver strips on the sides are aluminum (top electrode) and contact to a different photodiode. b) A schematic showing the various layers that make up the photodiode.

and spin speed were chosen to match the thickness of the P3HT/PCBM photodiodes). We expect no photocurrent to flow through this control device (i.e. the device should not function as a diode). Any measured current during irradiation is due to current originating in the electrodes, wires, and surroundings.

2.1.5 Scintillator Preparation

Scintillators were received from the manufacturer in a large sheet of either 2 mm or 5 mm thickness. The scintillators were cut to the desired size using a band saw. This left the sides of the scintillators rough. The sides of the scintillators were polished by sanding with progressively finer grit sand paper. Hereafter, a scintillating element coupled to an organic photodiode will be referred to as a stemless plastic scintillation detector (SPSD). For a single-element PSD, the scintillators were cut to approximately $5 \times 5 \times 5 \text{ mm}^3$ for three Eljen (Eljen Technology, Sweetwater, TX, USA) scintillators (EJ-204, EJ-208, and EJ-260) and approximately $3 \times 3 \times 2 \text{ mm}^3$ for two Saint-Gobain (Saint-Gobain, Courbevoie, France) scintillators (BC-400

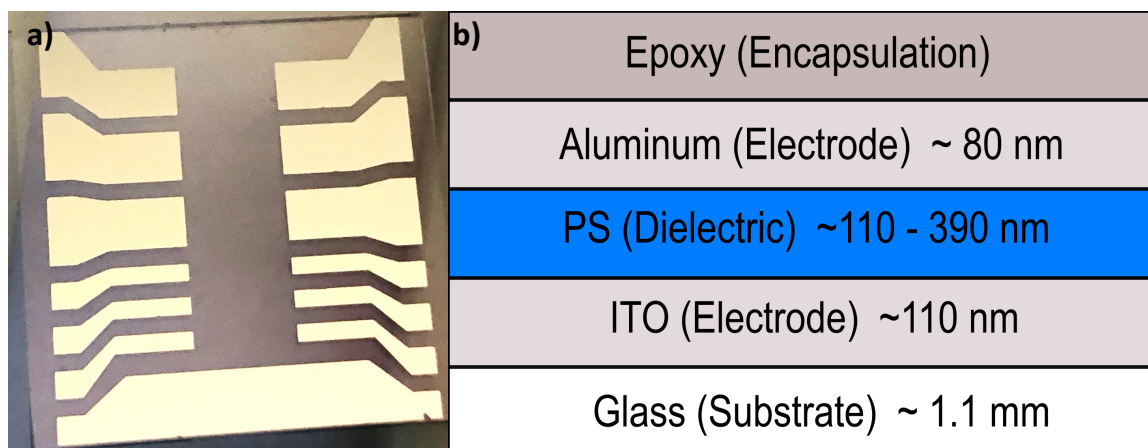


Figure 2.4: a) A photo of the polystyrene (PS) device. Polystyrene is clear in colour. b) A schematic showing the various layers that make up the device and their approximate thicknesses.

and BC-412) (figure 2.5). For more complex scintillator designs (i.e. segmented with septa to create an array), the scintillator was segmented using a Bodor 40 W CO₂ laser etcher (wavelength 10.6 μm) (Bodor Ltd., Jinan City, China). Next, black paint was deposited into the air gaps to decrease the cross-talk. After painting, the top surface was polished as before. After the scintillator was polished it was placed on the backside of the glass substrate containing the photodiode with the aid of an optical coupling gel (EJ-550) (Eljen Technology, Sweetwater, TX, USA).

2.2 Detector Setup

2.2.1 Measurement of Detectors

During irradiation a dual channel Keithley source measurement unit (SMU) (Keithley 2614B, Tektronix, Inc., Beaverton, USA) was used to measure the current flowing through the photodiode. No bias was applied to the photodiodes while the current was measured (i.e. the short-circuit current was measured). To make contacting the diodes more reliable a holder was made using a 3D printer (figure 2.6). The holder had pogo pins placed into it to make contact with each diode. Next a

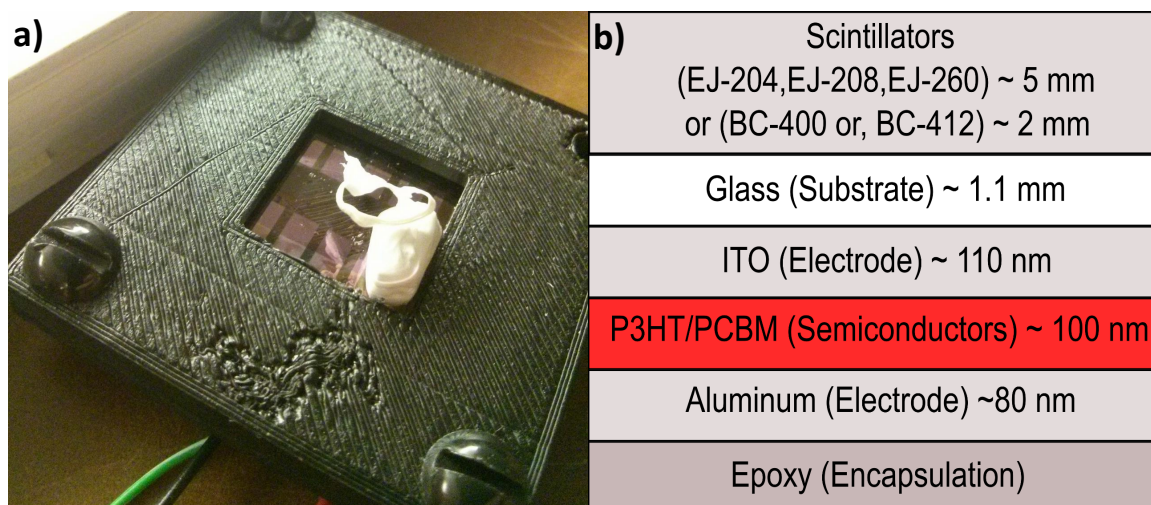


Figure 2.5: a) On the left is a picture of the SPSP. The white is a reflective tape around the scintillator. The black is a 3D printed holder to allow easy and reliable contact to the device. For irradiation the air gaps would be filled in with 3D printed material. b) A schematic of the SPSP with approximate thicknesses of each layer.

wire was soldered from the pogo pins. When measuring the photodiodes or a single SPSP, a triaxial cable with alligator clips at the end were connected to the ends of the wires for measurement (figure ??a). When measuring the array each wire was soldered to a binding post placed outside of the beam (figure ??b). This created an organized way to switch between each diode, with less chance of breaking a contact due to strain on the wires.

2.2.2 Extraction of Photocurrent

To measure the current flowing through the photodiode during irradiation, two Keithley Source Measurement Units (SMUs) were used. Independent measurements of the electrodes was achieved by attaching one SMU to the ITO electrode and one to the aluminum electrode to help distinguish the contribution of the signal due to a radiation induced photocurrent and from an undesired contribution. This undesired contribution was hypothesized to be induced in the electrodes, wires, etc.

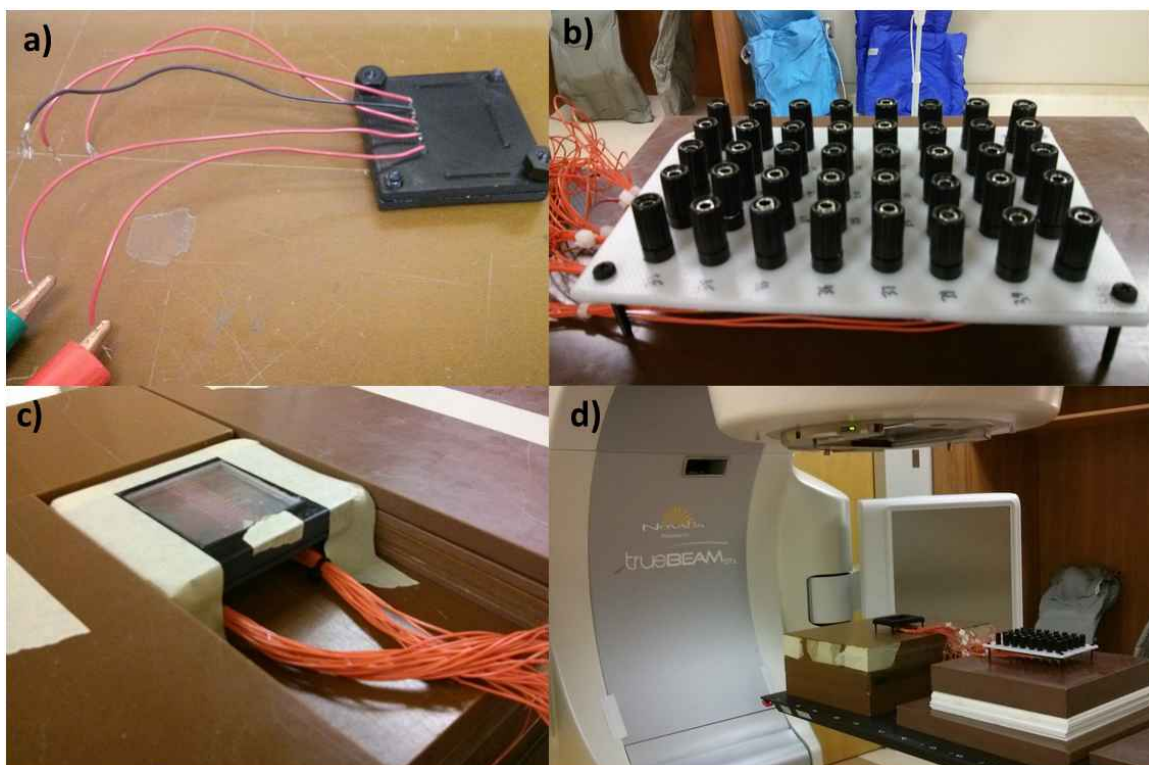


Figure 2.6: a) Alligator clips attached to a couple wires connected to a single SPAD device. The Bottom of the 3D holder is pictured to show the wires attached to pogo pins which make contact with the photodiodes. b) An array of binding posts with each contact soldered to allow easy switching between which photodiode is going to be readout. c) Photo of the SPAD array. d) Photo showing the array holder in the irradiation beam. The binding post array is away from the beam so that the alligator clips are not within the beam. For irradiation measurements solid water fully surrounds the array.

due to a shower of high energy electrons induced by the radiation beam (i.e. Compton current) [23, 72]. A signal comprised solely of radiation-induced photocurrent would see electrons extracted by the aluminum electrode (measured a positive current on the SMU) and holes extracted by the ITO electrode (measured a negative current on the SMU), but of equal magnitude. However, the irradiation produces Compton current originating in the electrodes/wires which will result in electrons being measured by both electrodes (measured positive). The result is that current measured on the aluminum electrode is a combination of the photocurrent and Compton current. Meanwhile, on the ITO electrode the photocurrent would oppose

the Compton current. To extract the photocurrent the current measured with the PS device (purely Compton current) was subtracted from the P3HT/PCBM BHJ photodiode for each electrode. The net current after subtracting should be solely due to photocurrent, which would be negative on the ITO electrode and positive on the aluminum electrode, but of equal magnitude. A more thorough explanation of this correction technique and evidence for its efficacy is given in Chapter 4. The technique was continued for some experiments with the SPSD, but due to a much higher signal, the Compton current was often insignificant and subtracting it did not change the results.

2.3 Irradiation Setup

The photodiodes and SPSDs were irradiated using both an Xstrahl 300 orthovoltage X-ray unit (Xstrahl Ltd., Surrey, UK) (100, 180, and 300 kVp) and a TrueBeam medical linear accelerator (Varian Medical Systems Inc., Palo Alto, USA) (6 and 10 MV photons, and 16 MeV electrons). A calibrated ionization chamber was used to measure all machine outputs. For Orthovoltage irradiations the detectors were placed on top of a 15 cm stack of Solid Water (Sun Nuclear Corp., Melbourne, USA) and a cone of 5 cm diameter and 30 cm length was used to deliver dose (figure 2.7). For megavoltage irradiations, reference measurements were performed with the detectors placed at isocenter of a 10x10 cm² field, with a 95 cm source-to-surface distance (SSD) and 5 cm of solid water was placed on top of the device for build-up (figure 2.8). During irradiation the current or charge of the detector was measured using a dual SMU while unbiased.

Various dependencies of the detectors were measured by varying the setup. Linearity was measured by placing the detector in reference conditions and delivering 1-1000 cGy with a 6 MV photon beam. Sensitivity of the devices was then determined from the slope of the line and stated in nC/cGy. Dose rate dependence

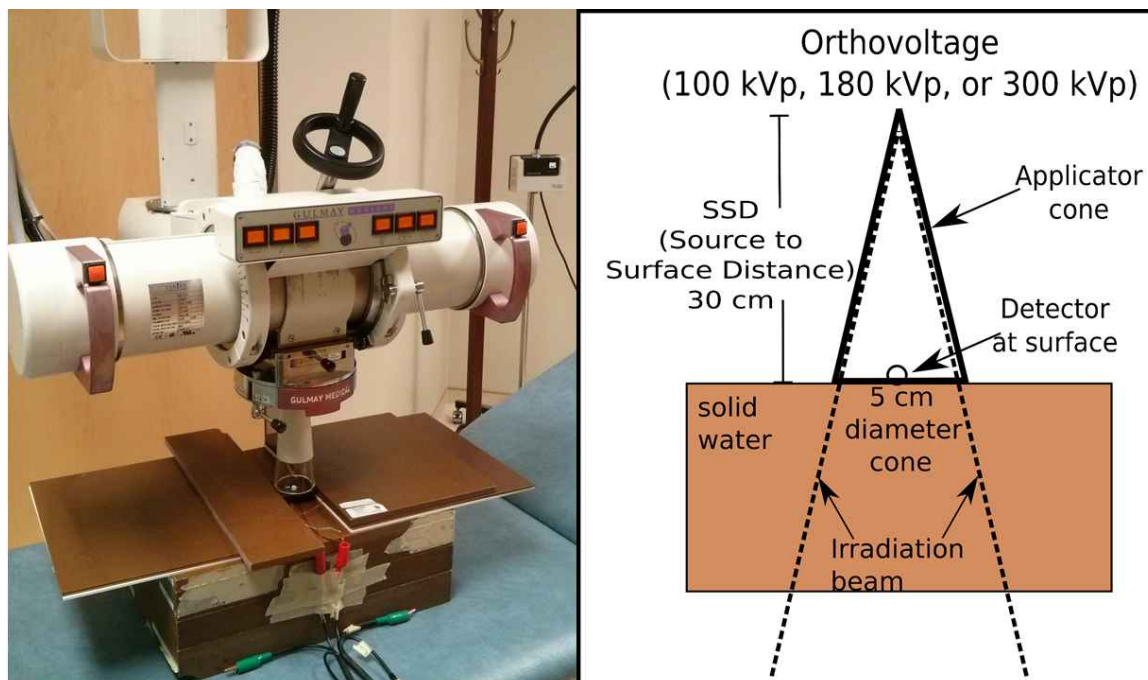


Figure 2.7: On the left is a picture of the orthovoltage unit setup for irradiations using kV photon beams. On the right is a schematic of the setup.

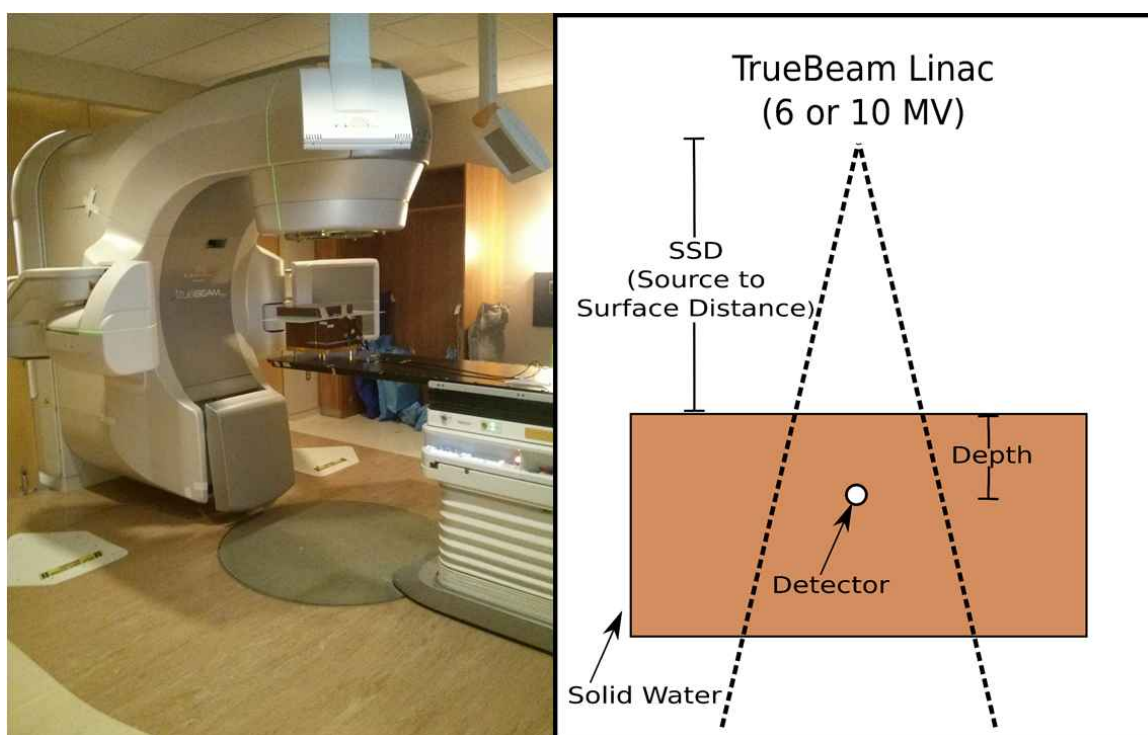


Figure 2.8: On the left is a picture of the setup used to irradiate our devices with a TrueBeam Linac. On the right is a schematic showing the setup.

was measured by delivering 200 cGy with dose rates average dose rates ranging from 100-600 cGy/min.

The dose per pulse dependence was measured with reference conditions except the SSD was varied between 80 and 125 cm. The charge per dose at each SSD was calculated from measurements with an Exradin A12 ion chamber (Standard Imaging, Middleton, WI, USA). The data was then normalized to both the dose per pulse and charge per unit dose at an SSD of 95 cm and the dependence quantified.

Output factors were measured by irradiating the detectors with 200 MU with a 6 MV photon beam for field sizes between $0.5 \times 0.5 \text{ cm}^2$ and $25 \times 25 \text{ cm}^2$. Output factors are defined by the signal at a given field size to the signal measured at the reference field size ($10 \times 10 \text{ cm}^2$). As a comparison an Exradin A12 ion chamber was used for $4 \times 4 \text{ cm}^2$ to $25 \times 25 \text{ cm}^2$ field sizes. When the field size is smaller than $4 \times 4 \text{ cm}^2$ the large size of the Exradin A12 ion chamber leads to volume averaging which results in an under-response. At a field size of $4 \times 4 \text{ cm}^2$ a semiflex 31010 micro ion chamber (PTW, Freiburg, Germany) was cross-calibrated with the Exradin A12 ion chamber (a process known as daisy-chaining). The micro ion chamber was used for field sizes of $1 \times 1 \text{ cm}^2$ to $4 \times 4 \text{ cm}^2$. The micro ion chamber cannot be used for large field sizes because the small volume results in a low signal and the signal due to the stem effect becomes significant. Similarly, a PTW 60019 microDiamond (PTW, Freiburg, Germany) was irradiated for small fields of $0.5 \times 0.5 \text{ cm}^2$ to $4 \times 4 \text{ cm}^2$. Both the diamond and micro ion chamber measurements were corrected using output correction factors in TRS-483 [6].

Percent depth dose curves (PDDs) were measured by placing various thicknesses (0 to 15 cm) of solid water on top of the detectors and the treatment couch was shifted down to ensure a constant SSD of 100 cm. The signal at each depth was then normalized to the maximum signal to obtain the PDD. For SPSD measurements the point of measurement was taken to be at the midpoint of the scintillator.

The PDDs were compared to CC13 ion chamber (Blue Phantom, IBA Dosimetry, Schwarzenbruck, Germany) measurements in a water tank (Blue Phantom, IBA Dosimetry, Schwarzenbruck, Germany).

Directional dependence was measured at the surface with the large scintillator SPSDs with 16 MeV electrons, SSD of 107 cm, and gantry angles between 0 and 45. 16 MeV electrons were selected to maximize the Cerenkov contribution to the signal. The couch was shifted at each gantry angle to ensure the SPSD was located along the central axis of the beam. This caused an increased distance from the source to the detector and decreased the dose. For this reason, SPSD measurements were compared to a PTW 60019 microDiamond, which has been shown to have low angular dependence [35]. Measurements were repeated at a depth of 3 cm, which should have a smaller directional dependence because electron scattering should result in a more isotropic Cerenkov emission in comparison to the surface.

A 1-dimensional array of SPSDs was used to measure profiles of small fields. The array was calibrated by irradiating it in a 10x10 cm² field under reference conditions and the response of each pixel measured. Next, the array was shifted one pixel and irradiated again under reference conditions. With these two measurements the dose to a pixel in measurement 1 is the same as its neighbor in measurement 2. The response of each pixel as a function of dose can then be determined by chaining the response of a pixel to the next pixel closer to the center and so on until the center of the field where the dose is known. This results in each pixel having a correction factor which can convert the signal to a dose. The array was irradiated with 0.5x0.5, 1x1, and 2x2 cm² field sizes with the response of each pixel measured and corrected. The profiles were compared to film measurements.

EBT3 Gafchromic film (Ashland Specialty Ingredients, Bridgewater, NJ) has excellent spatial resolution and low energy dependence making it a good choice for small field profiles. The film was readout using an EPSON EXPRESSION 10,000

XL scanner (Epson, Suwa, Japan). The film was readout using 48 bit colour-depth, a resolution of 300 dpi, and pre-scanned seven times to ensure uniform heating of the bulb. After irradiating the film it was allowed to develop for 24 hours before scanning. To calculate the dose to the film a triple-channel film dosimetry algorithm described in Mayer et al. was used [73]. The triple-channel method was selected because it reduces uncertainty compared to using a single channel approach, which results in an uncertainty of 2-4% depending on the dose (in field or outside the field), resolution, etc [29, 73]. The correction method was implemented by first irradiating film at reference conditions with various known doses. The colour percent of each colour channel as a function of dose was computed and shown in figure 2.9. A look up table (LUT) was created by fitting a function to the response of each channel. The fit used the equation:

$$PC = \frac{a + D * b}{c + D} \quad (2.1)$$

Where D is the known dose, PC is the percent colour (for each channel), and a, b, and c were the fit parameters. After having the lookup table the dose to a film irradiated in non-reference conditions is calculated using the formula derived by Mayer et al. The formula for calculating dose to a pixel in location i,j is:

$$D(i, j) = \frac{D_{ave}(i, j) - (RS(i, j)) \frac{\sum_{k=1}^3 D_k(i, j) a_k(i, j)}{\sum_{k=1}^3 a_k(i, j)}}{1 - RS(i, j)} \quad (2.2)$$

Where D_{ave} is the average dose of the three channels, k is an index that spans the three colour channels, RS is the relative slope for the channels, and a_k is the slope of each colour channel. In equation form those were calculated by the following:

$$D_{ave} = \frac{1}{3}(D_R(i, j) + D_G(i, j) + D_B(i, j)) \quad (2.3)$$

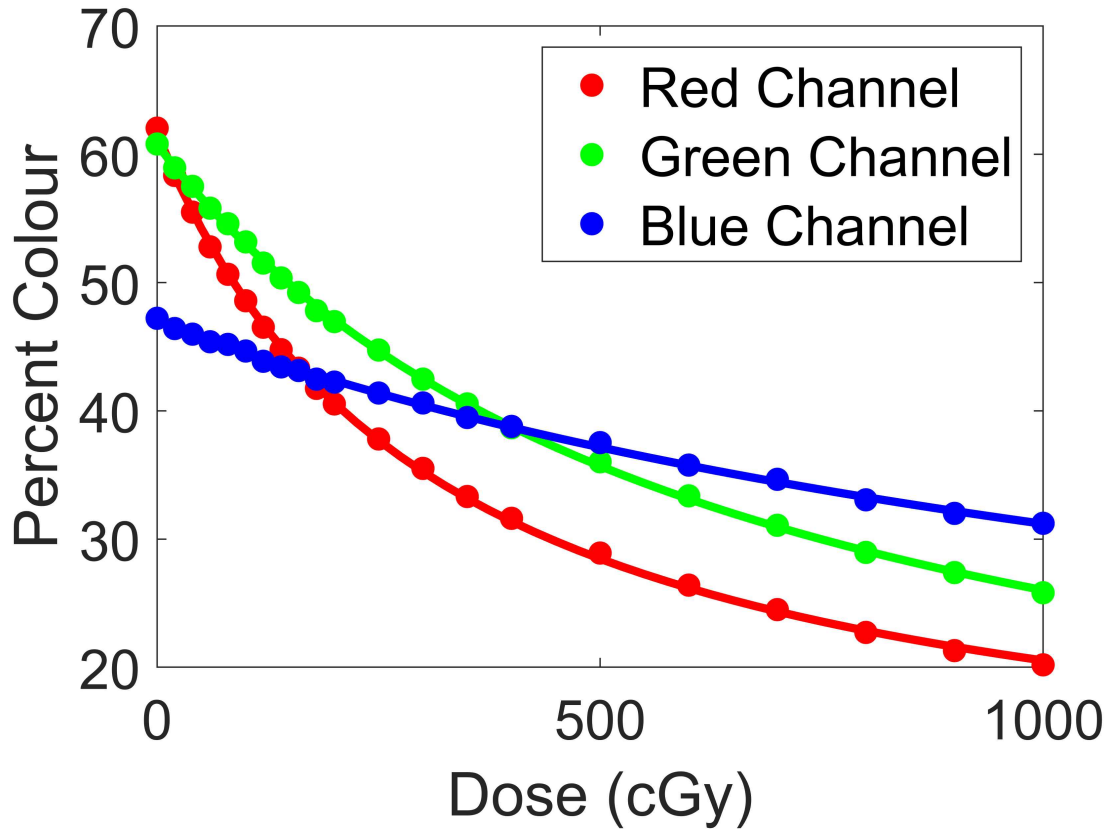


Figure 2.9: Calibration for converting percent colour to dose for each colour channel of red, green, and blue. The multichannel correction used all three colour channels to obtain a more accurate calculation of dose.

$$RS(i, j) = \frac{1}{3} \frac{(\sum_{k=1}^3 a_k(i, j))^2}{\sum_{k=1}^3 a_k^2(i, j)} \quad (2.4)$$

$$a_k(i, j) = \frac{\partial D_k}{\partial I_k}(i, j) \quad (2.5)$$

Further details of the correction method can be found in Mayer et al[73].

The methods detailed in this section were required to complete the developmental work related to SPSDs.

Chapter 3

Manuscript 1: Radiation Induced Photocurrent in the Active Volume of P3HT/PCBM BHJ Photodiodes

3.1 Prologue

This manuscript explains the fabrication and characterization (response ionizing radiation beams) of a P3HT/PCBM BHJ photodiode using the methods discussed in chapter 2. Discussed is a novel technique for the correction of Compton current originating in the electric contacts and leads of the detector. In this chapter the photodiode itself is used as a radiation detector.

The work showed that such a detector could be used as a direct radiation detector by itself, albeit with low sensitivity. However, the sensitivity of the devices was shown to increase with thickness and the sensitivity may be able to be further increased by applying a bias.

This manuscript was published in the journal of Organic Electronics:

- Hupman, Michael A, Irina Valitova, Ian G. Hill, and Alasdair Syme. 2020. “Radiation Induced Photocurrent in the Active Volume of P3HT/PCBM BHJ Photodiodes.” *Organic Electronics* 85:105890.

3.2 Abstract

The purpose of this work is to fabricate and characterize the response of a P3HT/PCBM bulk heterojunction organic photodiode to photon beams with respect to dose rate, total dose, and energy. A bulk heterojunction (BHJ) organic

photodiode was fabricated by spin coating a blend of P3HT and PCBM onto an ITO-coated glass substrate and then depositing aluminum top contacts. Control devices were made by spin coating polystyrene instead of the P3HT/PCBM layer. The devices were irradiated with a 6 MV photon beam with dose rates of 100-600 cGy/min. Energy dependence was measured for energies of 100, 180, and 300 kVp and 6 and 10 MV. Photocurrent in the BHJ was calculated by subtracting the average current measured using the four PS devices from that measured with each of the four BHJ diodes to correct for current collected by the electrodes and the wires/connectors. The sensitivities of the four BHJ devices were within the range of 3.7-4.3 pC/cGy. The range of values is mostly due to inter-device variation and not due to variation between readings on the ITO and Al electrodes of a single device. The diodes exhibit an energy dependence with more than 4 times the response at 100 kVp than at 6 MV. The direction and magnitudes of the measured currents after correction for the electrode/lead currents were consistent with photocurrent. The photocurrents increased linearly with dose rate indicating they could be suitable in radiation sensing applications.

3.3 Introduction

Organic electronic (OE) devices such as organic thin film transistors and organic photovoltaic cells have been researched for decades [74, 75, 76]. While their silicon-based analogs have been used as radiation detectors for decades, it is only relatively recently that interest has grown in the use of OE devices in ionizing radiation sensing applications. These devices are an attractive option for radiation detectors for numerous reasons: they can be fabricated on flexible substrates; they can be formed in 2-dimensional arrays, they can take the functional form of many device types, and have potential for tissue equivalence [77, 78, 79]. We have previously reported on the response of organic field effect transistors to ionizing radiation

and in this work, we focus on the development of organic diodes [80].

To be a good radiation detector, a diode should have low dark current, electronic stability, and show a high induced current when exposed to radiation. Some previous work has shown that organic diodes have a measurable response to x-rays [81, 82, 83]. Kingsley et al (2010) measured the stability of an organic diode made of P3HT and PCBM semiconductors coupled to an inorganic scintillator and exposed to 15 MV photons [84]. They found a reduction of sensitivity of about 5% after 500 Gy. Others have shown it is possible to use organic diodes as direct x-ray detectors [81, 85, 82, 83]. Mills et al. (2013b) irradiated an organic diode with a 10 μm semiconducting layer of F8T2 to a 6 MV photon beam and measured sensitivities of 3.3 and 5.0 nC/Gy for reverse bias voltages of -50 and -150 V, respectively [82]. Mills et al. (2013a) showed in other work that by adding tantalum nanoparticles, the sensitivity of the diodes to 17.5 keV photons was four times higher than without [85]. Intaniwet et al. (2009) measured the stability of a PTAA semiconductor diode and found that the x-ray photocurrent remained the same after a cumulative exposure of 600 Gy and aging of 6 months [83]. These works demonstrate that organic diodes can be used for direct detection of x-rays and exhibit good reproducibility over a large dose range.

In this work BHJ photodiodes were fabricated and exposed to high-energy photon beams and the charge collected on the two electrodes. Excitons created in the BHJ will result in electrons being collected at one electrode and holes at the other. However, in a high-energy photon beam, electrons may also be collected from other interactions. As the photons interact with the materials they can create electrons via the photoelectric effect or Compton effect. These electrons may be created anywhere in the device or even the material surrounding the device, including the wires, and travel a distance through the material due to their high energy. These

electrons can be collected at the electrodes or in the wires and measured as a current that may be comparable to the photocurrent created in the BHJ layers. Evidence for this has been found by Fraboni et al (2012) when they showed that placing shielding material over the leads caused significant reduction in measured signal [86]. Introducing shielding material into the radiation field causes perturbations to the radiation field that could decrease the accuracy of the dose measurement, so it would be better to find an alternative method to correct for this signal. Current produced in the electrodes and wires of the device constitute a stem current. By varying the field size of the irradiation beam more of the wires will be irradiated which will increase the stem effect. In our devices the stem contribution will be corrected by subtracting the current measured with a PS layer between the electrodes instead of the P3HT/PCBM layer. An ion chamber will be used as a ground truth for comparison because it does not exhibit a significant stem effect.

In this work, we measured the response of a P3HT/PCBM BHJ diode in photon beams. The response of the diode was measured as a function of dose, dose rate, and energy of the beams. Furthermore, we set out to extract the photocurrent from the total current measured by subtracting the contribution of signal that does not originate in the BHJ. We believe this is the first time an approach to differentiate between photocurrent and Compton current in organic photodiodes irradiated with ionizing radiation has been shown.

3.4 Methods

3.4.1 Fabrication of Diodes

Fabrication of the organic P3HT (Brilliant Matters, Quebec City, Canada)/PCBM (Solenne BV, Groningen, Netherlands) bulk-heterojunction diodes followed established methods from the photovoltaic literature except that the spin speeds for the

semiconductors were reduced to create thicker films [62, 61, 63]. ITO-covered glass substrates were patterned by etching with hydrochloric acid for 5 minutes. The substrates were cleaned by sonicating in successive solutions of Sparkleen (Thermo Fisher Scientific, Waltham, USA) in DI water, DI water, acetone, and ethanol for 15 minutes each followed by UV-ozone for 20 minutes. PEDOT:PSS (Clevios P VP Al 4083, Heraeus, Hanau, Germany) was spin coated at 5000 rpm for 60 s and placed on a hot plate at 150 °C for 20 minutes. To measure the effects of device thickness, three different recipes for the BHJ were used. A 4 % by weight solution of equal parts P3HT and PCBM in chlorobenzene (Sigma-Aldrich, St. Louis, USA) was spin coated for 60 s at 100 rpm, 60 s at 500 rpm, and then 60 s at 1000 rpm and annealed at 110 °C for 1 hour resulting in a film ~ 420 nm thick. A 2 % by weight solution of P3HT and PCBM was spin coated at the same speeds as above resulting in a film ~ 200 nm thick. Thinner diodes were fabricated with a 2 % by weight solution of equal parts P3HT and PCBM spin coated at 2000 rpm for 60 s resulting in a film about 100 nm thick (typical of an organic photovoltaic cell). The ~ 200 nm thick devices were used for all experiments unless otherwise specified. Next 80 nm of aluminum was deposited through a stencil mask with vacuum thermal evaporation at a rate of ~ 1 Å/s defining an active area of 3.25 mm². The diodes were encapsulated by covering the diode with an epoxy (Ossila, Sheffield, UK) which was cured under UV-light for 20 minutes.

As a control, devices were made with a polystyrene (PS) (Sigma-Aldrich, St. Louis, USA) layer in place of the P3HT/PCBM semiconductors. Solutions of 3, 6, and 10 % by weight solution of PS in toluene were spin coated at 2000 rpm resulting in films ~ 110 , ~ 220 , and ~ 390 nm, respectively. Since polystyrene is an insulator, we expect that no photocurrent will flow through it (i.e. the device should not function as a diode) and any current measured is due to current originating in the electrodes, wires and surroundings from the irradiation.

3.4.2 Irradiation Setup

For all experiments other than energy dependence studies, diodes were irradiated using a Varian Clinac 21EX (Varian Medical Systems, Inc., Palo Alto, USA) medical linear accelerator using 6 MV photons (figure 3.1a,c). Diodes were positioned on top of 15 cm of solid water (Sun Nuclear Corp., Melbourne, USA) with an additional 5 cm of solid water on top for build-up. To prevent the build-up material from damaging the diodes, PMMA was used to hold up the solid water creating a small air gap (~ 1 mm). All machine outputs were measured with a calibrated ionization chamber. During irradiations, a dual channel SMU (Keithley 2614B, Tektronix, Inc., Beaverton, USA) was used to separately measure the current coming from the aluminum and ITO electrodes. The diodes were unbiased for all irradiation measurements.

Medical linear accelerators deliver radiation in pulses of approximately 5 μ s duration with a repetition frequency in the 100 – 300 Hz range. Two types of dose rate can then be defined: The average dose rate varies the number of pulses that are delivered per unit time, but does not vary the dose per pulse; and the instantaneous dose rate (or dose per pulse) which is studied as a variable by maintaining a constant average dose rate and changing the distance between the source and the detector. The inverse square dependence of dose rate thus introduces variation in dose per pulse. Average dose rate dependence of the diodes was measured by delivering 200 cGy with a 10x10 cm² field at dose rates of 100, 200, 300, 400, 500, and 600 cGy/min. Dose per pulse dependence was measured on the Clinac 21EX by varying the source to surface distance (SSD) from 80 to 125 cm with the diode at a depth of 5 cm.

Energy dependence was measured using an Xstrahl 300 orthovoltage x-ray unit (Xstrahl, Surrey, UK) which delivered 100, 180, and 300 kVp photon beams

with solid water under the devices for backscatter (figure 3.1b,d).

Output factors (the variation of machine output as a function of radiation field size) were measured for field sizes between $3 \times 3 \text{ cm}^2$ to $25 \times 25 \text{ cm}^2$ at an SSD of 95 cm and depth of 5 cm. Output factors are normalized at a reference field size ($10 \times 10 \text{ cm}^2$) and ground truth values are determined with an Exradin A12 ion chamber (Standard Imaging, Middleton, WI, USA). Output factor measurements are a good test of the functionality of our PS-based control devices because we know with great certainty the variation of machine output as a function of field size and the only other variable is the amount of “stem” in the field.

In all experiments describe above, the photocurrent was determined by subtracting the current measured with a PS control device from the BHJ device.

3.4.3 Photocurrent Extraction

The geometry of the BHJ diode in this work is shown in figure 3.2. Current was independently measured on each electrode, using two Keithley Source-Measure Units (SMUs) to help distinguish the contribution of the signal due to photocurrent and from current generated elsewhere. A photocurrent would see electrons extracted by the aluminum electrode and holes by the ITO electrode. Electrons collected by the electrodes will result in a positive current as measured by the SMUs. The result would be that the current measured on the aluminum electrode would be a combination of the current generated in the electrode, wires and surroundings, and photocurrent. On the ITO electrode the photocurrent will oppose the current generated in the electrode/wires. To extract the photocurrent from the measured current we replaced the BHJ layer with polystyrene (PS). PS is a dielectric which should not produce any photocurrent, but current will still be present due to the other mechanisms previously stated. By subtracting the PS electrode currents from those measured on the BHJ device, we take the net BHJ currents to represent

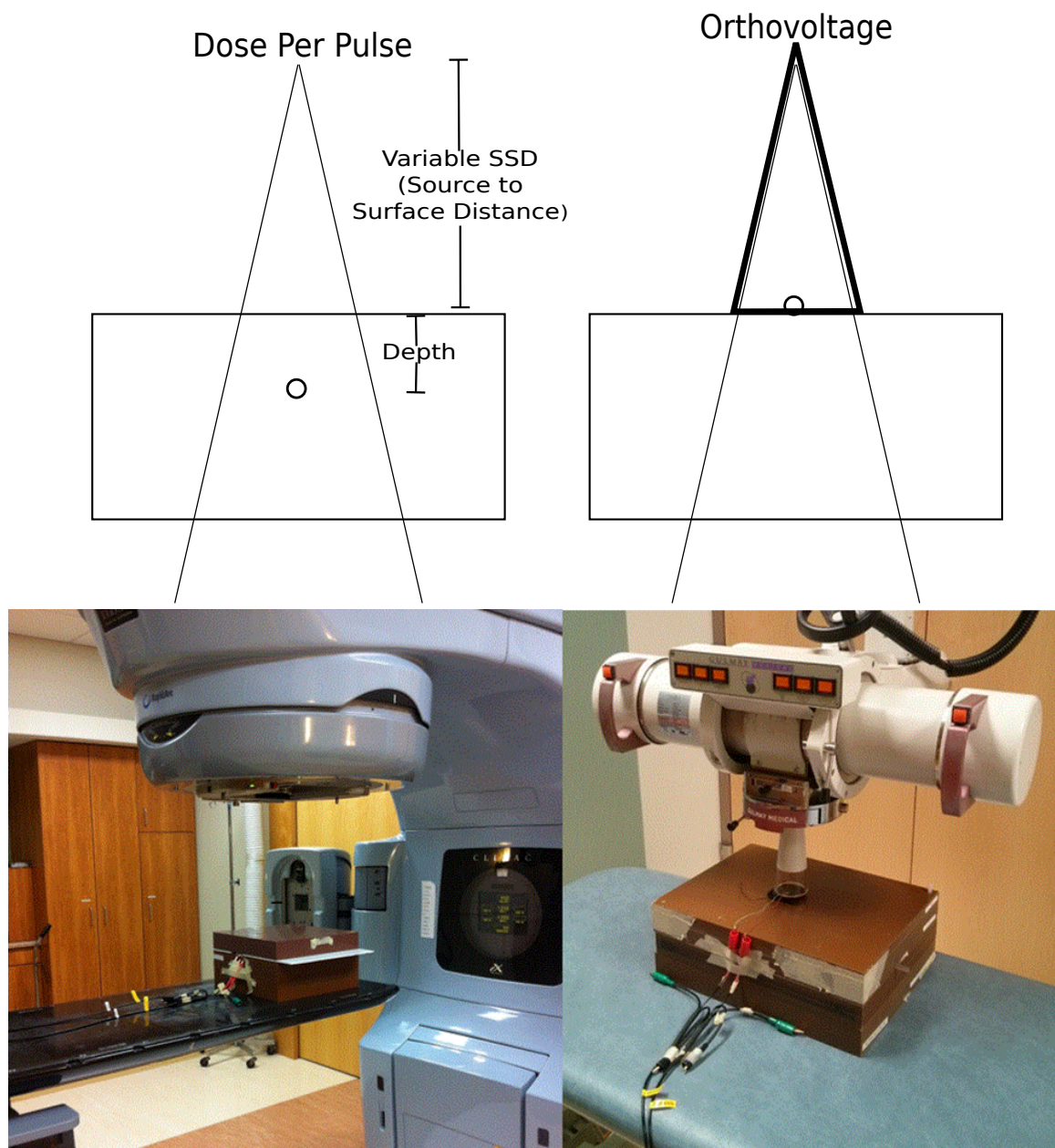
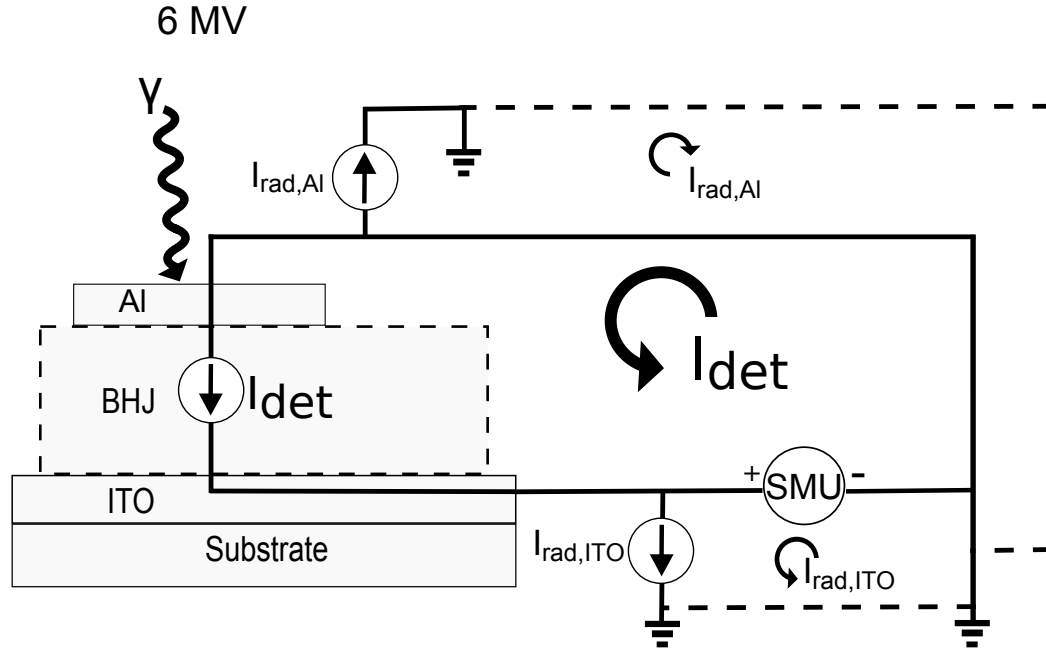


Figure 3.1: The top left shows a schematic of a Linac with the device placed at depth by placing solid water on top of the device. With this setup the source to surface distance (SSD) could be varied to measure the dose per pulse dependence. The top right shows a schematic for Orthovoltage measurements where the device is placed at the surface. On the bottom left is a picture of the diode which is setup to be irradiated with 6 MV or 10 MV photons. 5 cm of solid water is placed on top of the diode for buildup, but has PMMA shims to hold it up to avoid damage to the diode. On the bottom right is a picture of the diode setup for 100, 180, and 300 kVp irradiation with the diode placed on top of a stack of solid water for backscatter.



$$I_{SMU,ITO} = -I_{det} + I_{rad,ITO}$$

Figure 3.2: Schematic diagram of bulk heterojunction (BHJ) diode with electrometers connected. The current was measured coming from each electrode to isolate the contribution of the signal originating in the BHJ. I_{det} is the radiation induced current from the detector. $I_{rad[ITO/Al]}$ is the radiation induced current in the electrodes and leads. When measuring the current from the ITO electrode $I_{rad,ITO}$ contributes to the signal, but $I_{rad,Al}$ does not and vice versa. The signal measured with a PS control device is due to $I_{rad[ITO,Al]}$ allowing a correction.

those generated within the device itself, i.e. the photocurrent. The resulting calculated photocurrent should be negative on the ITO electrode and positive on the aluminum electrode (given the definitions in Figure 3.2), but of equal magnitude.

3.5 Results

Figure 3.3 shows the average current measured across four BHJ diodes (~ 200 nm thick) and four PS control devices (~ 220 nm) on both the ITO and aluminum electrodes using six different dose rates. The BHJ diode had an increase of current

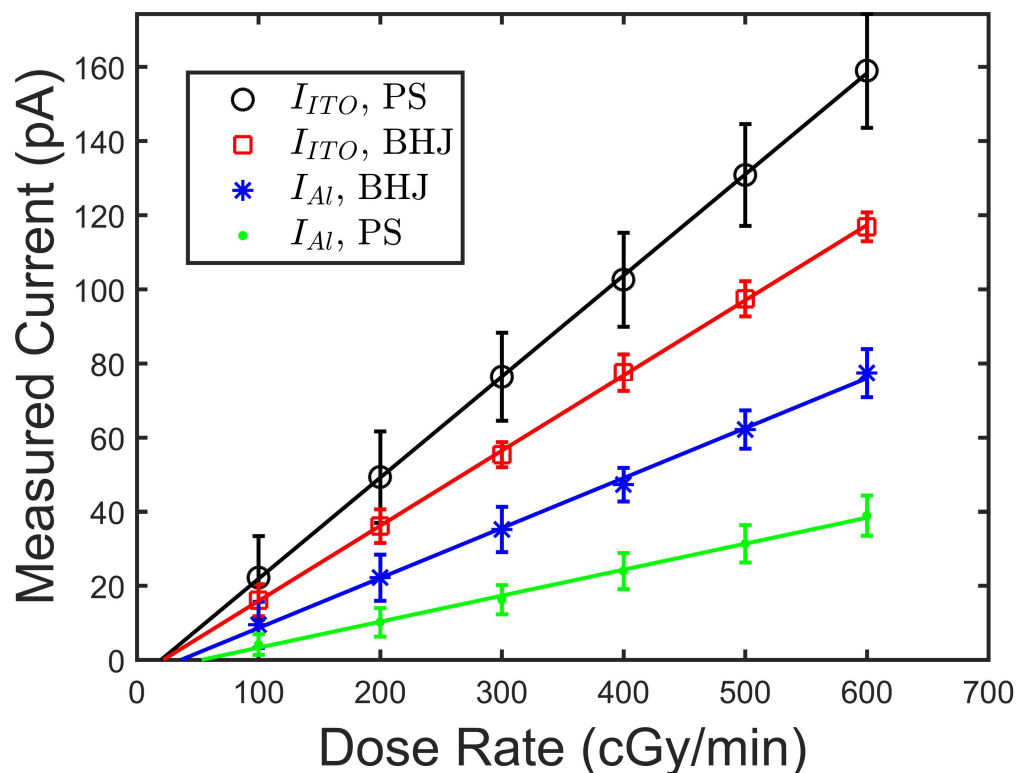


Figure 3.3: The average current collected from the BHJ diodes (~ 200 nm thick) and the PS devices (~ 220 nm thick) was measured at various dose rates and showed a linear increase indicating there was no dependence of average dose rate. The BHJ diode exhibits an increase of current through the aluminum electrode and decrease of current through the ITO electrode in comparison to the PS device.

on the aluminum electrode and a decrease of current on the ITO electrode in comparison to the PS control device. Each individual device had a linear increase of beam on current with dose rate. The error bars are due to the variability between devices and are not representative of noise in the measured data from a single device.

Figure 3.4 shows the net photocurrent collected at each of the electrodes by subtracting the average current flowing through the PS devices from each of the four BHJ diodes. The ITO photocurrent was negative, but its magnitude is plotted to show how the ITO current compared to that at the Al electrode. The range of

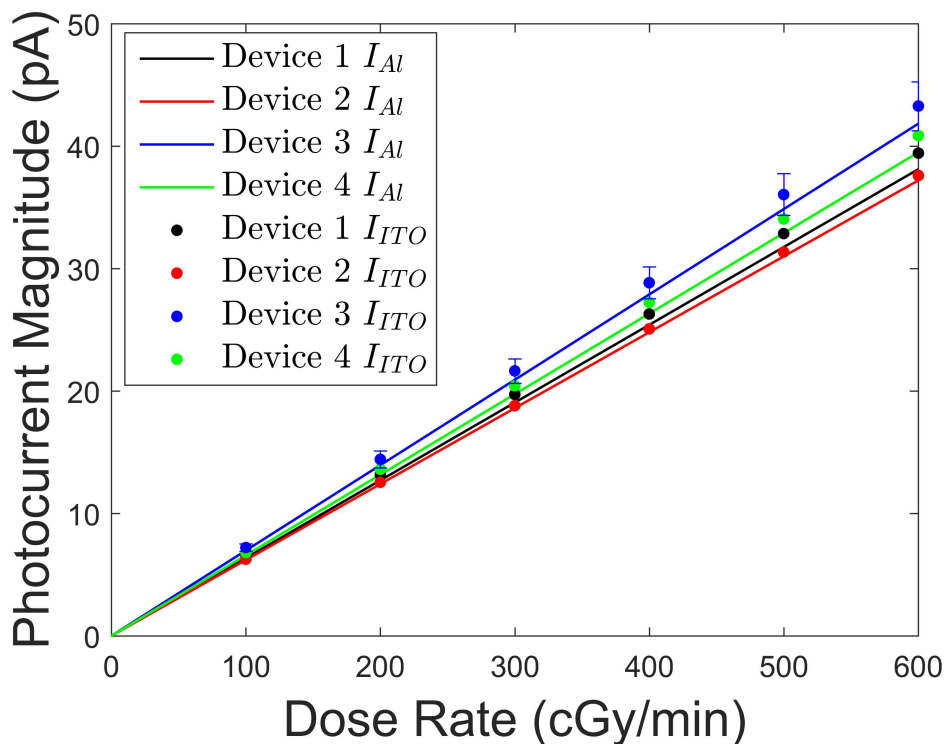


Figure 3.4: The absolute photocurrent flowing through each electrode as a function of dose rate was found by subtracting the average current flowing through the PS devices from each of the four BHJ diodes. The magnitude of the current is shown for comparison between the electrodes, but the ITO current was measured to be negative. The similarity of magnitudes and the direction of current is consistent with our interpretation that we are measuring photocurrent. The photocurrent flowing through each electrode increases linearly with dose rate indicating no dependence on average dose rate. Error bars are shown for device 3 to indicate magnitude, but the other devices had similar values.

sensitivities on the ITO and aluminum electrodes are 3.8-4.3 and 3.7-4.2 pC/cGy, respectively. The direction of the current on each electrode and the ITO/Al magnitudes being comparable is consistent with the net current representing the photocurrent generated in the BHJ.

The total current flowing through the aluminum electrode of a BHJ diode is shown in figure 3.5 for a 100 s irradiation at a dose rate of 600 cGy/min. The current while the beam is on for this particular diode is 87 ± 1 pA. The SNR while the beam was on was approximately 180.

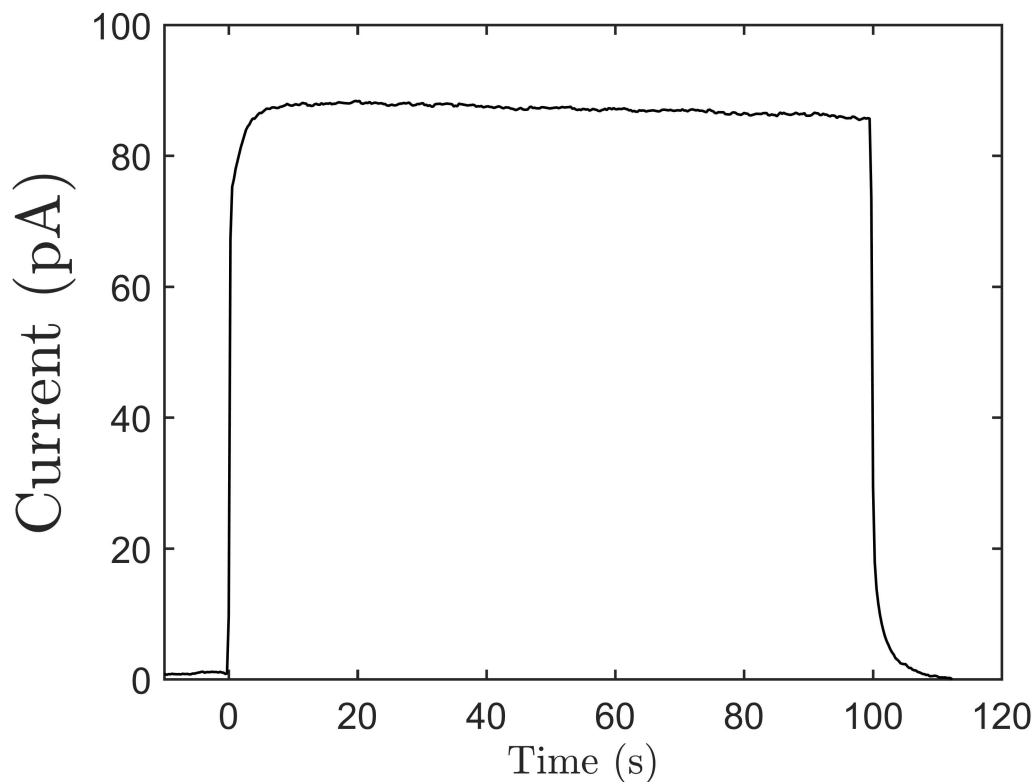


Figure 3.5: The total current flowing through the aluminum electrode for a BHJ diode when irradiated at 600 cGy/min for 100 s.

Figure 3.6 shows both the total (raw current measured with no PS correction) and net (with PS correction) response of the diodes at five different energies (effective energies ~ 0.047 , 0.072 , 0.135 , 1.92 , and 2.97 MeV) [87]. The relative charge collected by the diode normalized at an effective energy of 1.92 MeV is shown. The sensitivity of the diode decreases as the energy increases. There is an increase of response at 100 kVp of 4.7 ± 0.4 and 3.5 ± 0.4 times that of 6 MV for the uncorrected and corrected measurements, respectively.

Figure 3.7 shows the range of sensitivities found for three thicknesses of BHJ diodes. The sensitivity was calculated with the photocurrent determined by subtracting the current from the PS devices. The sensitivities of the diodes increase with thickness. The measured ranges of sensitivities were 1.8 - 2.8 , 3.7 - 4.3 , and 6 - 7.5

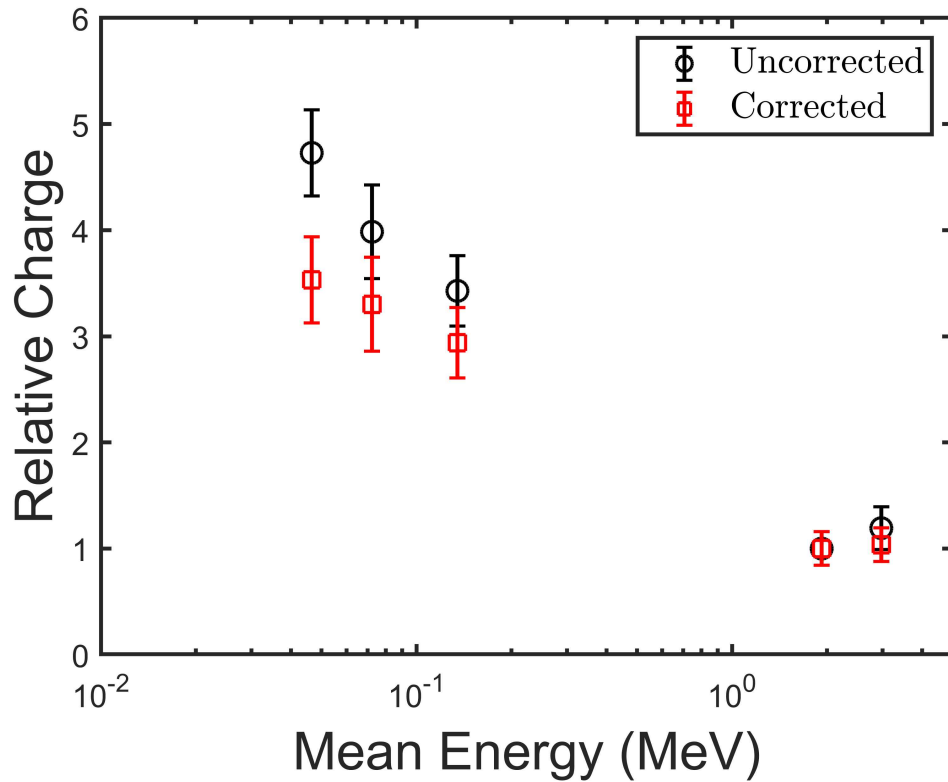


Figure 3.6: The charge collected by the diode irradiated with 1 Gy and normalized at an energy of 6 MV. The corrected data has the charge collected by the PS device subtracted from the BHJ as before. The effective energies are 0.047, 0.072, 0.135, 1.92, and 2.97 MeV.

pC/cGy for thicknesses of 100, 200, and 420 nm, respectively.

Figure 3.8 shows both the total (raw current measured with no PS correction) and net (with PS correction) response of the diodes when varying the dose per pulse. Before correction there is a decrease in response with dose per pulse and a deviation from the normalized dose per pulse of over 10 %. After correction the dependence is reduced with a maximum deviation of approximately 2 % over the SSDs of 80-125 cm when normalized at 95 cm.

Figure 3.9 shows the output factor before and after correcting the response. The output factor is the response of the detector as it varies with field size normalized to the response of the detector with a 10x10 cm² field size. Ion chamber

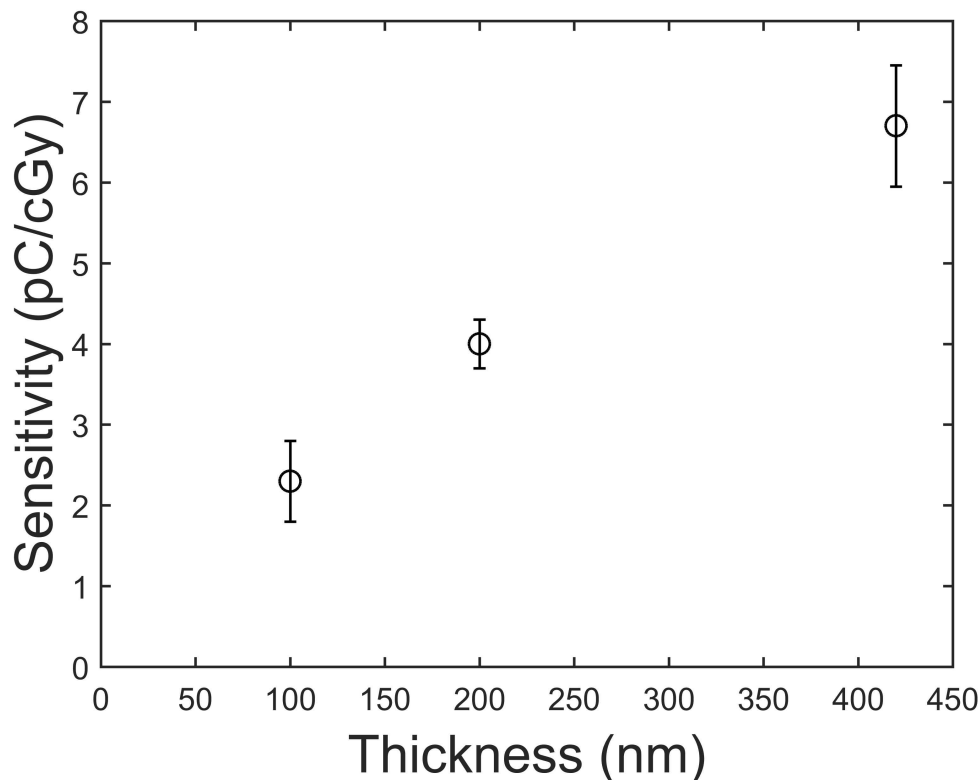


Figure 3.7: The range of sensitivities of four BHJ diodes are plotted for three thicknesses. The sensitivity was calculated after the current was corrected by subtracting the current measured with PS devices.

measurements are used as a ground truth for comparison because they exhibit no stem effect. Before correction there is a large field size dependence likely due to the wires contacting the devices. However, after correction all points are within 2 % from field sizes of $3 \times 3 \text{ cm}^2$ to $20 \times 20 \text{ cm}^2$.

3.6 Discussion

The current measured using the BHJ was positive on each of the two electrodes as shown in figure 3.3. If the response of the device were analogous to that of a photodiode, the currents at the two electrodes would be in the opposite direction, but of equal magnitude. The currents measured on PS device electrodes were subtracted from those measured on BHJ devices. After performing this correction,

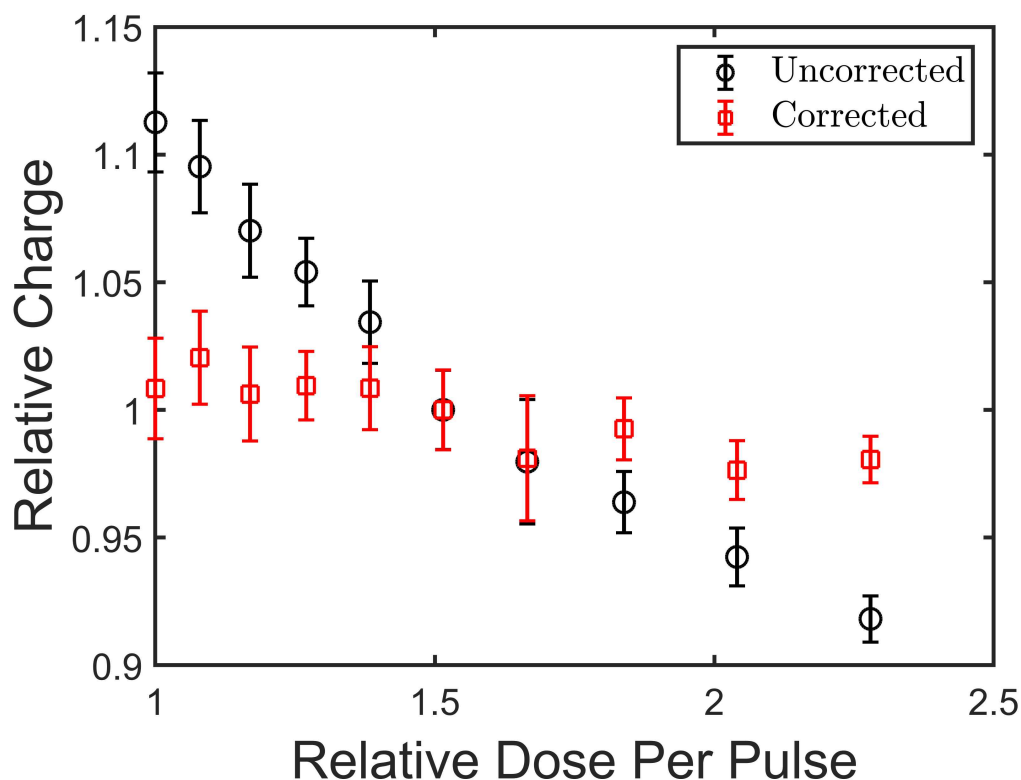


Figure 3.8: The dose per pulse was varied by varying the SSD between 80-125 cm and the charge normalized to an SSD of 95 cm. Before the correction the response of the BHJ diode decreases with increasing dose per pulse. After correction the dependence was reduced.

the net current found on each BHJ electrode is of comparable magnitude and the direction of the current is consistent with our model and what would be expected from a photocurrent (figure 3.4). We believe that we are the first to try to quantify the magnitude of such a correction. These data show that when measuring the radiation-induced current in an organic diode one should be careful before assuming the entire signal is photocurrent.

High energy (megavoltage) photons typically interact in water-like materials via the photoelectric effect and Compton scatter. The high energy electrons that are set in motion as a result of these interactions move through the medium producing additional excitations and ionizations. The net result is a shower of electrons

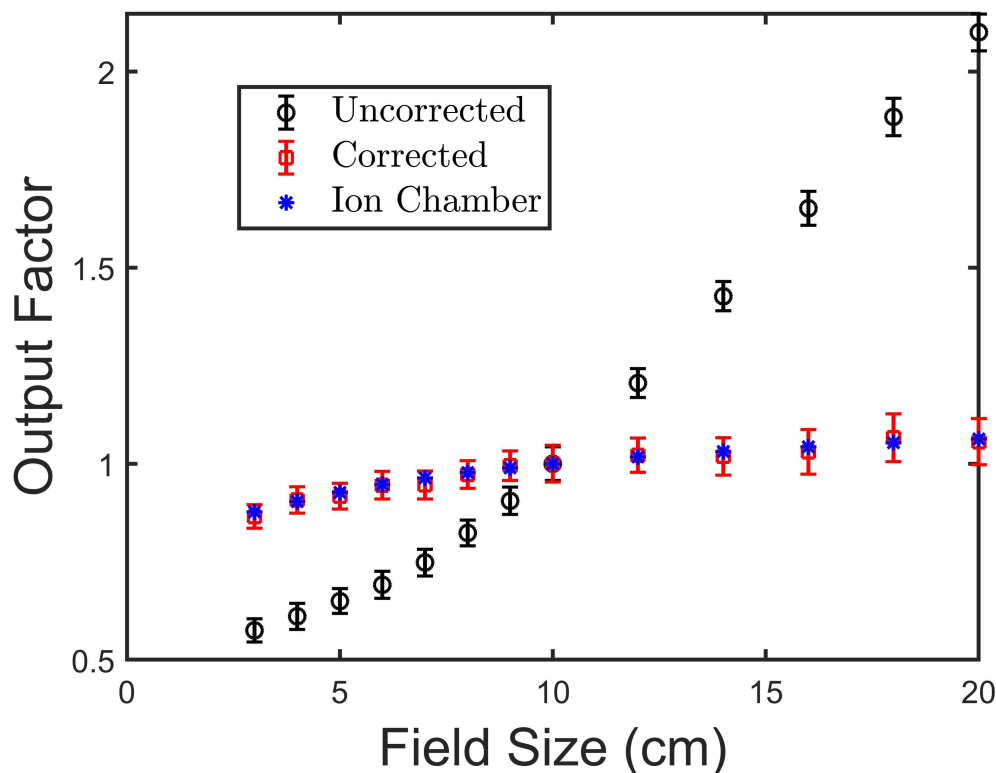


Figure 3.9: The output factor was measured for a 6 MV photon beam and compared to ion chamber measurements. Before the correction was applied there was a large difference between device and the ion chamber which was greatly reduced with the correction.

with a wide range of energies. Low energy electrons may create excitons which may have energy close to that of excitons created with the exposure to light. If the excitons are “hot excitons” then we expect they will thermalize rapidly like in solar cells. As a result, we believe we are primarily measuring excitons. Furthermore, planar P3HT films of thickness comparable to the ones used in this study were fabricated and the measured current was indistinguishable from the PS measured current within error (data not shown). We interpret these results to mean that diffusion and dissociation at an interface are important processes for this radiation sensing application.

The diodes exhibit an energy dependence with the response at 100 kVp being 4.7 ± 0.4 and 3.5 ± 0.4 times that at 6 MV for the uncorrected and corrected measurements, respectively. This is larger than might be expected based on photon-interaction cross section ratios. The use of PS as a surrogate for the organic semiconductors may not have the same effect at MV versus kV energies and the patterns of energy deposition in the semiconductors at these different energy levels may contribute to the observed differences, though future work will be required to validate either of these hypotheses. Efforts to reduce the energy dependence of the devices will include the use of organic conductors for contacts as well as material composition optimization to reduce photon interaction probabilities at low photon energies.

The photocurrents measured in this work are approximately two orders of magnitude lower than typical ionization chamber currents for similar measurements. Figure 3.7 shows an increase in sensitivity with thickness and does not appear to have saturated at a thickness of 420 nm, suggesting that further gains in signal may be realized with thicker devices. Furthermore, sensitivities in the range observed here are comparable to a commercially-available parallel plate ionization chamber (Advanced Markus Chamber, PTW-Freiburg, Freiburg, Germany: 6.7 pC/cGy). Clinically-used detectors minimize the footprint of wires and contact points to reduce the Compton current induced during irradiation. For our purposes, this optimization is not practical for laboratory based exploration. However, even after minimizing this effect it can be problematic in some detectors depending on the application (small volume ion chambers can still have Compton current induced during irradiation (stem effects)). Minimizing the footprint of the wires and contacts of the devices presented in this work should result in a device which only needs one SMU to measure the signal with no PS correction necessary. Further work will explore the impact of BHJ composition and measurement parameters on device sensitivity

(i.e. applying a reverse bias, changing semiconductor material, etc.).

The dose per pulse was varied by changing the SSD and using a $10 \times 10 \text{ cm}^2$ field size (defined 100 cm from the source) (figure 3.8). Changing the dose per pulse (by increasing or decreasing the distance to the detector) results in a magnification or minification of the field size at the detector, which causes more or less of the wire which is carrying the signal to be irradiated. After correction by subtracting the PS measured current there is a large improvement in the dose per pulse dependence. Similar behaviour was observed when measuring output factors. This indicates that non-photocurrent signal cannot be neglected since it can have a significant impact on the accuracy of dose measurements.

In this work a BHJ photodiode was irradiated and the photocurrent was corrected by subtracting the current measured using a PS device irradiated using the same setup. This requires two measurements, but a device could be made where the BHJ and PS devices are fabricated on the same substrate next to one another and irradiated together (figure 3.10). This would allow the measure of photocurrent in a single measurement. The downside of this technique is a reduction of spatial resolution and may result in increased uncertainties for measurements in high dose gradient regions. Such a dual device correction method is not without precedent, however. A dual-MOSFET design in which two identical MOSFETs are fabricated on two similar silicon chips and operated at two different biases has been used for years [88].

3.7 Conclusion

We studied the response of a BHJ device to photon beams of various qualities, various dose rates, and accumulated dose. We corrected the measured signal by subtracting the current measured with a device where the BHJ layer was substituted with PS. Doing this we were able to differentiate between the photocurrent

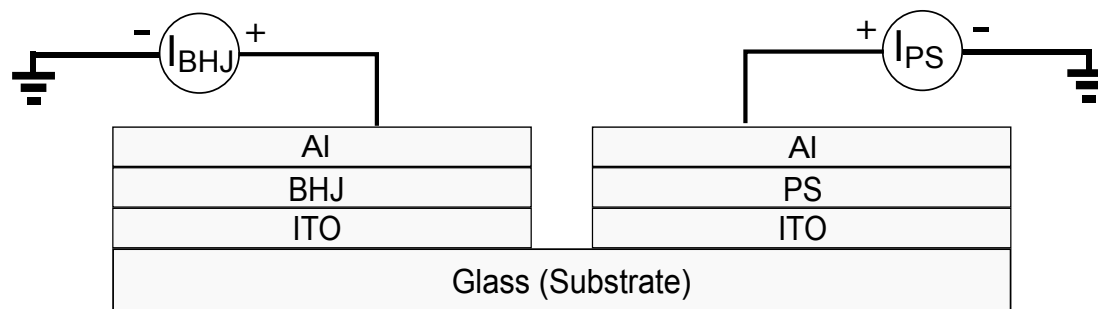


Figure 3.10: Schematic of BHJ and PS device fabricated side by side to allow the measurement of photocurrent with a single measurement. However, this would reduce the spatial resolution and could result in increased uncertainties in high dose gradient regions.

and the extraneous signal. After correction the current measured on each of the electrodes were of equal magnitude and the direction was consistent with photocurrent created in the BHJ layer. These data are consistent with our proposed model of device signal and emphasizes the need to be cautious when using organic diodes as radiation detectors and attributing the signal to the BHJ layer. Furthermore, after correction the output factors matched the ion chamber measurements within 2 % indicating that the stem effect had been effectively corrected. The sensitivity of the BHJ after correction was 4.1 pC/cGy. The BHJ had a decrease in response with energy (4 times sensitivity at 100 kVp compared to 6 MV), and future work will aim to further our understanding of this behaviour.

Chapter 4

Manuscript 2: Method for the Differentiation of Radiation-Induced Photocurrent from Total Measured Current in P3HT/PCBM BHJ Photodiodes

4.1 Prologue

This manuscript details and validates the method used to correct the Compton current (current originating in the electrodes, wires, etc.) in manuscript 1. The Compton current had a strong field size dependence because as the field size increases more of the electrical components are directly in the irradiation beam. The footprint of the electrodes were not optimized as this was a preliminary study. A commercial product could greatly reduce the size of electrodes (and therefore Compton current). However, due to the low signal (radiation induced current) of this device some correction may still be necessary. The method resulted in excellent agreement of output factor measurements with a commercial ion chamber.

This manuscript was published in the MethodsX journal:

- Hupman, Michael A, Irina Valitova, Ian G. Hill, and Alasdair Syme. October 2020. “*Method for the Differentiation of Radiation-Induced Photocurrent from Total Measured Current in P3HT/PCBM BHJ Photodiodes.*” *MethodsX* 7:101125.

4.2 Abstract

Thin film radiation-detecting diodes fabricated in the laboratory, such as an organic bulk heterojunction, often contain conductive leads, indium tin oxide traces and metallic interconnects which are exposed to the high-energy photon beam during operation. These components generate extraneous radiation-induced currents, that, if not accounted for, will erroneously be attributed to the detector. In commercial devices, these contributions are mitigated by minimizing the size of these components, an approach that is often not feasible in a research lab. Here we demonstrate a method to measure these extraneous signals, and by subtraction, correct the gross signal to accurately reflect the signal generated in the active volume of the diode itself.

- The method can effectively correct the extraneous signal.
- The method showed promise over a range of photon beam energies, dose rates, and field sizes.

4.3 Methods Details

4.3.1 Introduction

The ability to accurately measure absorbed dose (energy deposited per unit mass) is a critical prerequisite for the safe and effective use of ionizing radiation to treat cancer. Numerous types of devices can be calibrated for this purpose (e.g. ionization chamber, thermoluminescent dosimeter, silicon diode, film, etc.); in this work, we describe measurements in radiation fields using a P3HT/PCBM bulk heterojunction (BHJ) photodiode. Organic semiconductor-based dosimeters have gained interest because of their low atomic number, which is comparable to that of human tissue, which suggests that these devices could require fewer or smaller correction factors to translate a measurement into absorbed dose in comparison to their silicon

counterparts.

In an ideal radiation detector, the entirety of the measured signal is generated in the “active volume” of the detector. In the case of thin film diodes, such as organic BHJ photodiodes, this would be in the BHJ itself (i.e. the semiconductors), between the two electrodes. In the case of electrical devices, however, an additional current can be generated due to interactions in the electrodes, connectors, and wires. This “Compton current” constitutes an extraneous signal that contaminates the true signal of interest and can detract from the accuracy of a dose measurement.

4.3.2 Device Fabrication

Fabrication of the organic P3HT (Molecular weight 50-80 kg/mol, Brilliant Matters, Quebec City, Canada)/PCBM (Solenne BV, Groningen, Netherlands) BHJ diodes followed established methods from the photovoltaic literature [62, 61, 63, 66]. ITO-coated glass substrates were patterned by etching with hydrochloric acid for approximately 5 minutes. The etched slides were cleaned by sonicating for 15 minutes in successive solutions of deionized water with Sparkleen (Thermo Fisher Scientific, Waltham, USA), deionized water, acetone, and ethanol followed by UV-ozone for 20 minutes. PEDOT:PSS (Clevios P VP Al 4083, Heraeus, Hanau, Germany) was spin coated for 60 s at 5000 rpm and placed on a hot plate at 150 °C for 20 minutes in air. Equal parts P3HT and PCBM in chlorobenzene (Sigma-Aldrich, St. Louis, USA) were spin coated in inert atmosphere (N_2) inside a glove box with different recipes to create devices of three different thicknesses. A 2 % by weight solution was spin coated at 2000 rpm for 60 s resulting in a film \sim 100 nm. A 2 % by weight solution was spin coated for 60 s at 100 rpm, 60 s 500 rpm, and then 60 s at 1000 rpm resulting in a film \sim 200 nm. A 4 % by weight solution was spin coated

with the same speeds as the ~ 200 nm film resulting in a ~ 420 nm film. Film thickness was measured with a Dektak 8 stylus profilometer (Bruker Corporation, Billerica, USA). The films were annealed at 110 °C for 1 hour in inert atmosphere (N_2). Aluminum was deposited with vacuum thermal evaporation at a rate of ~ 1 Å/s to a thickness of ~ 80 nm defining an active area of 3.25 mm². The diodes were encapsulated with an epoxy (Ossila, Sheffield, UK), which was cured under UV-light for 20 minutes.

As a control, devices were made with a polystyrene (PS) (Molecular weight ~ 280 kg/mol, Sigma-Aldrich, St. Louis, USA) layer in place of the P3HT/PCBM semiconductors with the rest of the device following the fabrication detailed above. Solutions of 3, 6, and 10 % by weight solution of PS in toluene were spin coated at 2000 rpm resulting in films ~ 110 nm, ~ 220 nm, and ~ 390 nm, respectively.

4.3.3 Extraneous Signal

The BHJ photodiode was exposed to high energy (megavoltage) photons from a Varian TrueBeam medical linear accelerator (Varian Medical Systems, Palo Alto, USA). A schematic of the BHJ photodiode is shown in figure 4.1a. Initial measurements used one SMU with the positive output connected to the ITO electrode, and negative connected to the aluminum electrode. Our hypothesis was that the high energy irradiation would create excitons in the BHJ layer similarly to the way in which excitons are produced when the BHJ is exposed to visible light. If that were true, holes would migrate to the ITO electrode, resulting in a measurement of a negative current. However, what we measured was a positive current. To investigate the problem further we used a two-SMU setup which measured the current coming from each electrode independently, and simultaneously. If our initial hypothesis was correct, electrons would migrate to the aluminum electrode and a positive current would be measured of equal magnitude to the negative current on

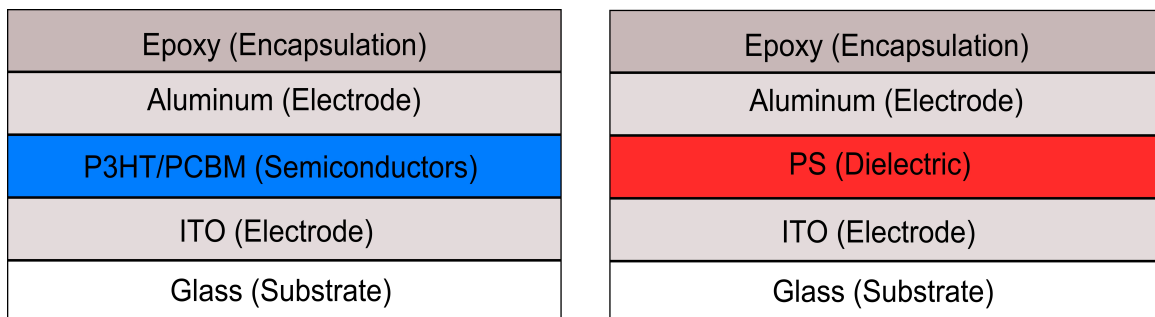


Figure 4.1: Schematic diagrams of the BHJ photodiodes (left) and PS control devices (right). The devices are identical except the organic semiconductors are replaced by PS in the control devices. Care was taken to create recipes that produced PS layer thicknesses that matched BHJ semiconductor thicknesses as much as possible.

the ITO electrode. However, the currents measured on the two electrodes were both positive, and of different magnitudes. We hypothesized that an undesirable current induced in the electrodes, wires, etc. due to the shower of electrons induced by the radiation beam. To correct for this Compton current we needed a device which would measure the Compton current without any radiation-induced photocurrent in the BHJ. For this purpose we fabricated a device with polystyrene (PS) in place of the BHJ as shown in figure 4.1b. A PS device should have negligible photocurrent because without a donor/acceptor interface there should be no dissociation and, even if free charges were generated, the mobility of these charges would be very low in PS, resulting in a very low extraction efficiency. An important detail of the measurement setup for this correction technique is to ensure an identical geometry of the electrodes, wires, etc. with respect to the radiation field for both device types to ensure the Compton current will be the same in both measurements.

4.3.4 Correction Method

Initially, to measure the current coming from the device, triaxial cables were used which had alligator clips at the end to connect to contact pads on the edge of the substrate. To decrease the Compton current, the bulky alligator clips needed to

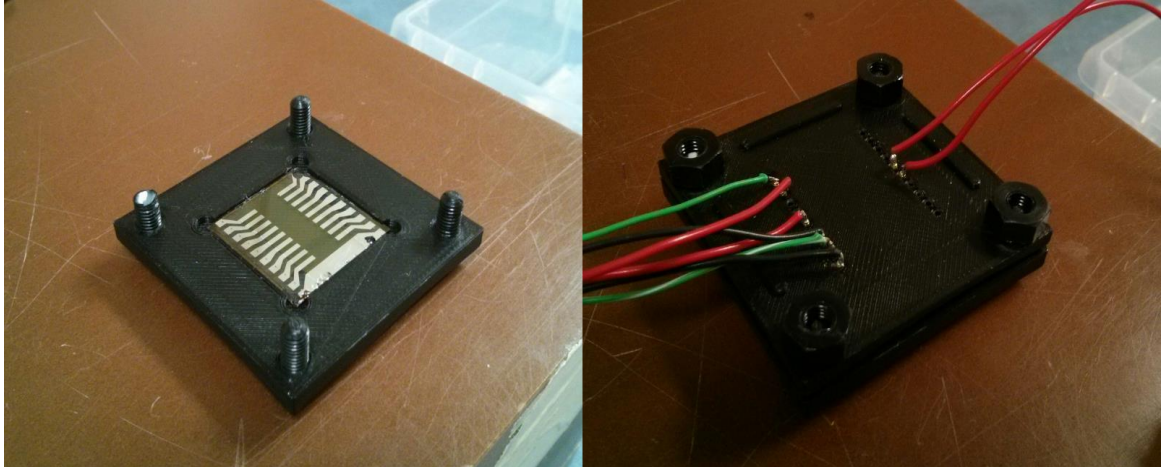


Figure 4.2: Picture of the device holder with and without the top to allow easy electrical contact. The holder shields light from reaching the photodiode and allows easy and consistent contact on the devices.

be placed outside of the irradiation field. To accomplish this a 3-D printed holder was used with pogo pins to contact the photodiode (figure 4.2). Next, wires were soldered to the ends of the pogo pins and brought outside of the beam. This reduced the size of the contacts in the beam. Furthermore, the 3-D printed holder allowed for easy device alignment within the beam and the path of the wires could be more easily reproduced when changing from a BHJ diode to a PS device. An added benefit of the 3-D printed holder is that it makes it easy to shield the BHJ photodiode from light.

A BHJ photodiode was irradiated and the current measured on the ITO electrode using an SMU (Keithley 2614B, Tektronix Inc., Beaverton, USA) as depicted in figure 4.3. Two distinct currents are labelled that contribute to the measured current. First, there is the current induced inside the BHJ semiconductors I_{det} which is analogous to photocurrent generated when a light is incident on a photodiode. Second, there is a Compton current $I_{rad,ITO}$ which is generated in the electrodes, contacts, and wires associated with the ITO electrode due to the incident radiation beam and the associated secondary electrons impinging upon them. A

similar current, $I_{rad,Al}$, is generated in the top-contact electrode and associated conductors. When a megavoltage photon beam (of the type encountered in a radiation therapy setting) interacts in a water-like material it creates electrons primarily via Compton scatter and some photoelectric effect. These electrons have enough energy to produce additional excitations and ionizations. The net result is a shower of electrons spanning a large range of energies. Electrons interacting in the electric contacts and wires can produce a current that contributes to the measured current represented by $I_{rad,[ITO/Al]}$ in the figure. The Compton current produced in the aluminum contact and wires $I_{rad,Al}$ does not contribute to the current measured on the ITO electrode. However, if the SMU were connected to measure the current coming from the aluminum electrode $I_{rad,Al}$ will contribute to the current and $I_{rad,ITO}$ will not. Furthermore, the magnitude of I_{det} will be the same, but it will be the opposite direction. In equation form these measurements can be represented by:

$$I_{SMU,ITO,BHJ} = -I_{det} + I_{rad,ITO} \quad (4.1)$$

$$I_{SMU,Al,BHJ} = I_{det} + I_{rad,Al} \quad (4.2)$$

Where $I_{SMU,[ITO/Al],BHJ}$ is the current measured by the SMU when connected to the BHJ photodiode to the ITO/Al electrode. Since I_{det} is negative when measuring the ITO current, the Compton current direction will oppose it (given the current directions defined in figure 4.3). The magnitude of $I_{rad,[ITO/Al]}$ will depend on the area of the electrodes and the amount of connector and wires in the irradiation beam (as well as beam parameters such as energy, dose rate, etc.).

To correct for the $I_{rad,[ITO/Al]}$ current and obtain the detector current I_{det} we fabricated devices with polystyrene (PS) instead of the BHJ. We expect that excitons will be generated in the PS layer just like the BHJ. However, given the insulating nature of PS, and the absence of a donor/acceptor interface, we do not expect

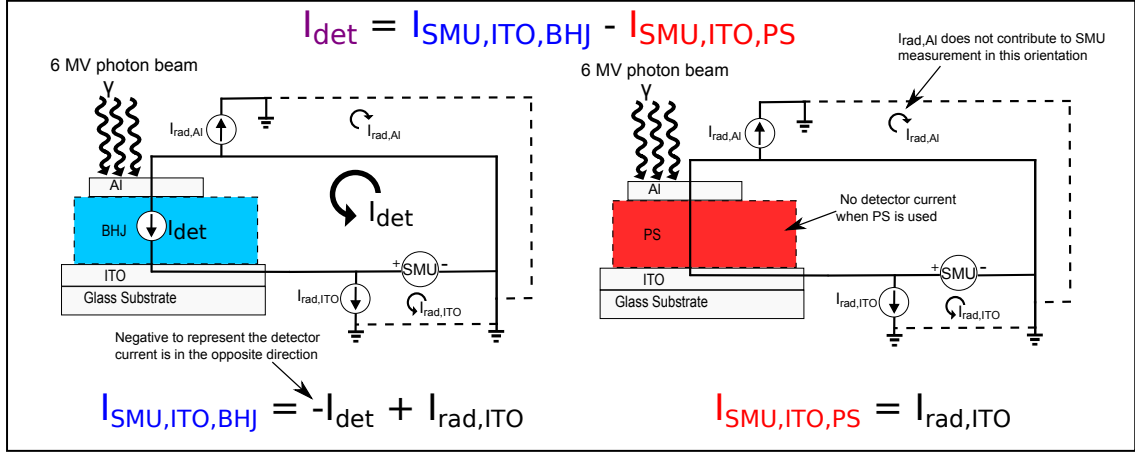


Figure 4.3: Schematic showing the two circuits used for the correction method. On the left the bulk heterojunction (BHJ) diode is placed in the radiation beam and the current is measured with an SMU connected to the ITO electrode. This measurement has current induced in the detector (I_{det}) and Compton current induced in the electrodes and wires ($I_{rad,ITO}$). On the right a polystyrene device has been placed in the irradiation beam in place of the BHJ diode and the current measured coming from the ITO electrode. The PS device will have no detector current (I_{det}), but will measure a Compton current ($I_{rad,ITO}$). To calculate the detector current (I_{det}) the current measured with the PS setup is subtracted from the BHJ diode setup.

any significant detector current. The measured current will be dominated by the extraneous contributions. Furthermore, if the irradiation setup is the same as when irradiating the BHJ (same beam energy, dose rate, etc.) then the $I_{rad,[ITO/Al]}$ current should be the same as measured for the BHJ. By measuring this current and subtracting it from the current measured with the BHJ measured current we can calculate the I_{det} current with the ITO electrode using:

$$I_{SMU,ITO,BHJ} - I_{SMU,ITO,PS} = (-I_{det} + I_{rad,ITO}) - (I_{rad,ITO}) \quad (4.3)$$

$$I_{SMU,ITO,BHJ} - I_{SMU,ITO,PS} = -I_{det} \quad (4.4)$$

Or on the aluminum electrode:

$$I_{SMU,Al,BHJ} - I_{SMU,Al,PS} = (I_{det} + I_{rad,Al}) - (I_{rad,Al}) \quad (4.5)$$

$$I_{SMU,Al,BHJ} - I_{SMU,Al,PS} = I_{det} \quad (4.6)$$

To do this correction only one SMU is needed. The current can be measured from the same electrode on the BHJ device and the PS device and the current subtracted. An additional check to increase confidence in the correction method can be performed by simultaneously measuring the current with both electrodes and comparing the calculated detector current for both direction and magnitude.

4.3.5 Validation of Method and Quantification of Compton Current

Figure 4.4 shows the current measured as a function of field size for the BHJ photodiode, PS device, and the corrected current (subtract the PS measured current from the BHJ measured current). For comparison measurements were done with no device attached to the leads and the alligator clips placed in the beam. Under these conditions 200 ± 50 pA was measured for a 10×10 cm² field which is more than the induced current in a BHJ diode. The figure shows that the Compton current (PS device) contributes a significant portion of the total signal (BHJ diode). Furthermore, the proportion of the total signal contributed due to Compton current increases with field size, as the leads receive a larger dose. This is shown in figure 4.5 more explicitly, where the percent of the total signal due to Compton current is given as a function of field size. Compton current makes up 11 ± 3 % of the total signal for a field size of 3×3 cm², but contributes over 60 % of the signal for a 20×20 cm² field. Compton current increases with field size because more length of wire is exposed to the beam. The corrected current increases with field size as well because more scatter is present which increases the dose at the middle of the field.

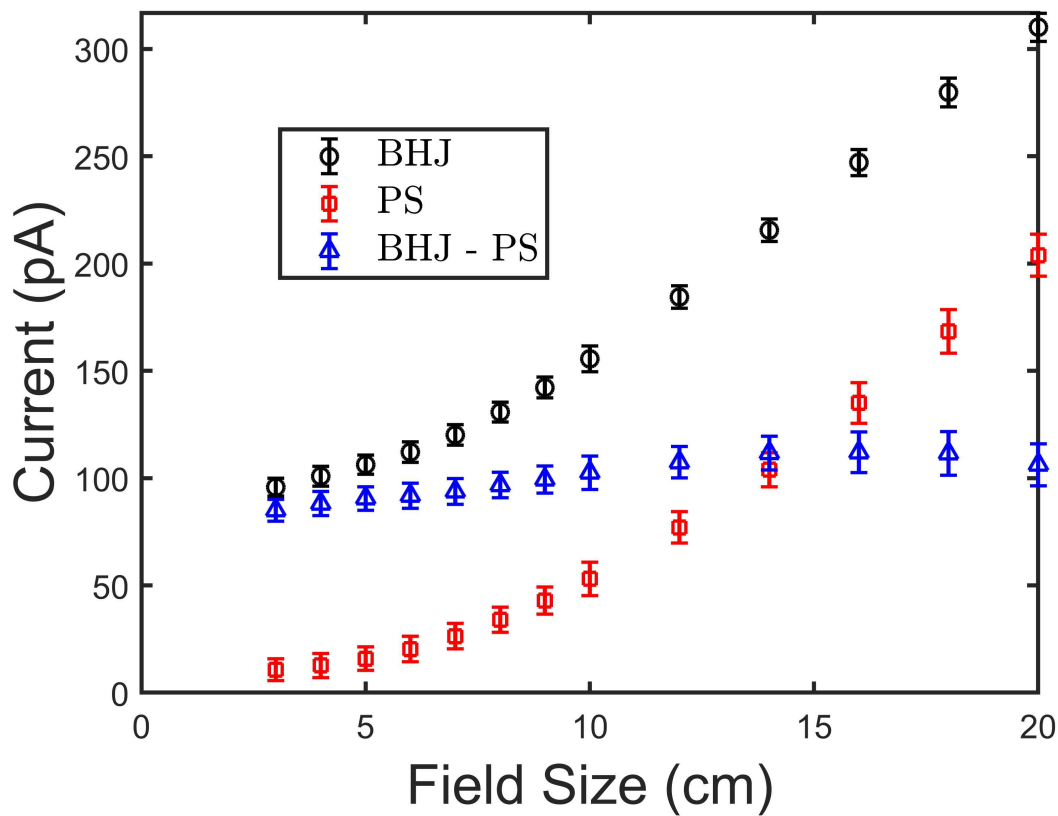


Figure 4.4: The current is plotted as a function of the field size for the bulk heterojunction (BHJ) photodiode, polystyrene (PS) device, and the corrected current (PS current subtracted from BHJ). For both the BHJ and PS the current increases with field size due to increasing the amount of wires irradiated. Data in this figure were used to produce figure 9 in Hupman et al (2020) [66].

This effect is well-known and has been verified using a commercial ionization chamber (figure 4.6). Figure 4.6 shows output factors which are the response of the detector normalized to the response for a $10 \times 10 \text{ cm}^2$ radiation field. Output factors are shown for the BHJ before and after correction compared to a commercial ion chamber. After correction, the data match the ion chamber well, demonstrating the validity of our correction method. Furthermore, this example emphasizes the importance of the device and substrate contacts, the sample holder (and pogo pins), the size and length of connecting wires, and geometry of the irradiation field on the magnitude of the Compton current contribution.

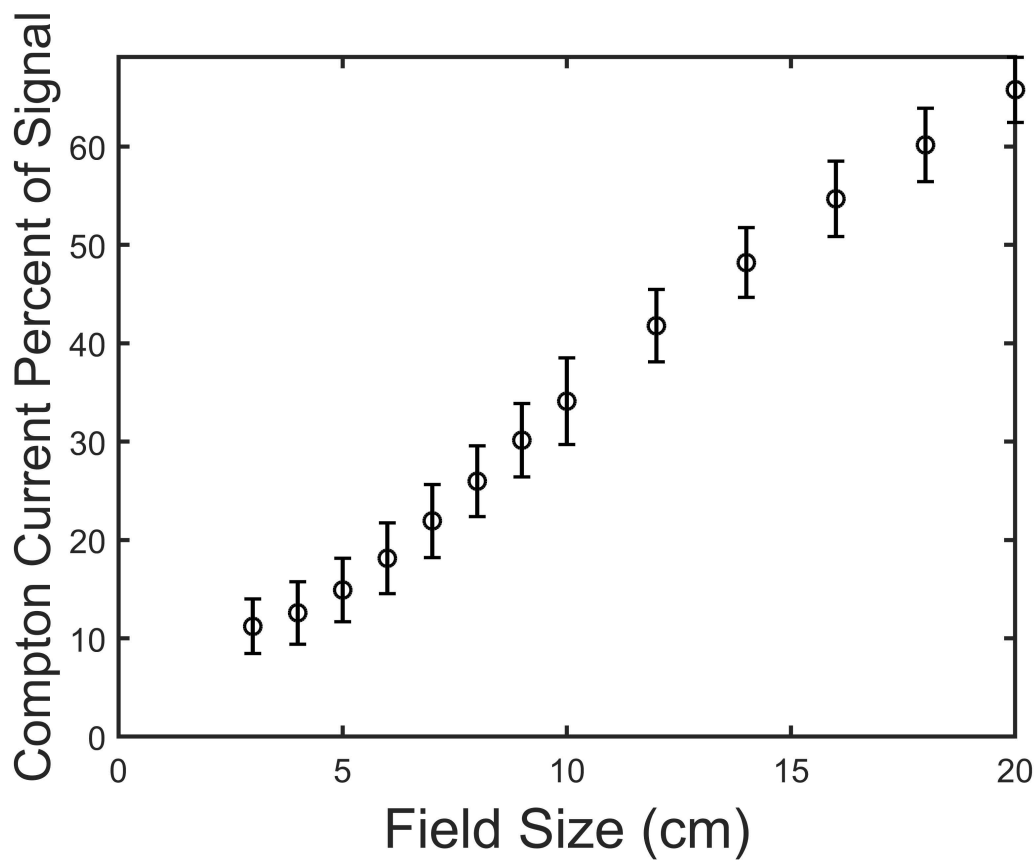


Figure 4.5: The percent of the total current comprised of Compton current (PS current divided by BHJ current from figure 4) is plotted as a function of field size. As the field size increases the percentage of the signal comprised of the Compton current increases.

4.3.6 Signal Change with Device Thickness

Figure 4.7 shows the current of BHJ diodes and the PS devices as a function of thickness. For the PS device there is no significant change with thickness because the signal is dominated by Compton current from the contacts, wires, etc. which does not change with PS thickness. The BHJ diode shows a significant increase in signal with thickness of device.

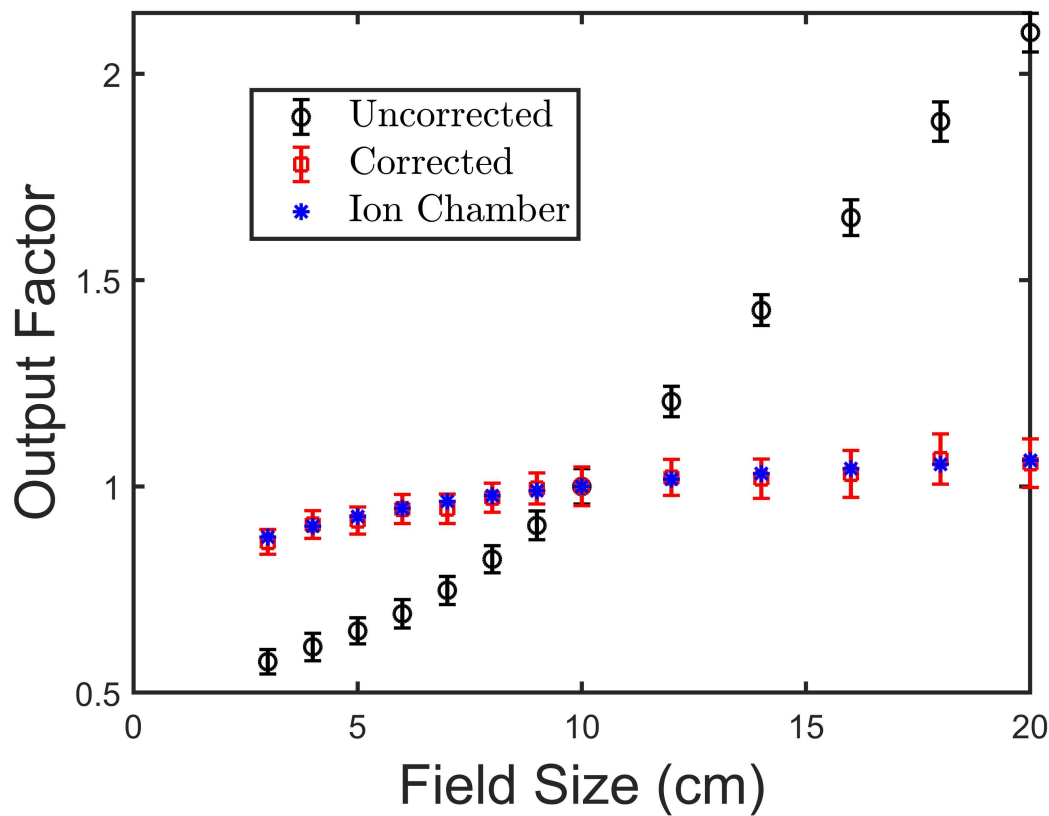


Figure 4.6: The output factor (detector response normalized to a 10x10 cm² field size) was measured for a 6 MV photon beam and compared to ion chamber measurements. The current is normalized to the signal measured with a 10x10 cm² field size. After the correction there is good agreement with the ion chamber. Figure taken from Hupman et al (2020) [66].

4.3.7 Suggestions to Reduce Compton Current

As demonstrated this correction technique has shown promising results. However, it is best to reduce the Compton current contribution as much as possible before implementing the technique. It is important to minimize the footprint of the electrodes, contacts, and wires where possible (this could include methods such as wire bonding for connections, and using the smallest gauge wires possible). Replacing ITO with organic conductors may reduce the contribution of the Compton current. The orientation of the detector should be chosen to reduce the footprint of the

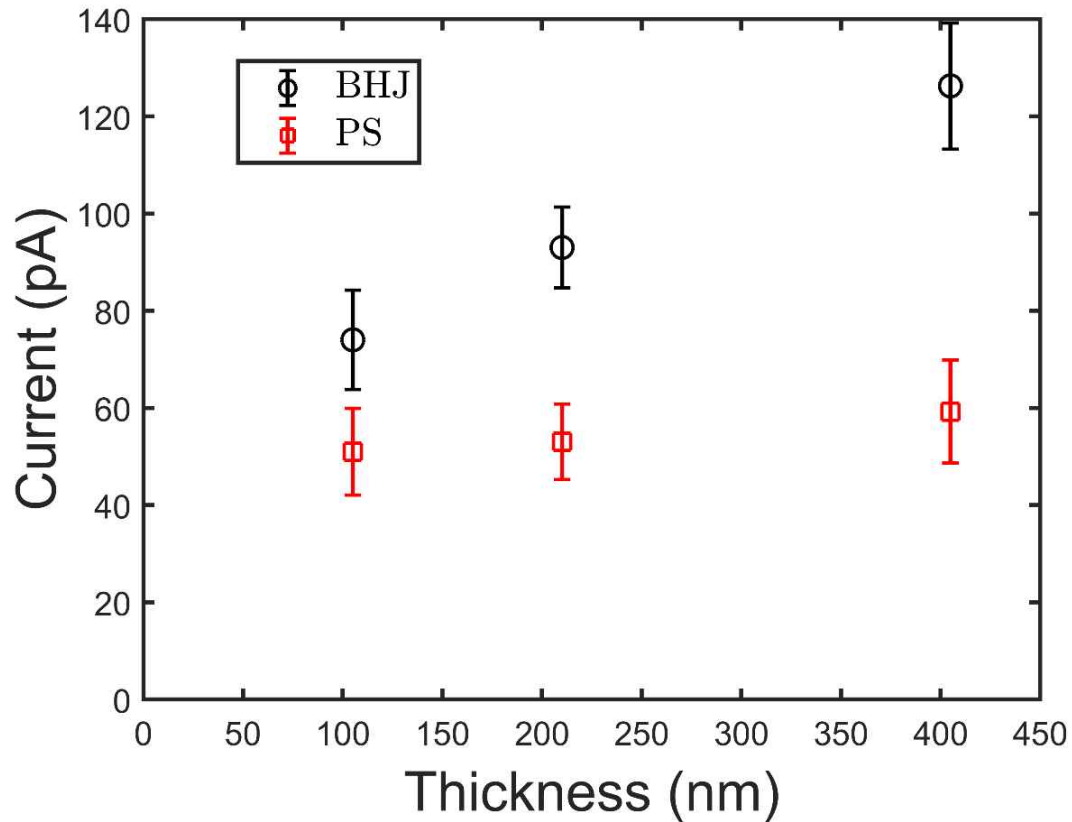


Figure 4.7: Current measured for three different thicknesses for the BHJ diode and the PS device. The BHJ diode shows an increase of current with thickness. The PS device shows no significant change in current with thickness. Data from figure 7 of Hupman et al (2020) were included in this figure for context [66].

wires in the beam.

4.4 Conclusion

In conclusion, we have presented a technique to correct the extraneous signal contributed due to interactions in the electrodes and wires when a thin-film photodiode is exposed to irradiation. The field size dependence shows that the magnitude of the problem depends on the length of wires placed within the irradiation beam. After using the correction technique the signal due to photocurrent originating within the BHJ agreed well with ion chamber measurements.

Chapter 5

Manuscript 3: Fabrication and Characterization of a Stemless Plastic Scintillation Detector

5.1 Preamble

Manuscripts 1 and 2 successfully characterized the photodiode in clinical radiation beams. Given the low sensitivity of the photodiode as a detector if used by itself, it was ideal for use as a light detector (i.e. collecting the light emitted by a scintillator) placed within the irradiation beam. This manuscript details the fabrication of a novel single element SPSD detector by coupling an organic scintillator to the photodiodes discussed in the first two manuscripts. Chapter 2 details the preparation of the scintillators and the irradiation setups used to characterize the SPSD.

This manuscript was published in the journal of Medical Physics:

- Hupman, Michael A., Thalath Monajemi, Irina Valitova, Ian G. Hill, and Alasdair Syme. November 2020. “*Fabrication and Characterization of a Stemless Plastic Scintillation Detector.*” *Medical Physics* 47(11):5882–89.

5.2 Abstract

Purpose: To fabricate a stemless plastic scintillation detector (SPSD) and characterize its linearity and reproducibility, its dependence on energy and dose per pulse; and to apply it to clinical PDD and output factor measurements.

Methods: An organic bulk heterojunction photodiode was fabricated by spin coating a blend of P3HT and PCBM onto an ITO-coated glass substrate and depositing

aluminum top contacts. Eljen scintillators ($\sim 5 \times 5 \times 5$ mm³; EJ-204, EJ-208, and EJ-260) or Saint-Gobain scintillators ($\sim 3 \times 3 \times 2$ mm³; BC-400 and BC-412) were placed on the opposite side of the glass using a silicone grease (optical coupling agent) creating the SPSD. Energy dependence was measured by using 100 kVp, 180 kVp, and 300 kVp photon beams from an orthovoltage treatment unit (Xstrahl 300) and 6 MV and 10 MV photons from a Varian TrueBeam linear accelerator. Linearity, dose per pulse dependence, output factors, and PDDs were measured using a 6 MV photon beam. PDDs and output factors were compared to ion chamber measurements. A control device was fabricated by substituting polystyrene (PS) for the P3HT/PCBM layer. No photocurrent should be generated in the control device and so any current measured is due to Compton current in the electrodes, wires, and surroundings from the irradiation. Output factors were corrected by subtracting the signal measured using the control device from the photodiode measured signal to yield the photocurrent.

Results: Each SPSD had excellent linearity with dose having an r^2 of 1 and sensitivities of 1.07 nC/cGy, 1.04 nC/cGy, 1.00 nC/cGy, 0.14 nC/cGy, and 0.10 nC/cGy for EJ-204, EJ-208, EJ-260 ($5 \times 5 \times 5$ mm³ volumes), BC-400, and BC-412 ($3 \times 3 \times 2$ mm³ volumes), respectively. No significant dose per pulse dependence was measured. Output factors matched within 1 % for the large scintillators for field sizes of 5×5 cm² to 25×25 cm², but there was a large under-response at field sizes below 3×3 cm². After correcting the signal of the small scintillators by subtracting the current measured using the PS control the output factors agreed with the ion chamber measurements within 1 % from field sizes 1×1 cm² to 20×20 cm². The impact of Cerenkov emissions in the scintillator were effectively corrected with a simple reflective coating on the scintillator. In comparison to a 6 MV photon beam the large scintillator SPSDs exhibited 37 %, 52 %, and 73 % of the response at energies 100 kVp, 180 kVp, and 300 kVp, respectively.

Conclusion: The principle of the SPSD was demonstrated. Devices had excellent linearity, reproducibility, no significant dose per pulse dependence and a simple reflective coating was sufficient to correct for Cerenkov emissions from within the scintillator. The devices demonstrated similar energy dependence to other scintillator detectors used in a radiotherapy setting.

5.3 Introduction

Plastic scintillation detectors (PSDs) are advantageous as high energy dosimeters because they are nearly water-equivalent, immediately responsive, have a long useable lifetime, and can have high spatial resolution [47, 57]. Plastic scintillators produce a quantity of light proportional to the energy absorbed for high energy photons and electrons. By measuring the light output the dose deposited can be determined. Clinical applications of PSDs include dosimetry of high energy photon and electron beams, brachytherapy, and in vivo dosimetry [47, 57, 89, 90, 58].

Beddar et al. showed that scintillator response is independent of total dose, dose rate, pressure, and has high spatial resolution [57]. Traditional PSDs are fabricated by coupling a scintillating element to the end of an optical fibre which is used to transport the scintillation light to an optical detector. The disadvantage of this design is the production of Cerenkov radiation in this optical “stem” which contaminates the scintillation signal. Cerenkov radiation is radiation produced when a charged particle passes through a medium at a speed greater than the speed of light in that medium. For high energy photons and electrons the production of Cerenkov light is proportional to dose. However, the amount of Cerenkov light reaching the optical detector depends on length of stem that is irradiated and the angle of incidence of the beam [47, 55]. Since a useful dosimeter must be deployable in geometries that differ significantly from calibration conditions, conventional PSDs require a Cerenkov radiation correction technique. Several techniques have been used to

various degrees of success, including: two-fiber subtraction, spectral filtering (or discrimination), and chromatic removal [57, 55, 56]. Furthermore, it has been shown that Cerenkov radiation is produced in the scintillator itself, further complicating the correction.⁸ Even with a correction, Cerenkov radiation can produce a dosimetric error greater than 10 % in certain circumstances [54].

The Exradin W1 (Standard Imaging, Middleton, WI, USA) was the first commercially available scintillation detector specifically designed for radiotherapy applications. It uses a spectral discrimination technique to correct for Cerenkov contamination [91]. Beierholm et al. found that the detector had reproducibility within 0.4 % under reference conditions, day-to-day variability within 0.4 %, and dose rate independence within 0.4 % [92]. However, a drawback they measured was a field size dependence as large as 3.3 % and 2.7 % for field size of 2x2 cm² and 40x40 cm², respectively. The authors suggested that the correction technique employed by the W1 for the stem effect was responsible for the observed discrepancies. Carrasco et al. found a reduction in response of the W1 detector of 0.28 %/kGy for the first 15 kGy of accumulated dose, followed by a further reduction of 0.032 %/kGy for dose 15 kGy to 127 kGy showing they are quite robust [91].

In previous work we have evaluated the response of organic field effect transistors, however, those devices were found to be insufficiently sensitive for common radiotherapy applications [80]. In this study we fabricated and characterized a new class of detector (the stemless plastic scintillation detector – SPSD) by coupling an organic scintillator to an organic photodiode. This eliminates the need for an optical fiber to carry the signal from the scintillator, thus eliminating the need for a stem correction while preserving the well-documented benefits of plastic scintillation detectors. Organic photodiodes should perform well due to their ability to absorb a high proportion of the light emitted from the scintillator while also not creating much signal due to direct interactions with the irradiation beam [66, 64, 93].

Kingsley et al. measured a reduction of $\sim 5\%$ in sensitivity with 0.5 kGy dose of a P3HT/PCBM photodiode device and a reduction of $\sim 30\%$ over 4 kGy when irradiated with 15 MV photon beam [84].

The SPSD was characterized with respect to linearity with dose and reproducibility. Its dependence on energy and dose per pulse was quantified. The impact of directional Cerenkov emission from the scintillator was quantified using an electron beam. A simple correction method for this dependence was investigated. Measurements of clinical data (PDD and output factors) were compared to an ion chamber. The devices studied herein are prototype devices in which the diodes are constructed on a glass slide and electrical connections are made with bulky metallic pogo pins that can generate a non-negligible current in certain measurement geometries. Although future work will minimize the extraneous signal in the device, in the current work, a correction method was used to permit the characterization of the scintillation signal as measured by the photodiodes [66].

5.4 Methods

5.4.1 SPSD Fabrication

Organic bulk heterojunction photodiodes were fabricated on ITO-coated glass substrates (ITO thickness ~ 110 nm) by spin coating a blend of P3HT and PCBM (~ 100 nm thick), and depositing aluminum top contacts (~ 80 nm thick) to define an active area of 9.75 mm² according to standard procedures [62, 61, 63]. A schematic diagram of the device layers is shown in figure 5.1. Eljen (Eljen Technology, Sweetwater, TX, USA) scintillators (EJ-204, EJ-208, and EJ-260) and Saint-Gobain (Saint-Gobain, Courbevoie, France) scintillators (BC-400 and BC-412) were stuck on the opposite side of the glass using a silicone grease (EJ-250). The Eljen scintillators were cut to approximately $5 \times 5 \times 5$ mm³ and the Saint-Gobain to $3 \times 3 \times 2$

mm³ and the sides polished. The scintillator coupled to the photodiode creates the detector which will hereafter be referred to as an SPSD. Although this device design eliminates an optical stem signal, these prototype devices still make use of bulky connector pins and other materials that can contribute an electrical signal that is independent of the desirable, optical signal. To quantify this signal, devices were also made with a polystyrene (PS) (Sigma-Aldrich, St. Louis, USA) layer in place of the BHJ layer. We have previously shown that this method effectively corrects the extraneous signal [66]. With this device no photocurrent should be generated from either the optical scintillation photons or the high energy particle interactions that take place in the active volume of the diodes (i.e. the device should not function as a photodiode) and any signal measured is due to Compton current in the electrodes, wires, and surroundings from the irradiation. The photocurrent will be calculated by subtracting the polystyrene current from the SPSD-measured current (this correction is only applied to output factors where the non-scintillation signal is significant).

5.4.2 SPSD Characterization

To measure linearity, the SPSD was irradiated with doses ranging from 1 cGy to 200 cGy with 6 MV photons, 10x10 cm² field size, at a depth of 5 cm in solid water (Sun Nuclear Corp., Melbourne, USA), and an SSD of 95 cm (figure 5.2). Three SPSDs were irradiated up to 1000 cGy. Output factors for each SPSD were measured with the same setup except the field size was varied from 1x1 cm² to 25x25 cm² with 200 cGy delivered for each field size three times. The output factors were compared with an Exradin A12 ion chamber (Standard Imaging, Middleton, WI, USA) for field sizes of 4x4 cm² to 25x25 cm² and with a semiflex 31010 micro ion chamber (PTW, Freiburg, Germany) for field sizes down to 1x1 cm² which was daisy chained with the Exradin A12 ion chamber (at 4x4 cm² field size). The same

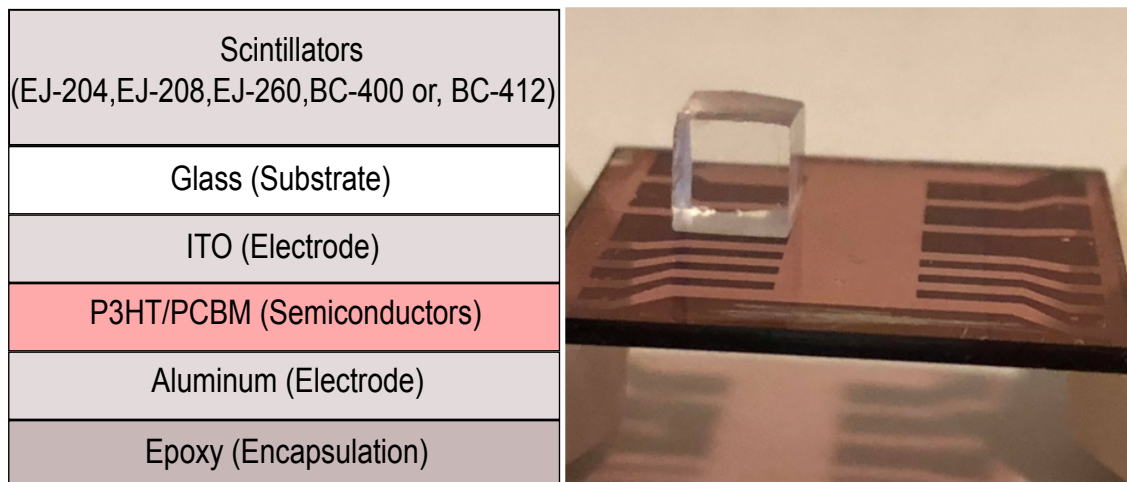


Figure 5.1: On the left is a schematic representation of the layers making up the stemless plastic scintillation detector (SPSD). The SSPD consists of a scintillator placed on top of a glass substrate where an organic photodiode has been fabricated on the opposite side. The P3HT/PCBM layer is replaced by PS for the control devices. The right shows an image of the SSPD. The substrate in the image has 12 photodiodes and the scintillator is coupled to one of them.

setup (with a field size of $10 \times 10 \text{ cm}^2$) was used for dose per pulse dependence except the SSD was varied from 80 cm to 125 cm. The dose delivered to the SSPD was determined using ion chamber measurements (Exradin A12) to facilitate the calculation of charge per dose at each SSD with the SSPD. The data (both dose per pulse and charge per unit dose) were then normalized at an SSD of 95 cm and the dependence quantified. PDDs were measured by placing solid water on top of the SSPD with a $10 \times 10 \text{ cm}^2$ field size and an SSD of 100 cm. The PDDs were compared to measurements with a CC13 ion chamber in a water tank. Energy dependence was measured by using 100 kVp, 180 kVp, and 300 kVp photon beams from an orthovoltage treatment unit (Xstrahl Ltd., Surrey, UK) and 6 MV and 10 MV photons from a Varian TrueBeam accelerator (Varian Medical Systems, Inc., Palo Alto, USA). Orthovoltage measurements were performed with a 5 cm diameter, 30 cm length cone with the SSPD placed on top of 15 cm of solid water to allow for backscatter (figure 5.2).

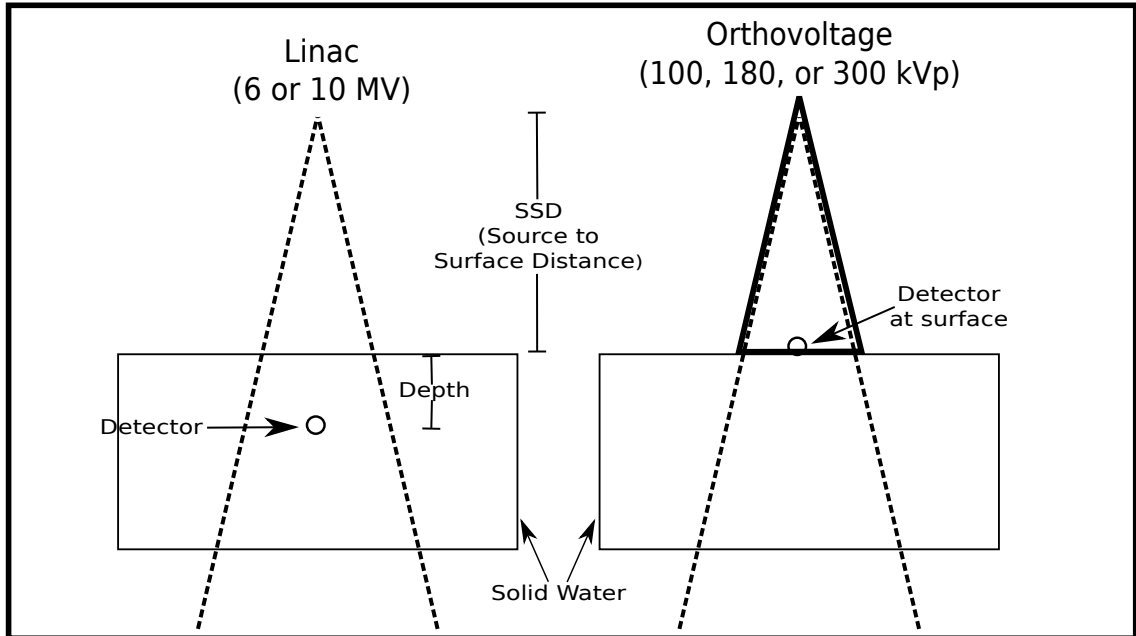


Figure 5.2: A schematic representation of the setup used to irradiate the SPSD with 6 and 10 MV photon beams (left) and using 100 kVp, 180 kVp, and 300 kVp photon beams (right).

As a preliminary investigation of the role of Cerenkov radiation in our detector we measured the signal with and without reflective tape on the scintillators. Measurements were performed at the surface for the large scintillators with 16 MeV electrons, $10 \times 10 \text{ cm}^2$ field size, SSD of 107 cm, and gantry angles varying from 0° to 45° . At each gantry angle the couch was shifted to ensure the SPSD was located along the central axis of the beam, causing an increased distance from the source to detector and decreasing the dose. For this reason measurements were compared to a PTW 60019 microDiamond (PTW, Freiburg, Germany) because it has been demonstrated to have low angular dependence over the range used [35]. Measurements were then repeated with the SPSD at a depth of 3 cm. In the absence of reflective tape, it is expected that the fairly uniform directionality of the electrons in the surface geometry, combined with the directionality of Cerenkov emission, will lead to a

directional dependence of the SPSSD [94]. This dependence may be reduced by ensuring more efficient collection of Cerenkov light regardless of its direction of emission. At depth, electron scattering should result in more isotropic Cerenkov emission, resulting in a smaller directional dependence [54].

5.5 Results

5.5.1 Linearity

The SPSSDs exhibited good noise characteristics with a coefficient of variability over 10 identical measurements of 0.14 %. The SPSSDs were irradiated with a 6 MV photon beam to doses ranging from 1 cGy to 200 cGy or 1 cGy to 1000 cGy (figure 5.3). SPSSDs showed excellent linearity over the dose range with sensitivities of 1.07 nC/cGy, 1.04 nC/cGy, 1.00 nC/cGy, 0.14 nC/cGy, and 0.10 nC/cGy for EJ-204, EJ-208, EJ-260, BC-400, and BC-412, respectively. The linear fit had an r^2 of 1 for each of the five SPSSDs and the inset of figure 3 shows the fit is reliable down to 1 cGy.

5.5.2 Dose Per Pulse

Figure 5.4 shows how each scintillator depends on dose rate and in particular the dose per pulse. The data are normalized at the dose per pulse corresponding to 95 cm SSD. The coefficients of variability were 0.17 %, 0.10 %, 0.14 %, 0.19 %, and 0.10 % for the scintillators EJ-204, EJ-208, EJ-260, BC-400, and BC-412, respectively. The data appears scattered with no obvious dependence. Furthermore, the variation over the range of doses per pulse compares to the variability of repeated measurements suggesting that the variation is random and no significant dose per pulse dependence over the range measured.

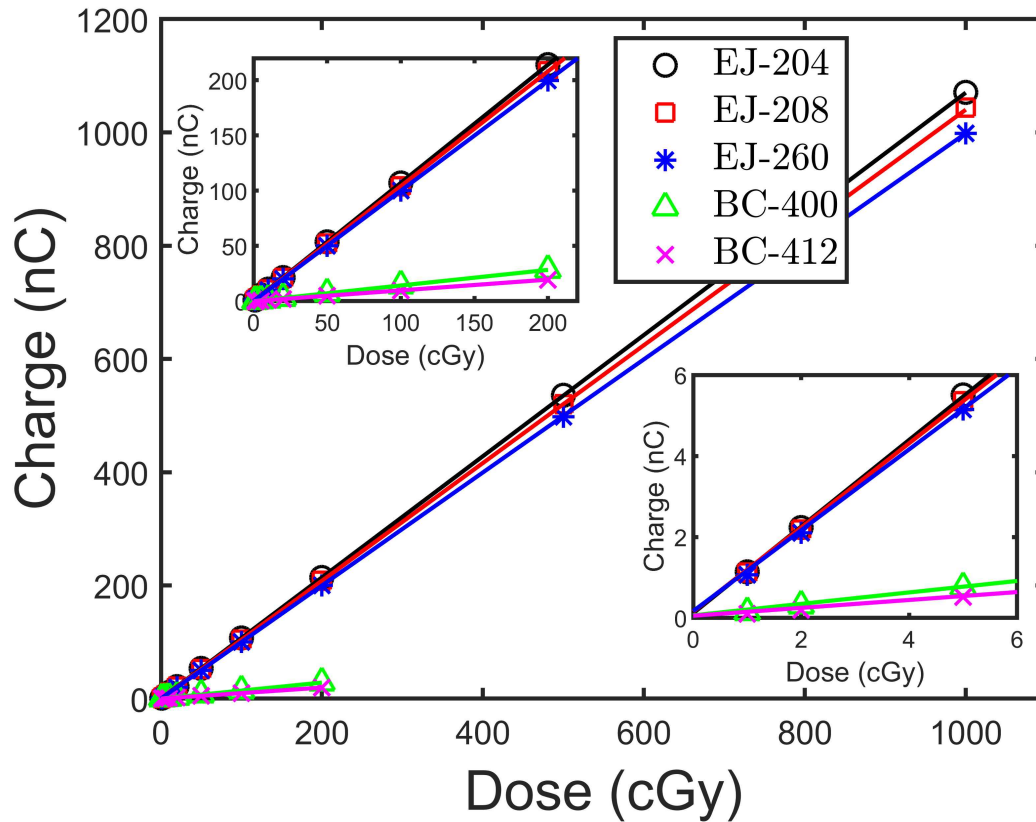


Figure 5.3: The charge collected as a function of dose for the three SPADs. Each SPAD exhibited a linear response and was sensitive to doses at 1 cGy.

5.5.3 Output Factors

The output factors for each of the five SPADs are shown in figure 5.5. Overall, the large SPADs match well with the ion chamber except at small field sizes ($4 \times 4 \text{ cm}^2$ and smaller). From $5 \times 5 \text{ cm}^2$ to $25 \times 25 \text{ cm}^2$ differences between the large SPADs and the ion chamber are less than 1%. At field sizes of $3 \times 3 \text{ cm}^2$ and below, there is a progressively larger under response, likely due to volume averaging effects. The small scintillators have a large deviation from the ion chamber over the range of field sizes. However, when re-normalized to the ion chamber at a field size of $4 \times 4 \text{ cm}^2$ (figure 5b) the small scintillators had better agreement with the ion chamber for smaller field sizes compared to the large scintillators.

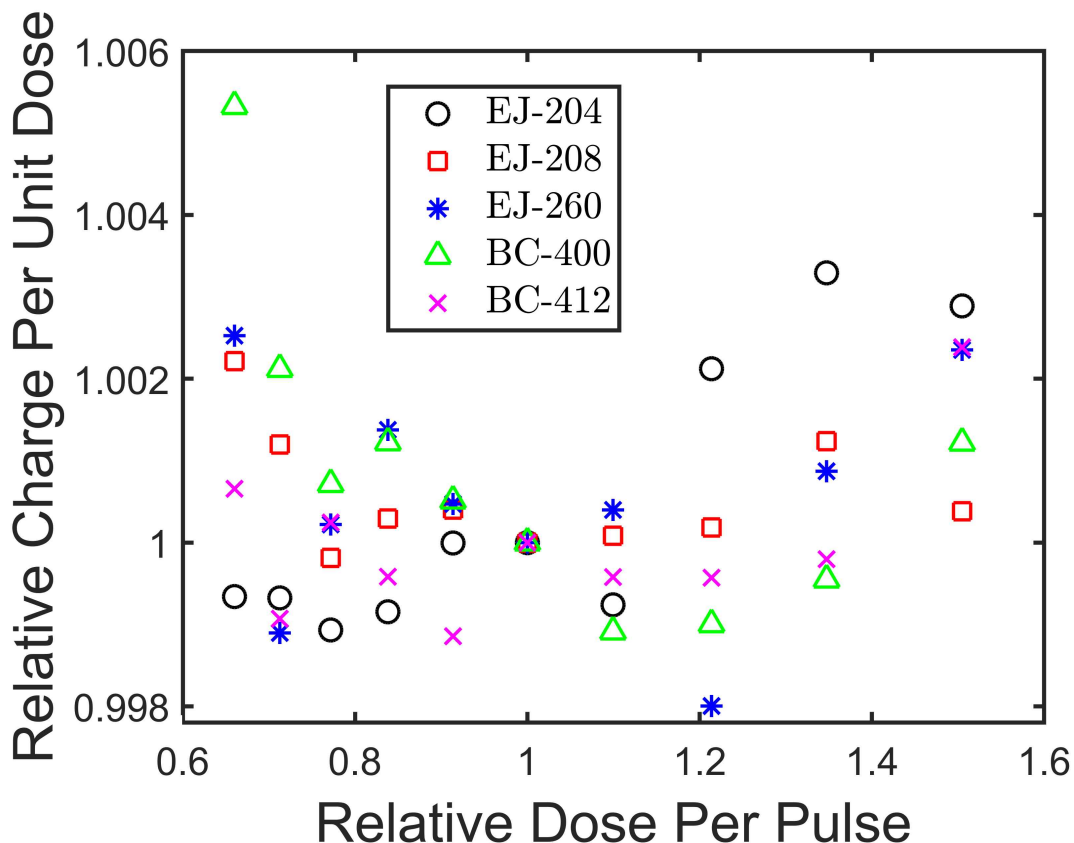


Figure 5.4: The dose per pulse was measured by varying the SSD from 80 cm to 125 cm and normalizing to 95 cm SSD. The charge per dose was then normalized at an SSD of 95 cm and the variation observed. There is no dependence observed with a variation of less than 0.4 % for of the value measured at 95 cm SSD for each of the SPSSDs.

5.5.4 Output Factors with non-scintillation signal subtracted

Figure 5.6 shows the output factors which have the non-scintillation signal subtracted by subtracting the current measured by the PS device. After subtraction the large scintillators see little difference because the non-scintillation signal makes up a very small portion of the total signal. However, after subtracting the non-scintillation signal from the small scintillators they agree with the ion chamber measurements within 1 % from field sizes $1 \times 1 \text{ cm}^2$ to $20 \times 20 \text{ cm}^2$. At small field sizes $1 \times 1 \text{ cm}^2$ to $4 \times 4 \text{ cm}^2$ (figure 6b) there is little change in the output factor because the non-scintillation signal makes a small portion of the total signal since the fields

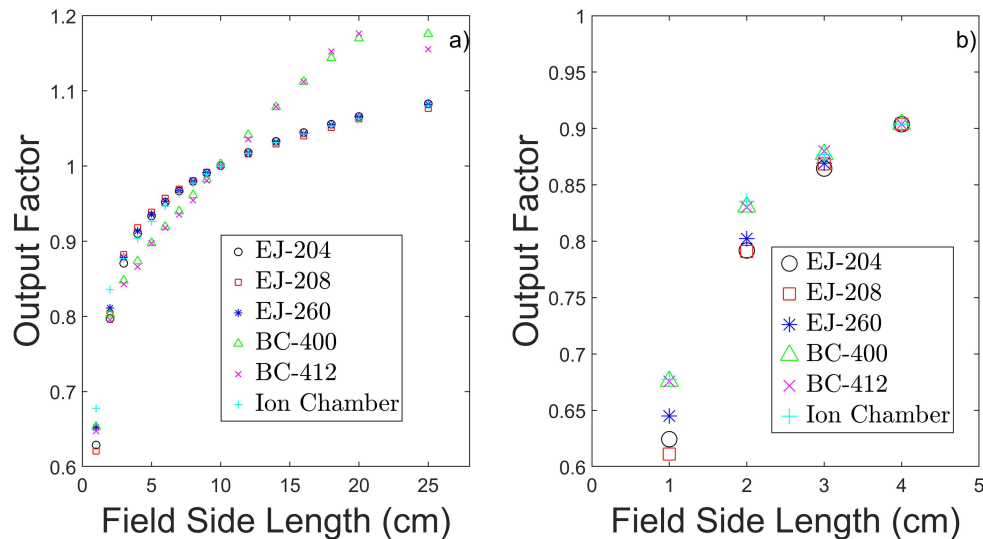


Figure 5.5: a) Output factors for the five SPSSDs are plotted. For comparison, output factors were measured using an Exradin A12 ion chamber from $4 \times 4 \text{ cm}^2$ to $25 \times 25 \text{ cm}^2$ and a semiflex 31010 micro ion chamber daisy chained for smaller field sizes. The three larger scintillators matched the output factor of the ion chamber well except at small field sizes where it deviated likely due to volume averaging. b) Output factors re-normalized to the ion chamber at a field size of $4 \times 4 \text{ cm}^2$. The large scintillators deviate from the ion chamber measurements which is possibly due to a volume averaging effect.

avoid significant overlap with the connectors and wires.

5.5.5 PDD

PDDs for each of the five SPSSDs were measured for both 6 MV and 10 MV by placing solid water on top of the SPSSDs and shifting the setup to maintain an SSD of 100 cm (figure 5.7). The PDDs matched the shape of the curves measured with the ion chamber well. However, some areas saw discrepancies of close to 2 %. The depth shown in the figure corresponds to the depth midway through the scintillator.

5.5.6 Energy Dependence

The response of the SPSSDs to photon beams of various energies normalized

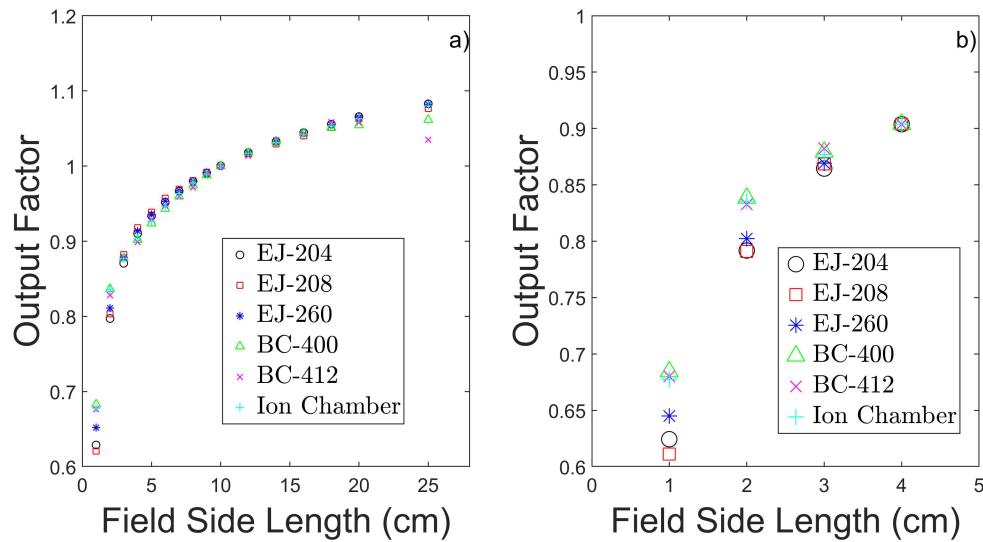


Figure 5.6: Output factors for the five SPDSs are plotted after the current measured using a PS device was subtracted. For comparison, output factors were measured using an Exradin A12 ion chamber from $4 \times 4 \text{ cm}^2$ to $25 \times 25 \text{ cm}^2$ and a semiflex 31010 micro ion chamber daisy chained for smaller field sizes. a) The output factors for the three large scintillators were not significantly affected by the correction (figure 5.5), but the small scintillator output factors were greatly improved. b) Output factors re-normalized to the ion chamber at a field size of $4 \times 4 \text{ cm}^2$. The large scintillators deviate from the ion chamber measurements which is likely due to a volume averaging effect.

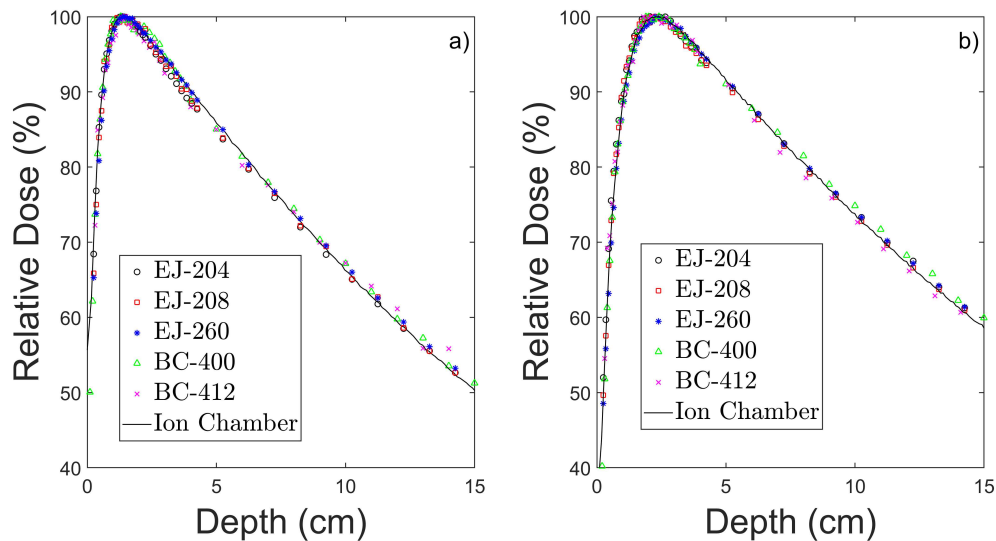


Figure 5.7: PDDs with the five SPDSs compared to an ion chamber for 6 MV (left) and 10 MV (right). The depth corresponds to the depth midway through the scintillator.

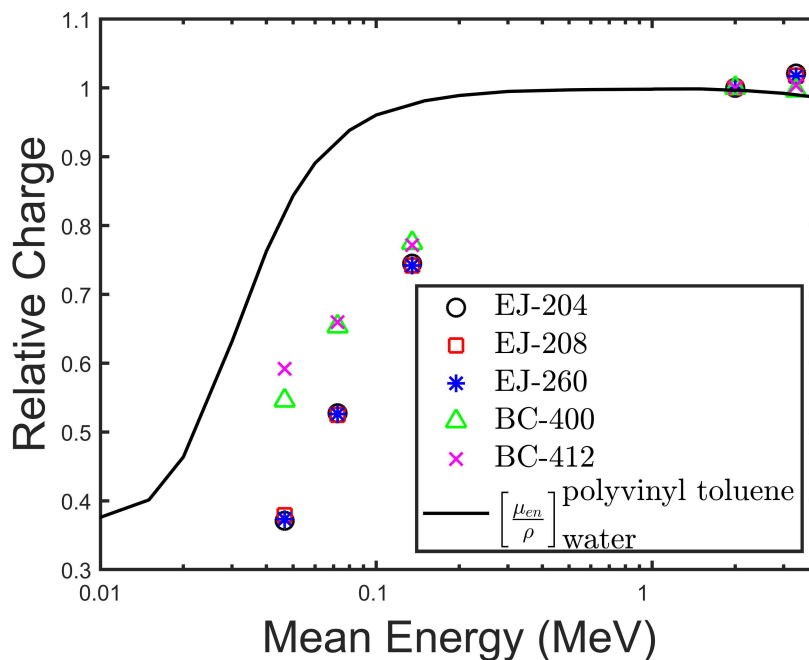


Figure 5.8: The energy dependence was observed by irradiating with 100 kVp, 180 kVp, 300 kVp as well as 6 MV and 10 MV. The relative charge is plotted for a 200 cGy dose delivery normalized to a 6 MV beam. The response of the SPSDs increases with energy. The ratio of the mass energy-absorption coefficient of polyvinyl toluene (main material of scintillator) to water is shown. The mass energy absorption coefficient ratios are included to illustrate that differences in this energy range will contribute to a reduction in water equivalence.

at 6 MV is shown in figure 5.8. The response for the three large scintillators at 100 kVp, 180 kVp, and 300 kVp in comparison to 6 MV are 37 %, 52 %, and 73 %, respectively. The small scintillators showed improved energy dependence at the kilovoltage energies. At 10 MV each SPSD had less than a 1 % increase of response in comparison to 6 MV. These data have not been corrected for the difference between the mass-energy absorption coefficients between polyvinyl toluene (material making up the scintillator) and water for each energy [95].

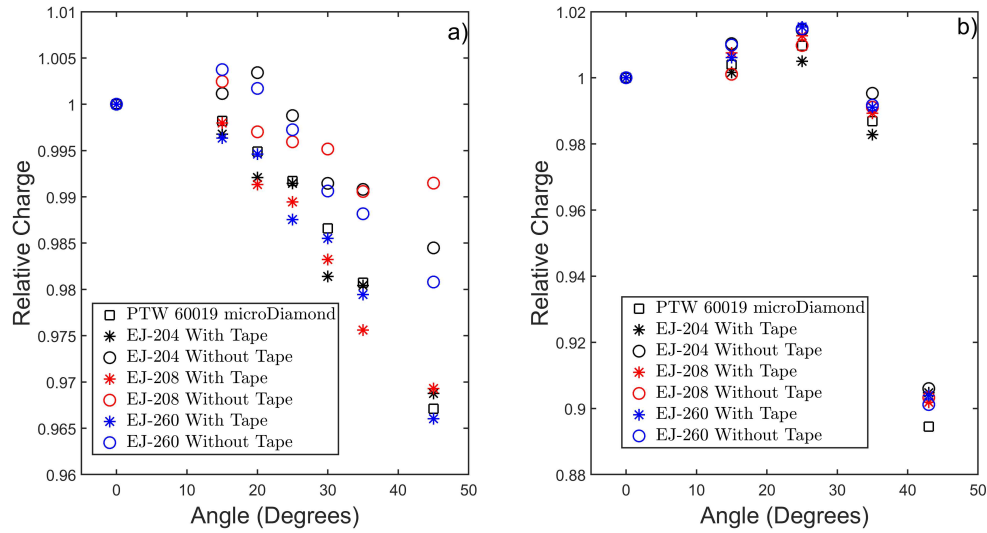


Figure 5.9: Directional dependence measured using a 16 MeV electron beam with the large scintillators with and without the use of reflective tape on the scintillator and compared to measurements with a diamond detector. a) Directional dependence at the surface. b) Directional dependence at a depth of 3 cm in solid water.

5.5.7 Impact of Cerenkov radiation

The response of the large SPSDs was measured at the surface with and without the use of a reflective tape on the scintillators. The data were compared to a diamond detector and the results are shown in figure 5.9a. At the surface the SPSDs had a maximum difference from the diamond of about 0.6 % and 2.5 % with and without the reflective tape, respectively. This maximum difference without reflective tape was observed at a gantry angle of 45°. At a depth of 3 cm the presence of reflective tape does not have a material impact on the signal of the SPSD as a function of beam angle (figure 5.9b). SPSDs saw an average increase of signal of 1.7 times when using reflective tape.

5.6 Discussion

The SPSDs all showed excellent linearity with dose with an r^2 of 1 for doses 1 cGy to 200 cGy or 1 cGy to 1000 cGy. Furthermore, the SPSDs exhibited good

reproducibility (coefficient of variability of 0.14 % over 10 measurements), no significant dose per pulse dependence, and good sensitivity (0.10 nC/cGy to 1.07 nC/cGy).

The larger scintillators (5x5x5 mm³; Eljen) measured a large under-response for small field size output factors likely due to volume averaging. The small scintillators (3x3x2 mm³; Saint-Gobain) can capture the output factors more accurately at small field sizes (figure 5.5b). However, the small scintillators show large differences over the range of field sizes measured which is due to a non-scintillation signal (i.e. Compton current induced in the wires). The fraction of the total signal contributed by extraneous (i.e. non-scintillator) signal increases as a function of field size. By subtracting the polystyrene measured current from the SPSDs the scintillation signal is calculated. Since the output factor is a ratio of signals (signal at chosen field size divided by signal at 10x10 cm² field size), when the chosen field size is larger than 10x10 cm², the fraction of the signal subtracted is larger for the term in the numerator compared to the one in the denominator, so the corrected output factor gets smaller (compared to the uncorrected value - see figure 5.5a/5.6a). Conversely, when the field size is smaller than 10x10 cm², the fraction of the signal subtracted is smaller for the term in the numerator compared to the one in the denominator, so the corrected output factor gets larger compared to the uncorrected value. After correction, the small scintillators agreed within 1 % of ion chamber measurements for field sizes 1x1 cm² to 20x20 cm². The non-scintillation signal is more significant for the small scintillators due to the decreased signal from the scintillator. In the future, the SPSD will be optimized to minimize the extraneous (non-scintillation) signal by reducing the metallic footprint of connectors (including the use of organic conductors), using a more efficient scintillator, and selecting materials for the BHJ diode to match the emission spectrum of the scintillator.

The SPSDs showed an increased response with energy in the kV range, but showed little energy dependence in the MV range. The dependence in the kV range

is likely partly due to the mass attenuation-energy absorption coefficient difference between polyvinyl toluene (the main material of the scintillator) and water and partly due to quenching [95, 48]. Large scintillators had an energy dependence similar to previously published values (figure 5.8) [48, 96]. Ratios of coefficients at particular energies are not necessarily predictive of detector response when exposed to sources that emit a broad spectrum of energies, but are included to illustrate that differences in energy absorption in this energy range will contribute to a reduction in water equivalence. More work is needed with SPSDs to quantify how much each mechanism contributes. The energy dependence of the SPSDs was reduced when using smaller scintillators. This is in part because the diode, which has a decreased response with energy in the kV range, will contribute a more significant portion of the measured signal [66]. The dose gradient across the larger scintillators at these energies may also contribute to the enhanced energy dependence. The data suggest that it may be possible to find an optimal scintillator thickness to minimize the energy dependence of the device.

PSDs are most commonly used with an optical fiber to carry the light from the scintillator to a detector. Cerenkov radiation produced in the optical fiber can contaminate the signal and must be corrected. In our setup we remove the optical fiber and use an organic photodiode to collect the light which should help mitigate the Cerenkov problem. However, it has been shown that Cerenkov will be produced in the scintillator itself [54]. To help understand how problematic the Cerenkov radiation could be in our SPSD we have measured the directional dependence on the surface using a 16 MeV electron beam since this setup produces a relatively unidirectional beam of electrons which will, in turn, maximize the directionality of the Cerenkov emissions. The use of reflective tape in this setting is a first test of a simple correction strategy. Without the reflective tape the difference between the SPSDs and the diamond detector reached a maximum of 2.5 % for a gantry angle

of 45° (close to the optimal angle for Cerenkov coupling to the diode), while using reflective tape produced differences of less than 0.5 % across the range of angles studied. With reflective tape the directional dependence may be reduced because the Cerenkov radiation can be efficiently collected independent of the incident beam angle. When the tape is removed most of the Cerenkov radiation not directed at the photodiode will not be collected. Using the reflective tape increased the SPSSD signal by a factor of approximately 1.7. At a depth of 3 cm there is no difference between relative signal as a function of gantry angle for measurements with and without reflective tape on the scintillator. This likely results from more diffuse distribution of electron paths through the scintillator at this depth which should decrease the directionality of the Cerenkov radiation (figure 5.9b) [97].

5.7 Conclusion

Five types of SPSSDs were fabricated by coupling Eljen (EJ-204, EJ-208, and EJ-260) or Saint-Gobain (BC-400 and BC-412) scintillators to P3HT/PCBM bulk heterojunction organic photodiodes. The SPSSDs allow the measurement of the light from a scintillator without the use of an optical fiber which should reduce the Cerenkov radiation contaminating the signal while maintaining the benefits scintillators have as radiation detectors. The SPSSDs exhibited excellent linearity with dose, no significant dose per pulse dependence over the range measured, and an increase response with energy in the kV range comparable to energy dependence previously published with plastic scintillation detectors. Cerenkov light generated in the scintillator can be efficiently collected with the use of reflective tape. This effectively eliminates the directional dependence associated with Cerenkov light emission. Future work will aim to reduce the extraneous signal in the devices.

5.8 Acknowledgements

This work was supported in part by a natural sciences and engineering research council of Canada (NSERC) Discovery Grant and NSERC postgraduate scholarship-doctoral (PGS-D).

Chapter 6

Manuscript 4: Measuring Small Field Profiles and Output Factors with a Stemless Plastic Scintillator Array

6.1 Preamble

This manuscript builds off of the single-element SPSD fabricated and characterized in manuscript 3. In this work a novel 1D array SPSD is fabricated and used to measure small field profiles and output factors. The quality of the detector was compared to commercial detectors that included ion chambers, film, and diamond detector measurements. The work investigates the various geometries of scintillators that includes four bulk scintillators with differing dimensions, as well as one detector that has been segmented to reduce cross-talk.

The single element-SPSD fabricated in manuscript 3 could be used for point measurements, allowing it to be used as a tool for in vivo dosimetry or it could be swept in a water tank to measure PDDs. An array detector could be used clinically for QA of small fields that includes measuring output factors and beam profiles simultaneously.

This manuscript has been submitted to the journal of Medical Physics on April 20, 2021.

6.2 Abstract

Purpose: To fabricate a 1D stemless plastic scintillation detector (SPSD) array using organic photodiodes and to use the detector to measure small field profiles

and output factors.

Methods: An organic photodiode array was fabricated by spin coating a mixture of P3HT and PCBM organic semiconductors onto an ITO-coated glass substrate and depositing aluminum top contacts. Four bulk scintillators of various dimensions were placed on top of the photodiode array. A fifth scintillator was used that had been segmented by laser etching and the septa filled with a black paint. Each detector array was first calibrated using a reference field of 95 cm SSD, 5 cm depth, and 10 x 10 cm² field size for a 6 MV photon beam. After calibration, profiles were measured for three small field sizes: 0.5 x 0.5 cm², 1 x 1 cm², and 2 x 2 cm². Using the central pixel of the array, output factors were measured for field sizes of 0.5 x 0.5 cm² to 25 x 25 cm². Small field profiles were compared to film measurements and output factors compared to ion chamber measurements.

Results: The segmented scintillator measured profiles that were in good agreement with film for all three field sizes. Output factors agreed to within 1.2 % of ion chamber over the field size range of 1 x 1 cm² to 25 x 25 cm². At 0.5 x 0.5 cm² the segmented scintillator underestimated the output factor compared to film and a microDiamond detector. Bulk scintillators failed to produce good agreement with film for measured profiles and deviation from ion chamber for output factors were apparent at field sizes below 5 x 5 cm². In comparison to a bulk scintillator of dimensions 5 x 5 x 0.5 cm³ the etched scintillator saw a reduction of 5.1, 7.1, and 10.5 times the signal for field sizes of 0.5 x 0.5 cm², 1 x 1 cm², and 2 x 2 cm² field sizes, respectively. The reduction of signal comes from reduced cross-talk which was present in all of the bulk scintillator geometries to various degrees.

Conclusion: A 1D SPSD array was demonstrated with various scintillator designs. The etched scintillator array demonstrated excellent small field profile measurements when compared to film and output factors when compared to micro ion chamber and diamond detector measurements.

6.3 Introduction

Stereotactic radiosurgery/radiotherapy treatments are characterized by the use of small fields, large doses per fraction and steep dose gradients outside the target volumes. Accurate measurements to characterize these fields are essential to ensure safe and effective treatment deliveries using these techniques.

In small field dosimetry many detectors need a correction factor due to the lack of charged particle equilibrium, chamber size, dose perturbation, and non-water equivalence of material [6, 98]. Failure to apply these correction factors to dose measurements can result in significant errors. Detectors that have a small correction factor include plastic scintillation detectors (PSDs) such as the Exradin W1 and W2 [99]. Plastic scintillating detectors are water-equivalent at megavoltage energies, and they emit light proportional to the absorbed energy when irradiated with high energy photons and electrons. Typically, the light produced is carried to an optical sensor using an optical fiber. A disadvantage of PSDs is that they suffer from Cerenkov radiation contaminating the signal, which needs to be corrected [47, 55]. Cerenkov radiation is produced when a charged particle such as an electron travels through a material faster than the speed of light in that material. Most of the Cerenkov radiation is typically created in the optical fiber because the length of optical fiber in the irradiation beam is typically much longer than the scintillator.

In previous work we developed a stemless plastic scintillation detector by removing the optical fiber and measuring the light emitted by the scintillator using an organic photodiode attached to the scintillator [68]. We fabricated the photodiodes using P3HT and PCBM organic semiconductors. The results showed the detector had a linear response with dose, no dose per pulse dependence, and the energy dependence was consistent with the energy dependence of an organic scintillator coupled to an optical fiber.

Arrays designed to measure small fields should be water equivalent, have no dose rate dependence, have high spatial resolution, and have real-time readout. EBT3 Gafchromic films have high spatial resolution and little energy dependence, but do not have real-time readout and requires a stringent protocol to minimize errors due to readout [29]. Silicon diode arrays have excellent spatial resolution and are readout in real-time [100, 101]. However, they have a dose per pulse dependence, angular dependence, and energy dependence, all of which depend on the design of the array and surrounding materials [102, 103]. Several array designs have been fabricated based on silicon diodes with various distributions of detector elements and sensitive volumes [102, 104, 105]. These arrays showed excellent clinical potential with accurate measurements of output factors, PDDs, and profiles. However, these detectors did show a dose per pulse dependence, which could be corrected for specific QA applications, but may be problematic for patient specific dose verifications [102]. Furthermore, the array exhibited an angular dependence which could be problematic depending on the application. Our array based on scintillating detectors may overcome some of these drawbacks. Previous work with a single-element SPSD showed no dose per pulse dependence [68]. Other works have shown that scintillators have little angular dependence once Cerenkov is corrected for [91].

In this work we expand on our previous work, by fabricating an SPSD array capable of measuring a one-dimensional dose profile. The detector consists of 35 photodiodes over a distance of approximately 4.5 cm. We explore the impact of scintillator shape and size, and how segmentation affects profiles measurements. Simultaneous acquisition of small field output factors is also described.

6.4 Methods

The P3HT (Brilliant Matters, Quebec City, Canada)/PCBM (Solenne BV, Groningen, Netherlands) photodiode array was fabricated following established

methods from the photovoltaic literature [62, 61, 63]. A 50 mm x 75 mm ITO-covered glass substrate (Delta Technologies LTD., Loveland, USA) was patterned by etching the ITO using hydrochloric acid for 6 minutes. The substrate was cleaned by sonicating for 15 minutes each in successive solutions of Sparkleen (Thermo Fisher Scientific, Waltham, USA) in deionized water, deionized water, acetone, and ethanol. Next PEDOT:PSS (Clevios P VP Al 4083, Heraeus, Hanau, Germany) was spin coated for 60 s at 5000 rpm and then placed on a hotplate for 20 min at 150 °C. A 2 % by weight solution of P3HT and PCBM in chlorobenzene (Sigma-Aldrich, St. Louis, USA) was spin coated for 1 min at 2000 rpm and placed on a hotplate for 1 h at 110 °C. Next aluminum top electrodes were deposited with vacuum thermal evaporation through a stencil mask at 1 Å/s to a thickness of 80 nm. The array consisted of 35 photodiodes, each with an active area of approximately 1 x 4 mm². Spacing between each photodiode is approximately 0.27 mm, which results in a length of approximately 4.5 cm for the entire array.

Two different scintillators were used in this work. EJ-204 (Eljen Technology, Sweetwater, TX, USA) with a thickness of 5mm and BC-400 (Saint-Gobain, Courbevoie, France) with a thickness of 2 mm. Non-etched scintillators were cut to a size of 5 x 5 cm² (square, abbreviated S) or 0.5 x 5 cm² (rectangular, abbreviated R), which would just cover the photodiode array (figure 6.1a and 6.1b). Therefore, there are four non-etched scintillator geometries that will be abbreviated as 5S (5 x 5 x 0.5 cm³), 5R (5 x 0.5 x 0.5 cm³), 2S (5 x 5 x 0.2 cm³), and 2R (5 x 0.5 x 0.2 cm³). A 5 mm thick EJ-204 scintillator was segmented using a Bodor laser etcher (Bodor Ltd., Jinan City, China) to create air gaps between each photodiode. Black paint (XF-1, Tamiya Inc., Shizuoka, Japan) was used to fill in the gaps to decrease the cross-talk (figure 6.1c and 6.1d). Scintillators were polished by sanding with progressively finer grit sand paper.

The SPSD array detector was then made by placing the scintillators on the

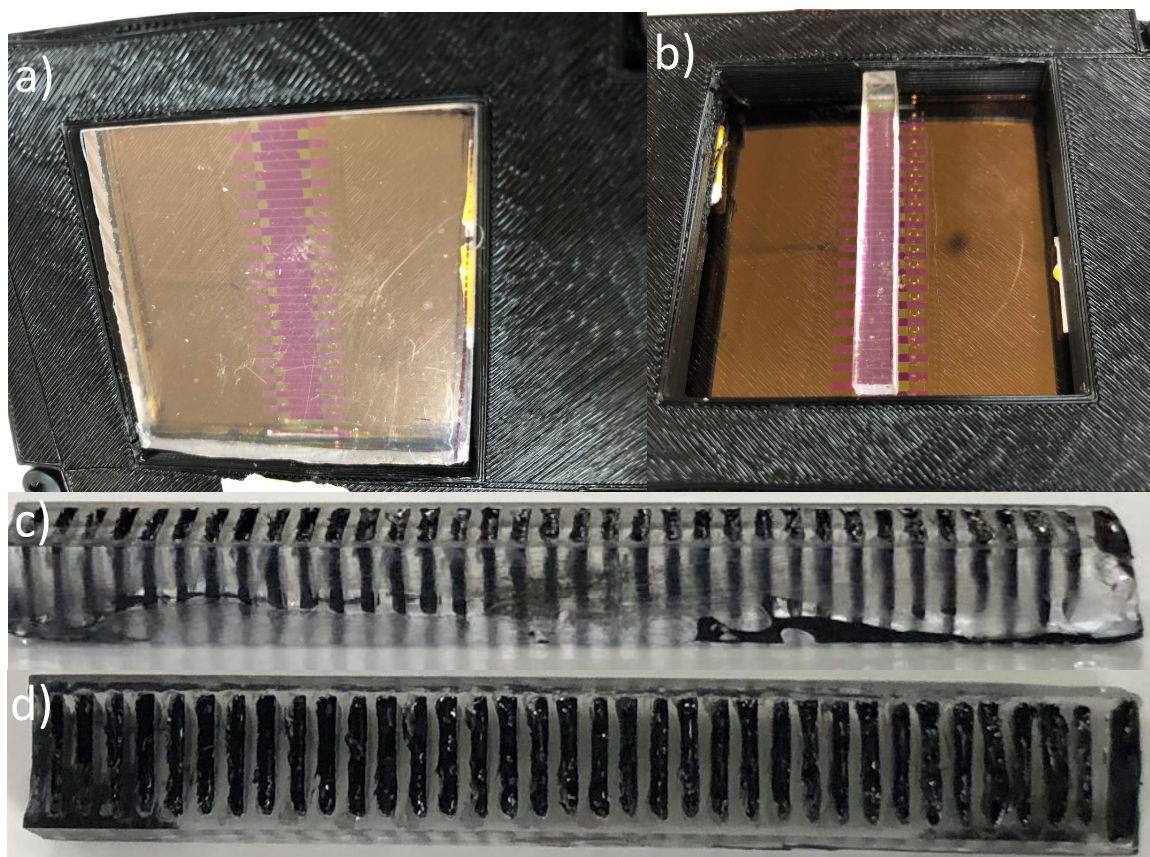


Figure 6.1: a) Picture of the photodiode array with the square ($5 \times 5 \text{ cm}^2$) and 5 mm thick scintillator placed on top. The black is a 3D printed holder to make contacting each photodiode easier and more reproducible. b) Picture of the photodiode array with the rectangular ($5 \times 0.5 \text{ cm}^2$) and 5 mm thick scintillator. For experiments 3D printed material was used to fill in all air gaps. c) Side view of the etched scintillator with black paint in the septa. d) Top view of the etched scintillator with black paint in the septa.

organic photodiode array with an optical coupling gel (EJ-550, Eljen Technology, Sweetwater, TX, USA). While these detectors eliminate an optical stem signal there is still an electrical signal that is independent of the desirable optical signal due to the bulky connector pins and other materials used to measure the signal from this prototype device. To quantify this signal, the P3HT/PCBM semiconducting layer was replaced with a polystyrene (PS) (Sigma-Aldrich, St. Louis, USA) layer. As

we have previously shown, this PS device should not generate signal due to optical scintillation photons or interactions in the volume of the photodiodes (i.e. the device should not function as a photodiode) [66]. Thus any signal measured is due to Compton current in the electrodes, wires, etc. and gives an indication of the improvements that could be made with a more optimal design.

The SPSD array was first irradiated in a $10 \times 10 \text{ cm}^2$ field under in house reference conditions (95 cm SSD, 5 cm solid water buildup, 600 MU/min) and the response of each device was measured. Next, the array was shifted by one pixel and this process repeated. This allowed us to calculate a calibration factor between a given array element and its immediate neighbor. By calibrating the central detector against a reference dosimeter (i.e. ion chamber), we were then able to obtain calibration values for the entire array as described in previously published work [106, 107, 108]. The array was then irradiated in field sizes of $0.5 \times 0.5 \text{ cm}^2$, $1 \times 1 \text{ cm}^2$, and $2 \times 2 \text{ cm}^2$ and the signal of each pixel normalized to the central pixel to obtain profiles, which were compare to film. We readout two pixels simultaneously. One was always the central pixel to ensure the sensitivity of the array did not change and the other one was varied to measure each pixel of the array. The assumption was if the sensitivity decreased due to radiation damage it would be detected by continuously measuring the central pixel. No significant decrease in signal of the central pixel was measured. Output factors were determined by using the signal of the central detector irradiated with an SSD of 95 cm and depth of 5 cm in solid water for field sizes of $0.5 \times 0.5 \text{ cm}^2$ to $25 \times 25 \text{ cm}^2$ and normalizing it to the response of a $10 \times 10 \text{ cm}^2$ field. Output factors were determined by using the signal of the central detector for field sizes of $0.5 \times 0.5 \text{ cm}^2$ to $25 \times 25 \text{ cm}^2$. For field sizes $4 \times 4 \text{ cm}^2$ to $25 \times 25 \text{ cm}^2$ an A12 ionization chamber (Standard Imaging, Middleton, WI, USA) was used to compare our results. For smaller field sizes a semiflex

31010 micro ion chamber (PTW, Freiburg, Germany) and a PTW 60019 microDiamond (PTW, Freiburg, Germany) detector were used. A common reference point for the A12, semiflex 31010 and PTW 60019 was chosen as $4 \times 4 \text{ cm}^2$ to permit reporting of all output factors with field size-appropriate detectors (i.e. the detectors were daisy chained at a field size of $4 \times 4 \text{ cm}^2$). MicroDiamond measurements were performed in a water tank and ion chamber measurements performed in solid water. The output factors for these detectors were corrected using the correction factors in TRS-483 [6]. The semiflex 31010 micro ion chamber used correction factors of 1.001 and 1.008 for field sizes of $3 \times 3 \text{ cm}^2$ and $2 \times 2 \text{ cm}^2$, respectively. The micro ion chamber was not used for field sizes below $2 \times 2 \text{ cm}^2$ because no correction factors are listed due to excessive error. The correction factors used for the PTW 60019 microDiamond detector were 0.997, 0.984, and 0.962, for field sizes of $2 \times 2 \text{ cm}^2$, $1 \times 1 \text{ cm}^2$, and $0.5 \times 0.5 \text{ cm}^2$, respectively.

Small field profiles were measured with EBT3 gafchromic film (Ashland Specialty Ingredients, Bridgewater, NJ) in solid water with the same setup parameters as the SPSD array for comparison. The films were scanned with an EPSON EXPRESSION 10,000 XL, with a 48 bit colour-depth, and a resolution of 300 dpi. The film was pre-scanned seven times to ensure uniform heating of the bulb in the scanner and was placed at the same location and orientation (for calibration and experiment) on the scanner. The film was scanned 24 hours after irradiation to allow the film to develop. A triple-channel film dosimetry algorithm outlined in Mayer et al. was used to calculate the dose to the film [73]. The etched scintillator SPSD was compared to the film profile measurements using a gamma analysis with two different distance to agreement/dose difference evaluation criteria: 1%/1mm and 2%/2mm [109].

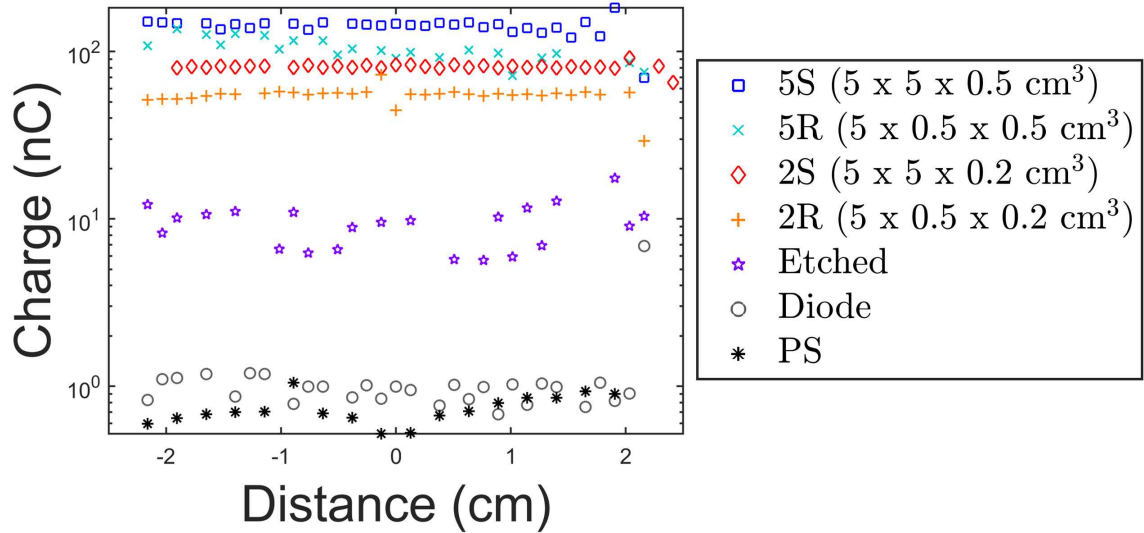


Figure 6.2: The charge (uncorrected) is plotted as a function of device location for an irradiation of 200 cGy using a $10 \times 10 \text{ cm}^2$ field size. The legend shows scintillator geometries of 5S ($5 \times 5 \times 0.5 \text{ cm}^3$), 5R ($5 \times 0.5 \times 0.5 \text{ cm}^3$), 2S ($5 \times 5 \times 0.2 \text{ cm}^3$), 2R ($5 \times 0.5 \times 0.2 \text{ cm}^3$), and etched ($5 \times 0.5 \times 0.5 \text{ cm}^3$ with septa). The diodes and PS (polystyrene) were irradiated with no scintillator on top of the array.

6.5 Results

Figure 6.2 shows the charge (uncorrected) collected by each individual photodiode of the SPSD array for each scintillator geometry, and for the photodiode and PS array without a scintillator when irradiated with 200 cGy in a $10 \times 10 \text{ cm}^2$ field. Under these conditions, the charge collected (mean and standard deviation) was $140 \pm 17 \text{ nC}$, $100 \pm 17 \text{ nC}$, $81 \pm 4 \text{ nC}$, $55 \pm 6 \text{ nC}$, and $10 \pm 3 \text{ nC}$ for the 5S, 5R, 2S, 2R, and etched scintillators, respectively. With no scintillator on the photodiodes the charge collected was $1 \pm 1 \text{ nC}$ and for the PS array was $0.9 \pm 0.2 \text{ nC}$.

Figure 6.3 shows the charge (uncorrected) collected of the SPSD array for each scintillator geometry for the field sizes of $0.5 \times 0.5 \text{ cm}^2$, $1 \times 1 \text{ cm}^2$, and $2 \times 2 \text{ cm}^2$. The charge measured at the center of the field reduces by factors of 5.1, 7.1, and 10.5 in the etched scintillator when compared to the 5S scintillator for field sizes of $0.5 \times 0.5 \text{ cm}^2$, $1 \times 1 \text{ cm}^2$, and $2 \times 2 \text{ cm}^2$, respectively. The magnitude of the

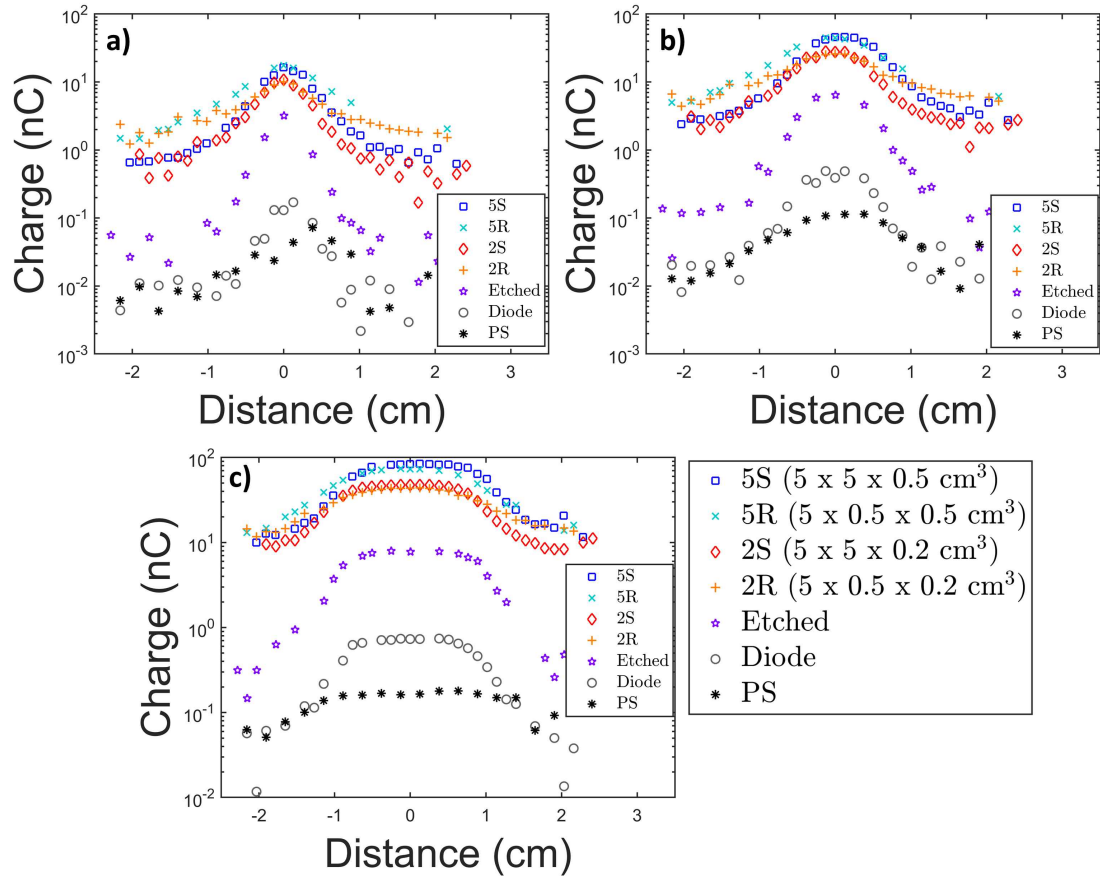


Figure 6.3: The charge (uncorrected) collected for each pixel is plotted when irradiated with 200 MU for field sizes of a) $0.5 \times 0.5 \text{ cm}^2$ b) $1 \times 1 \text{ cm}^2$ and c) $2 \times 2 \text{ cm}^2$. The abbreviations in the legend stands for 5S ($5 \times 5 \times 0.5 \text{ cm}^3$), 5R ($5 \times 0.5 \times 0.5 \text{ cm}^3$), 2S ($5 \times 5 \times 0.2 \text{ cm}^3$), 2R ($5 \times 0.5 \times 0.2 \text{ cm}^3$), etched ($5 \times 0.5 \times 0.5 \text{ cm}^3$ with septa), diode (no scintillator placed on the array), and PS (polystyrene) where the organic semiconductors in the photodiodes have been replaced with PS.

signal outside of the irradiation field is higher for the rectangular scintillators (2R and 5R) than the square scintillators (2S and 5S) and is even lower for the etched scintillator.

Figure 6.4 shows the profiles of each scintillator geometry placed on top of the SPSD array for field sizes of $0.5 \times 0.5 \text{ cm}^2$, $1 \times 1 \text{ cm}^2$, and $2 \times 2 \text{ cm}^2$. The signal is normalized to the maximum signal measured for each array. Our data are compared to film measurements. Close to the center of the field each SPSD array matches film fairly well. However, as you move further from the normalization point

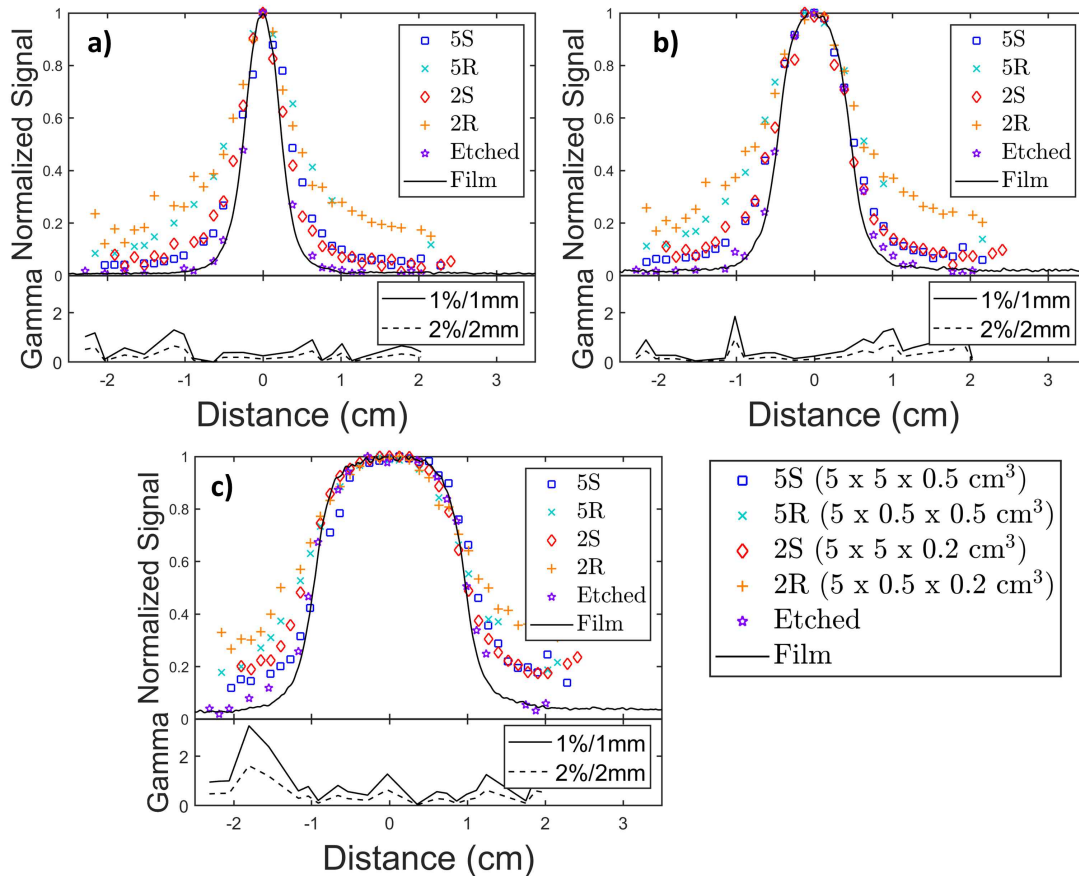


Figure 6.4: The signal is normalized to the center pixel for each data point is plotted for field sizes of a) $0.5 \times 0.5 \text{ cm}^2$ b) $1 \times 1 \text{ cm}^2$ and c) $2 \times 2 \text{ cm}^2$. The abbreviations in the legend stands for 5S ($5 \times 5 \times 0.5 \text{ cm}^3$), 5R ($5 \times 0.5 \times 0.5 \text{ cm}^3$), 2S ($5 \times 5 \times 0.2 \text{ cm}^3$), 2R ($5 \times 0.5 \times 0.2 \text{ cm}^3$), etched ($5 \times 0.5 \times 0.5 \text{ cm}^3$ with septa), and film (EBT3) which is shown for comparison. Gamma values calculated using the etched scintillator data in comparison to the film is shown under each profile.

towards the periphery many of the arrays see an over-response in signal in comparison to film data. The rectangular scintillators (2R and 5R) have more error outside the field than the square scintillators (2S and 5S). The etched scintillator design matches the film data well, even outside of the field. Below each profile is a gamma analysis comparing the etched scintillator data to the film data, indicating the level of agreement.

Figure 6.5 shows the output factors measured with the SPSSD array for each

scintillator geometry. For field sizes of $5 \times 5 \text{ cm}^2$ and larger, all scintillator geometries match ion chamber measurements well, with a maximum deviation of 1.6 % observed for the 5R scintillator geometry at a field size of $6 \times 6 \text{ cm}^2$. However, as shown in figure 6.5b at fields below $5 \times 5 \text{ cm}^2$ (corresponding to the length of the array) there begins to be an under-response for some scintillator geometries. The etched scintillator shows agreement to within 1.2 % down to a field size of $1 \times 1 \text{ cm}^2$. For the $0.5 \times 0.5 \text{ cm}^2$ field size, the etched scintillator measures an output factor that is 23 % lower than the microDiamond detector and 24 % less than film. For the rectangular and square scintillators the error in the output factors measured increased as the field size decreased below $5 \times 5 \text{ cm}^2$ field size. At a $4 \times 4 \text{ cm}^2$ field size there is a measured under-response of 0.6 %, 8.3 %, 0.8 %, and 9.7 % for the 2R, 2S, 5R, and 5S scintillator geometries, respectively. At $1 \times 1 \text{ cm}^2$ that discrepancy increased to 33 %, 52 %, 39 %, and 54 % for the 2R, 2S, 5R, and 5S scintillator geometries, respectively. The rectangular geometries performed better than the square geometries.

6.6 Discussion

In this work a novel radiation detector (SPSD array) was fabricated by coupling an array of organic photodiodes to scintillators with five different geometries. This detector system maintains the benefits of plastic scintillators, but are readout with a simple electrometer connection opposed to a colour filtration and correction method required for fiber-based systems. The initial application of the system studied in this work is aimed at output factors and profile measurements, and promising results have been reported here.

In figure 6.2 the charge collected for each pixel of the PSD array is given for a field size of $10 \times 10 \text{ cm}^2$. The PSD arrays with thicker scintillators produce larger signals as expected, and for a given scintillator thickness, larger scintillator

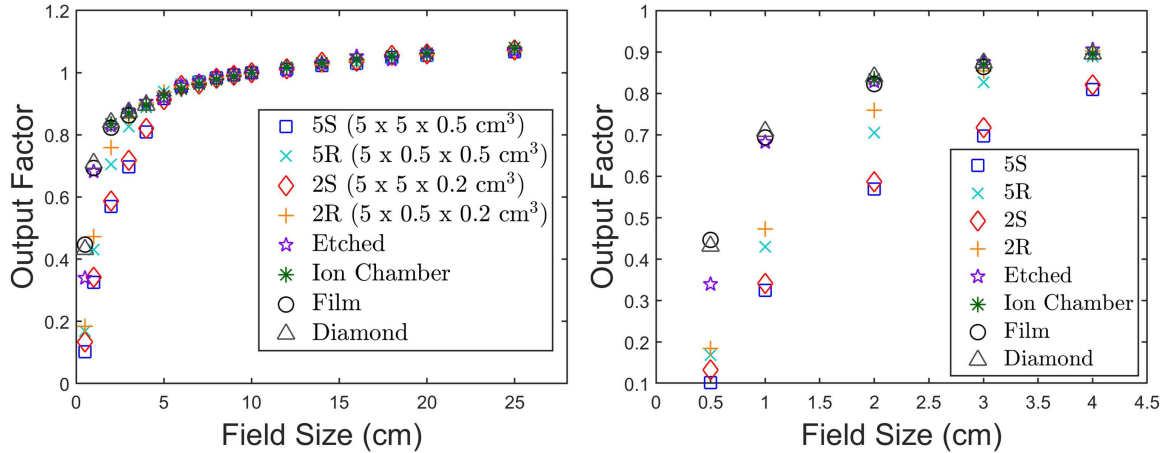


Figure 6.5: Output factors are plotted for field sizes ranging from $0.5 \times 0.5 \text{ cm}^2$ to $25 \times 25 \text{ cm}^2$ on the left and $0.5 \times 0.5 \text{ cm}^2$ to $4 \times 4 \text{ cm}^2$ on the right. The geometry of the scintillators are indicated in the legend. 5S ($5 \times 5 \times 0.5 \text{ cm}^3$), 5R ($5 \times 0.5 \times 0.5 \text{ cm}^3$), 2S ($5 \times 5 \times 0.2 \text{ cm}^3$), 2R ($5 \times 0.5 \times 0.2 \text{ cm}^3$), etched ($5 \times 0.5 \times 0.5 \text{ cm}^3$ with septa), ion chamber (A12 for $4 \times 4 \text{ cm}^2$ to $25 \times 25 \text{ cm}^2$ and a semiflex 31010 micro ion chamber for smaller field sizes), film (EBT3), and Diamond (PTW 60019 microDiamond) shown for comparison.

area results in larger detected signal, indicating that optical diffusion contributes significantly to the measured signal. When the scintillator is etched the charge collected decreases substantially due to the reduction of cross-talk. The variability between devices on a given array could be attributable to differences of photodiode efficiency and the quality of the interface between the scintillator and glass (polishing differences). The increase in variability for the etched scintillator design could be due to the decreased signal and differences of the size of the scintillator over each photodiode due to the variation in septa width.

Figure 6.3 shows the charge collected by each pixel for each geometry for each of three field sizes. The SPSD array with the rectangular scintillator geometries (2R and 5R) exhibit higher charge collection outside the field than the square scintillator geometries (2S and 5S). This may be due to light piping (i.e. light created near the center will reflect off the sides of the rectangular scintillator and be absorbed in the photodiodes further down the scintillator). The light created in the

center of the square scintillators can more easily travel laterally and not be detected by the photodiodes near the edge of the array. The charge collected near the center of the field reduces by factors of 5.1, 7.1, and 10.5 for the etched scintillator in comparison to the 5S scintillator for field sizes of $0.5 \times 0.5 \text{ cm}^2$, $1 \times 1 \text{ cm}^2$, and $2 \times 2 \text{ cm}^2$, respectively. This reduction of signal can be attributed to the decrease of cross-talk when etching the scintillator. It is more significant at larger field sizes because it is cutting off more light from the surrounding scintillator.

The photodiode makes up roughly 4.1 %, 6.1 %, and 9.3 % of the signal at the center of the field when compared to the SPSD array with the etched scintillator for field sizes of $0.5 \times 0.5 \text{ cm}^2$, $1 \times 1 \text{ cm}^2$, and $2 \times 2 \text{ cm}^2$, respectively. The PS makes up 1.5 %, 1.8 %, and 2.1 % of the SPSD array with the etched scintillator for field sizes of $0.5 \times 0.5 \text{ cm}^2$, $1 \times 1 \text{ cm}^2$, and $2 \times 2 \text{ cm}^2$, respectively. The contribution of the PS device indicates with an improved wiring footprint the signal contributed due to non-scintillation light could be decreased. To increase the sensitivity of the etched scintillator a reflective coating could be used in the septa for better light collection, leading to higher SNR. Furthermore, the design of the pixels could be optimized (current active area $1 \times 4 \text{ mm}^2$).

Small field profiles of the SPSD array are compared to film measurements in figure 6.4. The SPSD array with the rectangular scintillators demonstrate worse agreement outside of the primary field in comparison to the square scintillator which is likely due to light piping as explained earlier. In contrast, output factors measured with the rectangular scintillator show better agreement with ion chamber measurements compared to the square scintillators (figure 6.5). Elimination of signal from the lower dose regions of the field adjacent to the photodiode array in the rectangular scintillator geometry reduces the volume averaging effects of small fields leading to better agreement with the A12, PTW 60019 microDiamond, and semi-flex 31010 detectors (over the detector-appropriate field size ranges). The non-etched

scintillators saw an error in output factors as the field size decreased below $5 \times 5 \text{ cm}^2$ which corresponds to the lateral dimensions of the scintillator. Since the reference field size for output factors was chosen as $10 \times 10 \text{ cm}^2$ (i.e. the full scintillator was irradiated), contaminant signal (i.e. diffused optical photons) from all areas of the scintillator not directly above the central photodiode could contribute to this reference signal. Once the field sizes dropped below the size of the scintillator, some of this contaminant signal was no longer present, resulting in an underestimate of the output factor.

The SPSD array with the etched scintillator design performed well for small field profiles and output factors. All output factors were within 1.2 % of commercial detectors down to a field size of $1 \times 1 \text{ cm}^2$ (figure 6.5). The excellent agreement was achieved without being daisy-chained to a reference detector, which is required for the microDiamond and micro-ion chamber detectors, and highlights the versatility of our SPSD array. However, the deviation at the $0.5 \times 0.5 \text{ cm}^2$ field size was more significant. The difference at the smallest field size is likely due to volume averaging. The active area of the photodiode was approximately $1 \times 4 \text{ mm}^2$. A reduction in the lateral dimension of the photodiode could reduce the partial volume affect, but would result in a reduction of signal. Use of a reflective coating as a septal material could potentially compensate for this signal loss.

Small field measurements are some of the most challenging in a radiation therapy setting due to source occlusion, detector perturbations, requirements for corrections, etc. The consequences of not making the measurements accurately can be very serious [110] [111]. We have demonstrated that the SPSD array is capable of accurate measurements of both profiles and output factors. This novel detector

has potential as a high resolution detector for small fields, which could include post-commissioning QA, patient specific treatment verifications, and any other QA measurements. In the future we will create a 2D array to allow planar dose measurements. As we have reported here, the array would also be capable of simultaneous acquisition of small field profiles and output factors.

6.7 Conclusion

A novel array detector was fabricated by coupling an organic photodiode array to an organic scintillator. Scintillator geometries included four different sizes of bulk scintillator over the array and an etched scintillator was used to decrease cross-talk. In comparison to a $5 \times 5 \times 0.5 \text{ cm}^3$ bulk scintillator, the sensitivities of the etched scintillator were 5.1, 7.1, and 10.5 times less for field sizes $0.5 \times 0.5 \text{ cm}^2$, $1 \times 1 \text{ cm}^2$, and $2 \times 2 \text{ cm}^2$, respectively. Small field profiles were compared to film measurements and the etched scintillator performed very well. Furthermore, the etched scintillator measured output factors within 1.2 % of commercial detectors (ion chambers, film, and diamond) down to a field size of $1 \times 1 \text{ cm}^2$. At the smallest field size ($0.5 \times 0.5 \text{ cm}^2$) there was a significant deviation in the output factor which is likely due to volume averaging (active area of the photodiode was approximately $1 \times 4 \text{ mm}^2$), but could be reduced in the future. In the future this work could be extended to a 2D array capable of measuring output factors and profiles of small fields simultaneously.

6.8 Acknowledgements

This work was supported in part by a natural sciences and engineering research council of Canada (NSERC) Discovery Grant and NSERC postgraduate scholarship-doctoral (PGS-D).

Chapter 7

Conclusion

7.1 Summary

The purpose of this thesis was to develop a scintillator detector system that does not require an optical fiber. The elimination of the optical fiber decreases the Cerenkov radiation contributing to the signal which is the main source of error for plastic scintillation-based detectors. The detector developed in this work collects the light locally by placing an organic photodiode against the scintillator. The first and second manuscripts explored the response of the organic photodiodes when irradiated with photon beams (chapters 3 and 4). The thinnest photodiodes had a measurable, but small response, which was encouraging for their use in this detector, where the desired signal was due to the collection of light emitted by a scintillator. The third manuscript coupled an organic scintillator to the photodiode to create a single element SPSD, which demonstrated excellent performance for various clinical measurements. In the fourth manuscript a 1D array was fabricated by coupling an array of photodiodes to an organic scintillator to measure the emitted light. Small field profiles and output factors were measured which showed excellent agreement with film and micro ion chamber measurements. The detector system has potential as a novel clinical dosimetry system for use in simultaneously measuring output factors and profiles of small field.

The first manuscript set out to fabricate and characterize the response of a P3HT/PCBM bulk heterojunction organic photodiode with respect to total dose,

energy, and dose rate. The measured signal was corrected by subtracting the measured current of a device made with a PS layer in place of the BHJ layer. This method allowed the differentiation between irradiation induced photocurrent and extraneous signal and is described in detail in manuscript 2. Output factors were within 2% of ion chamber measurements indicating that the stem effect was effectively corrected. The sensitivity measured for a 100 nm thick device was 2.3 pC/cGy. By increasing the thickness to approximately 420 nm the sensitivity improved to 6.7 pC/cGy. The photocurrents measured increased linearly with dose rate which is encouraging for radiation sensing applications. The low sensitivity of the photodiodes made them ideal for coupling to scintillators as shown in manuscripts 3 and 4. The SPSD detector requires the diode to be placed within the beam and the desired signal is due to the collection of light emitted by the scintillator and not direct irradiation beam interaction in the diode itself.

The second manuscript gives a detailed description of the methods used in the first manuscript. A novel technique to differentiate the radiation-induced photocurrent created in the photodiode from the Compton current created in the wires, electrodes etc. was presented. This technique used a dielectric (polystyrene) layer between the electrodes in place of the semiconductor needed for the diode. Therefore, this device would not allow photocurrent to flow through it, but with the same irradiation conditions as the diode (dose rate, field size, etc.) would measure the same Compton current. The Compton current was highly dependent on field size. Compton current makes up 11 % of the signal for a 3 x 3 cm² field size and rising to over 60 % of the signal for a 20 x 20 cm² field size. The increase proportion of Compton signal is due to the larger volume of wires directly in the beam.

After implementing the correction technique, the output factors agreed with ion chamber measurements. Furthermore, after correction the current measured from the two electrodes demonstrated the expected photodiode behavior (opposite

directions and of equal magnitude), giving further evidence of the efficacy of our correction method.

The third manuscript described the fabrication and characterization of a stemless plastic scintillation detector. The detector was fabricated by coupling the organic photodiode characterized in manuscripts 1 and 2 to a polished organic scintillator. The SPSDs exhibited excellent linearity, no significant dose per pulse dependence, and an increase response with energy in the kV range that is comparable to previously published PSD data. The sensitivities of the small scintillator ($\sim 3 \times 3 \times 2 \text{ mm}^3$) and large scintillator ($\sim 5 \times 5 \times 5 \text{ mm}^3$) SPSDs were $0.10 - 0.14 \text{ nC/cGy}$ and $1.00 - 1.07 \text{ nC/cGy}$, respectively. Furthermore, the SPSDs were used to measure PDDs and output factors which compared favourably with ion chamber measurements. This single element detector could be used for various clinical measurements such as output factors, PDDs, or possibly as an in vivo dosimeter.

The fourth manuscript took the detector fabricated in manuscript 3 and extended it to create a 1D array of detectors. The array was used to measure small field profiles and the central detector measured output factors. The response of the detector was compared to commercial detectors such as EBT3 film, ion chambers (Exradin A12 and semiflex 31010 micro ion chamber depending on field size), and a PTW microDiamond detector. The non-etched scintillator array measured the signal outside of the field that was erroneously high due to cross-talk (i.e. light produced within the irradiation beam in the scintillator is absorbed by photodiodes outside the field). The cross-talk was significantly reduced by segmenting the scintillator with a laser etcher and depositing black paint into the voids. The etched design measured small field profiles that agreed well with film measurements. Output factors agreed to within 1.2 % of ion chambers, microDiamond, and film for field sizes $1 \times 1 \text{ cm}^2$ to $25 \times 25 \text{ cm}^2$. At a field size of $0.5 \times 0.5 \text{ cm}^2$ there was significant

difference from the film and diamond measurements, likely due to volume averaging. The active area of the photodiode was approximately $1 \times 4 \text{ mm}^2$. Reducing the lateral dimension could reduce the partial volume effect.

7.2 Future Work

More work is needed with this detector array to allow it to transition to a commercial product. The device would benefit from a better readout system, should be designed to minimize the footprint of the wiring, and the readout circuitry could be expanded to include an array of organic TFTs to facilitate individual addressing of devices in a 2D array of detectors.

Currently, the readout of the diode array must be performed one device at a time. A commercial array detector will need to allow the entire array to be readout simultaneously. Detector arrays of this nature are already used clinically. The lessons learned from the design of those arrays could aid in the implementation of an array detector based on this novel detector. Similarly, minimizing the footprint of the wiring in the beam has also been investigated for other array detector designs. If the signal from the wiring is significant then the stem effect in our detector may be as detrimental as Cerenkov produced in a PSD measured with an optical fiber (stem effect) and thus our design offers less benefit over the current product.

Future work will aim to create a 2D array of detectors. The design of the array will have to consider the size of each pixel. Smaller pixels will lead to lower signal, but improved spatial resolution. The optimal design of the array will likely be dependent on the application. A high resolution array might be appropriate for SRS field characterization, but a sparser array over a large area could be more appropriate for larger treatment sites. The sensitivity of these detectors could first be optimized to allow smaller pixel dimensions. The most significant improvement could come from placing a reflective coating around the scintillator and in the septa

for better light piping into the photodiode. Other ways to increase the sensitivity is to optimize the photodiode efficiency (spin-coating speed, semiconductor concentrations, annealing temperature, etc.), choose scintillator emission spectra that best overlap with the absorption spectrum of the photodiodes, and reduce the thickness of the glass substrate (or use a different thin substrate such as PET), which reduces the distance the light can diverge before being absorbed in the photodiode [70, 93]. Similar to before the exact layout of the array could draw from lessons learned with the design of other commercial products.

We have eliminated the optical fiber required for a standard readout of a scintillator-based detector, which transports the light signal to a distant optical detector (e.g. the Exradin W1 and W2 are commercial products that use an optical fiber). Eliminating the optical fiber should reduce the Cerenkov radiation. However, there could still be Cerenkov radiation contributing to the measured signal due to Cerenkov created in the scintillator itself [54]. The excellent agreement between our detectors to commercial detectors over a variety of irradiation setups presented throughout this work suggest that if Cerenkov is present, it is not problematic in the instances investigated. However, this phenomenon should be kept in mind for future work as there may be situations that Cerenkov could be significant, leading to an error. An investigation may be necessary to properly quantify the Cerenkov and the error that could result from it. It may be possible to do a correction using organic photodiodes with different absorption spectra and perform a chromatic removal technique. If Cerenkov radiation is collected efficiently (i.e. regardless of the direction of emission) then it can become part of the signal. So another possible solution as shown with the single-element SPSD presented in chapter 5, is simply placing reflective tape around the scintillator, which eliminated the directional dependence to 16 MeV electrons.

Future work should investigate the use of the array detector for patient specific dose verifications.

Other avenues of this research include making an energy independent detector, optimizing a photodiode as a direct detector, and using other properties of organic electronics for detectors (organic thin film transistors, flexible detector array, etc.). In chapter 3 we showed that a photodiode detector's response decreases with energy in the kV range. In chapter 5 we showed that when coupling an organic scintillator the opposite trend is observed. One thing to keep in mind about the energy dependence is that the orthovoltage unit and linac have vastly different dose rates, which may be contributing to the different response. By creating a detector that has significant contribution due to both the irradiation induced photocurrent in the diode and light absorption from the scintillator, a detector could be made to optimize the energy response. Another possible improvement is to make all components of the photodiode out of materials more water-equivalent. This includes using conducting organics for the electrodes and a plastic substrate (PET or PEN) instead of glass, which would have the additional benefit of being flexible. Another possible improvement is to use a scintillator with better energy dependence. A couple groups have introduced dopants into the scintillators, which reduced the energy dependence [48, 112].

Manuscripts 1 and 2 showed that an organic photodiode could be used as a direct detector. Although we showed that the sensitivity was low, it was similar to some commercially available detectors. Furthermore, we showed the sensitivity could be increased by increasing the thickness of the sensitive layer. We selected the thin photodiode to use for the SPSD in part to minimize the contribution from the diode to the signal. In other work from our group we showed that by applying a bias the sensitivity could be increased [113]. A photodiode direct detector could have the advantages of a very small active volume and being able to be fabricated

on a flexible substrate.

7.3 Conclusions

The research in this thesis shows the steps taken to fabricate a novel one-dimensional array of SPSDs. The detector has the recognized benefits of scintillation detectors (tissue equivalence, minimal field perturbation) without the need for a complex optical processing for Cerenkov radiation correction. We showed a single element device had excellent linearity with dose, no dose per pulse dependence, and energy dependence comparable to a PSD measured using an optical fiber. Furthermore, the detector array showed excellent agreement with other commercial detectors (ion chambers, film) for small field applications. This detector could be used for the simultaneous acquisition of output factors and profiles of small radiation fields.

Bibliography

- [1] K. D. Miller, R. L. Siegel, C. C. Lin, A. B. Mariotto, J. L. Kramer, J. H. Rowland, K. D. Stein, R. Alteri, and A. Jemal, “Cancer treatment and survivorship statistics, 2016,” *CA: A Cancer Journal for Clinicians*, vol. 66, no. 4, pp. 271–289, 2016.
- [2] G. A. J. Hall Eric J., “Radiobiology for the radiologist,” 2012.
- [3] F. H. Attix, *Introduction to radiological physics and radiation dosimetry*. John Wiley & Sons, 2008.
- [4] “NIST XCOM: Element/Compound/Mixture.”
- [5] A. E. Nahum, *Cavity Theory, Stopping-Power Ratios, Correction Factors*, vol. 34. 2009.
- [6] H. Palmans, P. Andreo, M. S. Huq, J. Seuntjens, K. E. Christaki, and A. Meghzifene, “Dosimetry of small static fields used in external photon beam radiotherapy: Summary of TRS-483, the IAEA–AAPM international Code of Practice for reference and relative dose determination,” *Medical Physics*, vol. 45, pp. e1123–e1145, nov 2018.
- [7] H. Johns and J. Cunningham, “THE PHYSICS OF RADIOLOGY FOURTH EDITION,” tech. rep., 1983.
- [8] “NIST ESTAR.”
- [9] A. McNair, “ICRU Report 33 - Radiation Quantities and Units Pub: International Commission on Radiation Units and Measurements, Washington D.C. USA issued 15 April 1980, pp.25,” *Journal of Labelled Compounds and Radiopharmaceuticals*, vol. 18, pp. 1398–1398, sep 1981.
- [10] N. Fatima, A. Meola, V. Y. Ding, E. Pollom, S. G. Soltys, C. F. Chuang, N. Shahsavari, S. L. Hancock, I. C. Gibbs, J. R. Adler, and S. D. Chang, “The Stanford stereotactic radiosurgery experience on 7000 patients over 2 decades (1999–2018): looking far beyond the scalpel,” *Journal of Neurosurgery*, vol. -1, pp. 1–17, apr 2021.
- [11] J. A. Halpern, A. Sedrakyan, W. C. Hsu, J. Mao, T. J. Daskivich, P. L. Nguyen, E. B. Golden, J. Kang, and J. C. Hu, “Use, complications, and costs of stereotactic body radiotherapy for localized prostate cancer,” *Cancer*, vol. 122, pp. 2496–2504, aug 2016.

- [12] W. L. Ong, S. Siva, R. L. Milne, F. Foroudi, and J. L. Millar, “Trend in stereotactic radiation therapy use for management of bone and brain metastases in patients with renal cell carcinoma in Australia,” *The Oncologist*, apr 2021.
- [13] B. Sidiqi, N. Sheth, A. Lee, J. Safdieh, and D. Schreiber, “Patterns of stereotactic radiotherapy utilization and fractionation for acoustic neuroma in the United States,” *Journal of radiosurgery and SBRT*, vol. 5, no. 3, pp. 201–207, 2018.
- [14] J. M. Stahl, C. D. Corso, V. Verma, H. S. Park, S. K. Nath, Z. A. Husain, C. B. Simone, A. W. Kim, and R. H. Decker, “Trends in stereotactic body radiation therapy for stage I small cell lung cancer,” *Lung Cancer*, vol. 103, pp. 11–16, jan 2017.
- [15] F. Sánchez-Doblado, G. H. Hartmann, J. Pena, J. V. Roselló, G. Russiello, and D. M. Gonzalez-Castaño, “A new method for output factor determination in MLC shaped narrow beams,” *Physica Medica*, vol. 23, pp. 58–66, jun 2007.
- [16] S. Derreumaux, C. Etard, C. Huet, F. Trompier, I. Clairand, J.-F. Bottollier-Depois, B. Aubert, and P. Gourmelon, “Lessons from recent accidents in radiation therapy in France,” *Radiation Protection Dosimetry*, vol. 131, pp. 130–135, aug 2008.
- [17] W. Bogdanich and R. R. Ruiz, “Radiation Errors Reported in Missouri,” tech. rep., 2010.
- [18] M. Aspradakis, J. Byrne, H. Palmans, S. Duane, J. Conway, A. Warrington, and K. Rosser, “IPEM report 103: Small field MV photon dosimetry,” 2010.
- [19] K. Eklund and A. Ahnesjö, “Physics in Medicine & Biology To cite this article: Karin Eklund and Anders Ahnesjö,” *Phys. Med. Biol.*, vol. 55, p. 7411, dec 2010.
- [20] C. Martens, C. De Wagter, and W. De Neve, “The value of the PinPoint ion chamber for characterization of small field segments used in intensity-modulated radiotherapy,” *Physics in Medicine and Biology*, vol. 45, pp. 2519–2530, sep 2000.
- [21] B. R. Muir and D. W. O. Rogers, “The central electrode correction factor for high-Z electrodes in small ionization chambers,” *Medical Physics*, vol. 38, pp. 1081–1088, jan 2011.
- [22] O. A. Sauer and J. Wilbert, “Measurement of output factors for small photon beams,” *Medical Physics*, vol. 34, pp. 1983–1988, jun 2007.

- [23] L. A. DeWerd, S. D. Davis, L. J. Bartol, and F. Grenzow, "Ionization chamber instrumentation," *Clinical Dosimetry Measurements in Radiotherapy*, edited by DWO Rogers and JE Cygler (Medical Physics Publishing, Madison, Wisconsin, 2009), 2009.
- [24] C. M. Ma, "AAPM TG-61 report on kilovoltage x-ray dosimetry: Formalisms and applications," in *Annual International Conference of the IEEE Engineering in Medicine and Biology - Proceedings*, vol. 3, pp. 2308–2312, 2000.
- [25] C. G. Soares, S. Trichter, and S. Devic, "Radiochromic film," *Textbook of AAPM Summer School*, 2009.
- [26] G. Massillon-JL, S.-T. Chiu-Tsao, I. Domingo-Munoz, and M. F. Chan, "Energy Dependence of the New Gafchromic EBT3 Film:Dose Response Curves for 50 KV, 6 and 15 MV X-Ray Beams," *International Journal of Medical Physics, Clinical Engineering and Radiation Oncology*, vol. 01, pp. 60–65, aug 2012.
- [27] A. Rink, D. F. Lewis, S. Varma, I. A. Vitkin, and D. A. Jaffray, "Temperature and hydration effects on absorbance spectra and radiation sensitivity of a radiochromic medium," *Medical Physics*, vol. 35, pp. 4545–4555, sep 2008.
- [28] B. Hartmann, M. Martišíková, and O. Jäkel, "Technical Note: Homogeneity of Gafchromic [®] EBT2 film," *Medical Physics*, vol. 37, pp. 1753–1756, mar 2010.
- [29] H. Bouchard, F. Lacroix, G. Beaudoin, J. Carrier, and I. Kawrakow, "On the characterization and uncertainty analysis of radiochromic film dosimetry," *Medical physics*, vol. 36, no. 6, pp. 1931–1946, 2009.
- [30] T. C. Zhu, A. S. Saini, and J. E. Cygler, "Diode dosimetry for megavoltage electron and photon beams," *Clinical Dosimetry Measurements in Radiotherapy*, no. 34, pp. 913–939, 2009.
- [31] A. S. Saini and T. C. Zhu, "Energy dependence of commercially available diode detectors for in-vivo dosimetry," *Medical physics*, vol. 34, no. 5, pp. 1704–1711, 2007.
- [32] D. Wilkins, X. A. Li, J. Cygler, and L. Gerig, "The effect of dose rate dependence of p-type silicon detectors on linac relative dosimetry," *Medical physics*, vol. 24, no. 6, pp. 879–881, 1997.
- [33] K. T. Welsh and L. E. Reinstein, "The thermal characteristics of different diodes on in vivo patient dosimetry," *Medical physics*, vol. 28, no. 5, pp. 844–849, 2001.

- [34] J. V. Dam, G. Leunens, and A. Dutreix, "Correlation between temperature and dose rate dependence of semiconductor response; influence of accumulated dose," *Radiotherapy and Oncology*, vol. 19, no. 4, pp. 345–351, 1990.
- [35] J. M. Lárraga-Gutiérrez, P. Ballesteros-Zebadúa, M. Rodríguez-Ponce, O. A. García-Garduño, and O. O. G. de la Cruz, "Properties of a commercial PTW-60019 synthetic diamond detector for the dosimetry of small radiotherapy beams," *Physics in Medicine and Biology*, vol. 60, pp. 905–924, jan 2015.
- [36] S. Beddar and L. Beaulieu, *Scintillation dosimetry*. CRC Press, 2016.
- [37] J. E. Cygler and P. Scalchi, "MOSFET dosimetry in radiotherapy," *Clinical Dosimetry Measurements in Radiotherapy*, no. 34, pp. 941–977, 2009.
- [38] C. R. Edwards, S. Green, J. E. Palethorpe, and P. J. Mountford, "The response of a MOSFET, p-type semiconductor and LiF TLD to quasi-monoenergetic x-rays," *Physics in Medicine and Biology*, vol. 42, no. 12, p. 2383, 1997.
- [39] G. P. Beyer, G. G. Mann, J. A. Pursley, E. T. Espenhahn, C. Fraisse, D. J. Godfrey, M. Oldham, T. B. Carrea, N. Bolick, and C. W. Scarantino, "An implantable MOSFET dosimeter for the measurement of radiation dose in tissue during cancer therapy," *IEEE Sensors Journal*, vol. 8, no. 1, pp. 38–51, 2008.
- [40] N. Jornet, P. Carrasco, D. Jurado, A. Ruiz, T. Eudaldo, and M. Ribas, "Comparison study of MOSFET detectors and diodes for entrance in vivo dosimetry in 18 MV x-ray beams," *Medical physics*, vol. 31, no. 9, pp. 2534–2542, 2004.
- [41] L. A. DeWerd, L. J. Bartol, and S. D. Davis, "Thermoluminescence dosimetry," *Clinical Dosimetry Measurements in Radiotherapy. Madison WI: Medical Physics Publishing*, 2009.
- [42] S. McKeever, *Thermoluminescence of solids*. 1988.
- [43] A. A. Nunn, S. D. Davis, J. A. Micka, and L. A. DeWerd, "LiF: Mg, Ti TLD response as a function of photon energy for moderately filtered x-ray spectra in the range of 20–250 kVp relative to C60o," *Medical physics*, vol. 35, no. 5, pp. 1859–1869, 2008.
- [44] J. J. Wood and W. P. Mayles, "Factors affecting the precision of TLD dose measurements using an automatic TLD reader," *Physics in Medicine and Biology*, vol. 40, no. 2, pp. 309–313, 1995.
- [45] P. A. Jursinic, "Characterization of optically stimulated luminescent dosimeters, OSLDs, for clinical dosimetric measurements," *Medical Physics*, vol. 34, pp. 4594–4604, nov 2007.

- [46] A. A. Omotayo, J. E. Cygler, and G. O. Sawakuchi, "The effect of different bleaching wavelengths on the sensitivity of Al₂O₃:C optically stimulated luminescence detectors (OSLDs) exposed to 6 MV photon beams," *Medical Physics*, vol. 39, pp. 5457–5468, aug 2012.
- [47] A. S. Beddar, T. R. Mackie, and F. H. Attix, "Water-equivalent plastic scintillation detectors for high-energy beam dosimetry: I. Physical characteristics and theoretical considerations," *Physics in Medicine & Biology*, vol. 37, no. 10, p. 1883, 1992.
- [48] J. F. Williamson, J. F. Dempsey, A. S. Kirov, J. I. Monroe, W. R. Binns, and H. Hedtj rn, "Plastic scintillator response to low-energy photons," *Physics in Medicine and Biology*, vol. 44, pp. 857–871, apr 1999.
- [49] G. Knoll, *Radiation detection and measurement*. John Wiley and Sons, 2010.
- [50] J. B. Birks, "Scintillations from organic crystals: Specific fluorescence and relative response to different radiations," *Proceedings of the Physical Society. Section A*, vol. 64, pp. 874–877, oct 1951.
- [51] J. I. Hopkins, "Electron Energy Studies with the Anthracene Scintillation Counter," *Review of Scientific Instruments*, vol. 22, no. 1, pp. 29–33, 1951.
- [52] A. M. Frelin, J. M. Fontbonne, G. Ban, J. Colin, and M. Labalme, "Comparative Study of Plastic Scintillators for Dosimetric Applications," *IEEE Transactions on Nuclear Science*, vol. 55, no. 5, pp. 2749–2756, 2008.
- [53] L. Beaulieu and S. Beddar, "Review of plastic and liquid scintillation dosimetry for photon, electron, and proton therapy," *Physics in Medicine & Biology*, vol. 61, no. 20, p. R305, 2016.
- [54] T. T. Monajemi and E. A. Ruiz, "Application of plastic scintillating fibres to surface dosimetry in megavoltage photon and electron beams: considerations for Cerenkov correction," *Physics in Medicine & Biology*, vol. 63, no. 18, p. 185003, 2018.
- [55] L. Archambault, A. S. Beddar, L. Gingras, R. Roy, and L. Beaulieu, "Measurement accuracy and Cerenkov removal for high performance, high spatial resolution scintillation dosimetry," *Medical physics*, vol. 33, no. 1, pp. 128–135, 2006.
- [56] S. F. D. Boer, A. S. Beddar, and J. A. Rawlinson, "Optical filtering and spectral measurements of radiation-induced light in plastic scintillation dosimetry," *Physics in Medicine & Biology*, vol. 38, no. 7, p. 945, 1993.
- [57] A. S. Beddar, T. R. Mackie, and F. H. Attix, "Water-equivalent plastic scintillation detectors for high-energy beam dosimetry: II. Properties and measurements," *Physics in Medicine & Biology*, vol. 37, no. 10, p. 1901, 1992.

- [58] F. Therriault-Proulx, S. Beddar, and L. Beaulieu, “On the use of a single-fiber multipoint plastic scintillation detector for ^{192}Ir high-dose-rate brachytherapy,” *Medical physics*, vol. 40, no. 6Part1, 2013.
- [59] O. Ostroverkhova, *Handbook of Organic Materials for Electronic and Photonic Devices*. 2018.
- [60] P. E. Shaw, A. Ruseckas, and I. D. W. Samuel, “Exciton diffusion measurements in poly (3-hexylthiophene),” *Advanced Materials*, vol. 20, no. 18, pp. 3516–3520, 2008.
- [61] W.-H. Baek, H. Yang, T.-S. Yoon, C. J. Kang, H. H. Lee, and Y.-S. Kim, “Effect of P3HT: PCBM concentration in solvent on performances of organic solar cells,” *Solar Energy Materials and Solar Cells*, vol. 93, no. 8, pp. 1263–1267, 2009.
- [62] M. T. Dang, G. Wantz, H. Bejbouji, M. Urien, O. J. Dautel, L. Vignau, and L. Hirsch, “Polymeric solar cells based on P3HT: PCBM: Role of the casting solvent,” *Solar Energy Materials and Solar Cells*, vol. 95, no. 12, pp. 3408–3418, 2011.
- [63] B. Watts, W. J. Belcher, L. Thomsen, H. Ade, and P. C. Dastoor, “A quantitative study of PCBM diffusion during annealing of P3HT: PCBM blend films,” *Macromolecules*, vol. 42, no. 21, pp. 8392–8397, 2009.
- [64] B. Liu, R. Q. Png, L. H. Zhao, L. L. Chua, R. H. Friend, and P. K. Ho, “High internal quantum efficiency in fullerene solar cells based on crosslinked polymer donor networks,” *Nature Communications*, vol. 3, pp. 1–8, dec 2012.
- [65] B. Peng, X. Guo, Y. Zou, C. Pan, and Y. Li, “Performance improvement of annealing-free P3HT : PCBM-based polymer solar cells via 3-methylthiophene additive,” *Journal of Physics D: Applied Physics*, vol. 44, sep 2011.
- [66] M. A. Hupman, I. Valitova, I. G. Hill, and A. Syme, “Radiation induced photocurrent in the active volume of P3HT/PCBM BHJ photodiodes,” *Organic Electronics*, vol. 85, p. 105890, oct 2020.
- [67] M. A. Hupman, I. Valitova, I. G. Hill, and A. Syme, “Method for the differentiation of radiation-induced photocurrent from total measured current in P3HT/PCBM BHJ photodiodes,” *MethodsX*, vol. 7, p. 101125, jan 2020.
- [68] M. A. Hupman, T. Monajemi, I. Valitova, I. G. Hill, and A. Syme, “Fabrication and characterization of a stemless plastic scintillation detector,” *Medical Physics*, vol. 47, pp. 5882–5889, nov 2020.
- [69] D. B. Hall, P. Underhill, and J. M. Torkelson, “Spin coating of thin and ultrathin polymer films,” *Polymer Engineering & Science*, vol. 38, no. 12, pp. 2039–2045, 1998.

- [70] B. T. de Villers, C. J. Tassone, S. H. Tolbert, and B. J. Schwartz, "Improving the Reproducibility of P3HT:PCBM Solar Cells by Controlling the PCB-M/Cathode Interface," *Journal of Physical Chemistry C*, vol. 113, no. 44, pp. 18978–18982, 2009.
- [71] D. M. Mattox, *Handbook of physical vapor deposition (PVD) processing*. William Andrew, 2010.
- [72] S. Tanny, S. Holmes, N. Sperling, and E. I. Parsai, "Technical note: Influence of Compton currents on profile measurements in small-volume ion chambers," *Medical Physics*, vol. 42, pp. 5768–5772, oct 2015.
- [73] R. R. Mayer, F. Ma, Y. Chen, R. I. Miller, A. Belard, J. McDonough, and J. J. O'Connell, "Enhanced dosimetry procedures and assessment for EBT2 radiochromic film," *Medical Physics*, vol. 39, pp. 2147–2155, mar 2012.
- [74] C. W. Tang and S. A. VanSlyke, "Organic electroluminescent diodes," *Applied Physics Letters*, vol. 51, no. 12, pp. 913–915, 1987.
- [75] C. D. Dimitrakopoulos and P. R. L. Malenfant, "Organic thin film transistors for large area electronics," *Advanced Materials*, vol. 14, no. 2, pp. 99–117, 2002.
- [76] H. Spanggaard and F. C. Krebs, "A brief history of the development of organic and polymeric photovoltaics," *Solar Energy Materials and Solar Cells*, vol. 83, no. 2-3, pp. 125–146, 2004.
- [77] A. Sandström, H. F. Dam, F. C. Krebs, and L. Edman, "Ambient fabrication of flexible and large-area organic light-emitting devices using slot-die coating," *Nature communications*, vol. 3, p. 1002, 2012.
- [78] T. Sekitani and T. Someya, "Stretchable, large-area organic electronics," *Advanced Materials*, vol. 22, no. 20, pp. 2228–2246, 2010.
- [79] S. Kim, H. Kwon, S. Lee, H. Shim, Y. Chun, W. Choi, J. Kwack, D. Han, M. Song, and S. Kim, "Low-power flexible organic light-emitting diode display device," *Advanced Materials*, vol. 23, no. 31, pp. 3511–3516, 2011.
- [80] M. A. Hupman, I. G. Hill, and A. Syme, "Preliminary characterization of the response of an organic field effect transistor to ionizing radiation," *Radiation Measurements*, vol. 118, pp. 31–35, 2018.
- [81] C. A. Mills, A. Intaniwet, M. Shkunov, J. L. Keddie, and P. J. Sellin, "Flexible radiation dosimeters incorporating semiconducting polymer thick films," in *Hard X-Ray, Gamma-Ray, and Neutron Detector Physics XI*, vol. 7449, p. 74491I, International Society for Optics and Photonics, 2009.

- [82] C. A. Mills, Y.-F. Chan, A. Intaniwet, M. Shkunov, A. Nisbet, J. L. Keddie, and P. J. Sellin, "Direct detection of 6 MV x-rays from a medical linear accelerator using a semiconducting polymer diode," *Physics in Medicine and Biology*, vol. 58, no. 13, p. 4471, 2013.
- [83] A. Intaniwet, C. A. Mills, M. Shkunov, H. Thiem, J. L. Keddie, and P. J. Sellin, "Characterization of thick film poly (triarylamine) semiconductor diodes for direct x-ray detection," *Journal of Applied Physics*, vol. 106, no. 6, p. 64513, 2009.
- [84] J. W. Kingsley, S. J. Weston, and D. G. Lidzey, "Stability of X-ray detectors based on organic photovoltaic devices," *IEEE Journal of Selected Topics in Quantum Electronics*, vol. 16, no. 6, pp. 1770–1775, 2010.
- [85] C. A. Mills, H. Al-Otaibi, A. Intaniwet, M. Shkunov, S. Pani, J. L. Keddie, and P. J. Sellin, "Enhanced x-ray detection sensitivity in semiconducting polymer diodes containing metallic nanoparticles," *Journal of Physics D: Applied Physics*, vol. 46, no. 27, p. 275102, 2013.
- [86] B. Fraboni, A. Ciavatti, F. Merlo, L. P. A. . . . , and U. 2012, "Organic Semiconducting Single Crystals as Next Generation of Low-Cost, Room-Temperature Electrical X-ray Detectors," *Wiley Online Library*.
- [87] R. Mohan, C. Chui, and L. Lidofsky, "Energy and angular distributions of photons from medical linear accelerators," *Medical Physics*, vol. 12, no. 5, pp. 592–597, 1985.
- [88] M. Soubra, J. Cygler, and G. Mackay, "Evaluation of a dual bias dual metal oxide-silicon semiconductor field effect transistor detector as radiation dosimeter," *Medical physics*, vol. 21, no. 4, pp. 567–572, 1994.
- [89] L. Archambault, T. M. Briere, F. Pönisch, L. Beaulieu, D. A. Kuban, A. Lee, and S. Beddar, "Toward a real-time in vivo dosimetry system using plastic scintillation detectors," *International Journal of Radiation Oncology* Biology* Physics*, vol. 78, no. 1, pp. 280–287, 2010.
- [90] L. Wootton, R. Kudchadker, A. Lee, and S. Beddar, "Real-time in vivo rectal wall dosimetry using plastic scintillation detectors for patients with prostate cancer," *Physics in Medicine & Biology*, vol. 59, no. 3, p. 647, 2014.
- [91] P. Carrasco, N. Jornet, O. Jordi, M. Lizondo, A. Latorre-Musoll, T. Eudaldo, A. Ruiz, and M. Ribas, "Characterization of the Exradin W1 scintillator for use in radiotherapy," *Medical physics*, vol. 42, no. 1, pp. 297–304, 2015.
- [92] A. R. Beierholm, C. F. Behrens, and C. E. Andersen, "Dosimetric characterization of the Exradin W1 plastic scintillator detector through comparison with an in-house developed scintillator system," *Radiation Measurements*, vol. 69, pp. 50–56, 2014.

- [93] S. R. Cowan, J. Wang, J. Yi, Y. J. Lee, D. C. Olson, and J. W. Hsu, “Intensity and wavelength dependence of bimolecular recombination in P3HT:PCBM solar cells: A white-light biased external quantum efficiency study,” *Journal of Applied Physics*, vol. 113, p. 154504, apr 2013.
- [94] F. Therriault-Proulx, L. Beaulieu, L. Archambault, and S. Beddar, “On the nature of the light produced within PMMA optical light guides in scintillation fiber-optic dosimetry,” *Physics in Medicine & Biology*, vol. 58, no. 7, p. 2073, 2013.
- [95] J. Boivin, S. Beddar, C. Bonde, D. Schmidt, W. Culberson, M. Guillemette, and L. Beaulieu, “A systematic characterization of the low-energy photon response of plastic scintillation detectors,” *Physics in Medicine and Biology*, vol. 61, pp. 5569–5586, aug 2016.
- [96] J. Boivin, S. Beddar, M. Guillemette, and L. Beaulieu, “Systematic evaluation of photodetector performance for plastic scintillation dosimetry,” *Medical physics*, vol. 42, no. 11, pp. 6211–6220, 2015.
- [97] W. J. Yoo, S. H. Shin, D. Jeon, S. Hong, S. G. Kim, H. I. Sim, K. W. Jang, S. Cho, and B. Lee, “Simultaneous measurements of pure scintillation and Cerenkov signals in an integrated fiber-optic dosimeter for electron beam therapy dosimetry,” *Optics express*, vol. 21, no. 23, pp. 27770–27779, 2013.
- [98] W. Parwaie, S. Refahi, M. Ardekani, and B. Farhood, “Different dosimeter-s/detectors used in small-field dosimetry: Pros and cons,” *Journal of Medical Signals & Sensors*, vol. 8, no. 3, p. 195, 2018.
- [99] P. E. Galavis, L. Hu, S. Holmes, and I. J. Das, “Characterization of the plastic scintillation detector Exradin W2 for small field dosimetry,” *Medical Physics*, vol. 46, pp. 2468–2476, may 2019.
- [100] K. A. Shukaili, S. Corde, M. Petasecca, V. Pereveratylo, M. Lerch, M. Jackson, and A. Rosenfeld, ““Characterization of ELEKTA SRS cone collimator using high spatial resolution monolithic silicon detector array”,” *Journal of Applied Clinical Medical Physics*, vol. 19, pp. 114–124, jul 2018.
- [101] M. Petasecca, M. K. Newall, J. T. Booth, M. Duncan, A. H. Aldosari, I. Fuduli, A. A. Espinoza, C. S. Porumb, S. Guatelli, P. Metcalfe, E. Colvill, D. Cammarano, M. Carolan, B. Oborn, M. L. F. Lerch, V. Perevertaylo, P. J. Keall, and A. B. Rosenfeld, “MagicPlate-512: A 2D silicon detector array for quality assurance of stereotactic motion adaptive radiotherapy,” *Medical Physics*, vol. 42, pp. 2992–3004, jun 2015.
- [102] G. Biasi, M. Petasecca, S. Guatelli, N. Hardcastle, M. Carolan, V. Perevertaylo, T. Kron, and A. B. Rosenfeld, “A novel high-resolution 2D silicon array detector for small field dosimetry with FFF photon beams,” *Physica Medica*, vol. 45, pp. 117–126, jan 2018.

- [103] I. Griessbach, M. Lapp, J. Bohsung, G. Gademann, and D. Harder, “Dosimetric characteristics of a new unshielded silicon diode and its application in clinical photon and electron beams,” *Medical Physics*, vol. 32, pp. 3750–3754, dec 2005.
- [104] N. Stansook, G. Biasi, K. Utitsarn, M. Petasecca, P. Metcalfe, M. Carolan, M. L. F. Lerch, V. L. Perevertaylo, T. Kron, and A. B. Rosenfeld, “2D monolithic silicon-diode array detectors in megavoltage photon beams: does the fabrication technology matter? A medical physicist’s perspective,” *Australasian Physical & Engineering Sciences in Medicine 2019 42:2*, vol. 42, pp. 443–451, feb 2019.
- [105] K. A. Shukaili, M. Petasecca, M. Newall, A. Espinoza, V. L. Perevertaylo, S. Corde, M. Lerch, and A. B. Rosenfeld, “A 2D silicon detector array for quality assurance in small field dosimetry: DUO,” *Medical Physics*, vol. 44, pp. 628–636, feb 2017.
- [106] M. Donetti, E. Garelli, F. Marchetto, A. Boriani, F. Bourhaleb, R. Cirio, I. Cornelius, S. Giordanengo, A. L. Rosa, U. Nastasi, and C. Peroni, “A method for the inter-calibration of a matrix of sensors,” *Physics in Medicine & Biology*, vol. 51, p. 485, jan 2006.
- [107] T. A. Simon, W. E. Simon, D. Kahler, J. Li, and C. Liu, “Wide field array calibration dependence on the stability of measured dose distributions,” *Medical Physics*, vol. 37, pp. 3501–3509, jul 2010.
- [108] S. Amerio, A. Boriani, F. Bourhaleb, R. Cirio, M. Donetti, A. Fidanzio, E. Garelli, S. Giordanengo, E. Madon, F. Marchetto, U. Nastasi, C. Peroni, A. Piermattei, C. J. S. Freire, A. Sardo, and E. Trevisiol, “Dosimetric characterization of a large area pixel-segmented ionization chamber,” *Medical Physics*, vol. 31, pp. 414–420, feb 2004.
- [109] D. A. Low, “Gamma Dose Distribution Evaluation Tool,” *Journal of Physics: Conference Series*, vol. 250, p. 012071, nov 2010.
- [110] C. Bassinet, C. Huet, S. Derreumaux, G. Brunet, M. Chéa, M. Baumann, T. Lacornerie, S. Gaudaire-Josset, F. Trompier, P. Roch, G. Boisserie, and I. Clairand, “Small fields output factors measurements and correction factors determination for several detectors for a CyberKnife® and linear accelerators equipped with microMLC and circular cones,” *Medical Physics*, vol. 40, p. 071725, jul 2013.
- [111] J. Fan, K. Paskalev, L. Wang, L. Jin, J. Li, A. Eldeeb, and C. Ma, “Determination of output factors for stereotactic radiosurgery beams,” *Medical Physics*, vol. 36, pp. 5292–5300, nov 2009.

- [112] H. Nusrat, G. Pang, S. B. Ahmad, B. Keller, and A. Sarfehnia, “Quantifying the impact of lead doping on plastic scintillator response to radiation,” *Medical Physics*, vol. 46, pp. 4215–4223, sep 2019.
- [113] I. Valitova, A. Hupman, I. G. Hill, and A. Syme, “Poly(3-hexylthiophene-2,5-diyl) based diodes for ionizing radiation dosimetry applications,” *Organic Electronics*, vol. 88, p. 105981, jan 2021.

Appendix A

Copyright Permission

A.1 Permission for: Radiation Induced Photocurrent in the Active Volume of P3HT/PCBM BHJ Photodiodes

The publisher of this manuscript is Elsevier:

Organic Electronics 85 (2020) 105890



Contents lists available at [ScienceDirect](#)

Organic Electronics

journal homepage: <http://www.elsevier.com/locate/orgel>



Radiation induced photocurrent in the active volume of P3HT/PCBM BHJ photodiodes




Michael A. Hupman^a, Irina Valitova^a, Ian G. Hill^a, Alasdair Syme^{a,b,c,*}


^a Department of Physics and Atmospheric Science, Dalhousie University, Halifax, Nova Scotia, B3H 4R2, Canada

^b Department of Radiation Oncology, Dalhousie University, Halifax, Nova Scotia, B3H 4R2, Canada

^c Department of Medical Physics, Nova Scotia Health Authority, QEII Health Science Centre, Halifax, Nova Scotia, B3H 1V7, Canada

Elsevier does not require written permission for use in the thesis. The following is from their website:

→  elsevier.com/about/policies/copyright/permissions

 **ELSEVIER** About Elsevier Products & Solutions Services Shop & Discov

Permission guidelines ScienceDirect content ClinicalKey content Tutorial videos Help and support

Can I use material from my Elsevier journal article within my thesis/dissertation? –

As an Elsevier journal author, you have the right to Include the article in a thesis or dissertation (provided that this is not to be published commercially) whether in full or in part, subject to proper acknowledgment; see the [Copyright page](#) for more information. **No written permission from Elsevier is necessary.**

This right extends to the posting of your thesis to your university's repository provided that if you include the published journal article, it is embedded in your thesis and not separately downloadable.

A.2 Permission for: Method for the Differentiation of Radiation-Induced Photocurrent from Total Measured Current in P3HT/PCBM BHJ Photodiodes

The publisher of this manuscript is Elsevier:

MethodsX 7 (2020) 101125



ELSEVIER

Contents lists available at ScienceDirect

MethodsX

journal homepage: www.elsevier.com/locate/mex



Method Article

Method for the differentiation of radiation-induced photocurrent from total measured current in P3HT/PCBM BHJ photodiodes




Michael A Hupman^{a,#,\$}, Irina Valitova^{a,#,\$}, Ian G Hill^{a,#,\$},
Alasdair Syme^{a,b,c,#,\$,*}


^a Department of Physics and Atmospheric Science, Dalhousie University, Halifax, Nova Scotia B3H 4R2, Canada

^b Department of Radiation Oncology, Dalhousie University, Halifax, Nova Scotia B3H 4R2, Canada

^c Department of Medical Physics, Nova Scotia Health Authority, QEII Health Science Centre, Halifax, Nova Scotia B3H 1V7, Canada

Elsevier does not require written permission for use in the thesis. The following is from their website:

→  elsevier.com/about/policies/copyright/permissions

 **ELSEVIER** [About Elsevier](#) [Products & Solutions](#) [Services](#) [Shop & Discov](#)

[Permission guidelines](#) [ScienceDirect content](#) [ClinicalKey content](#) [Tutorial videos](#) [Help and support](#)

Can I use material from my Elsevier journal article within my thesis/dissertation? –

As an Elsevier journal author, you have the right to Include the article in a thesis or dissertation (provided that this is not to be published commercially) whether in full or in part, subject to proper acknowledgment; see the [Copyright page](#) for more information. **No written permission from Elsevier is necessary.**

This right extends to the posting of your thesis to your university's repository provided that if you include the published journal article, it is embedded in your thesis and not separately downloadable.

A.3 Permission for: Fabrication and Characterization of a Stemless Plastic Scintillation Detector

The publisher of this manuscript is Wiley:

► [Med Phys.](#) 2020 Nov;47(11):5882-5889. doi: 10.1002/mp.14475. Epub 2020 Oct 6.

Fabrication and characterization of a stemless plastic scintillation detector

Michael A Hupman ¹, Thalal Monajemi ^{1 2 3}, Irina Valitova ¹, Ian G Hill ¹, Alasdair Syme ^{1 2 3}

Affiliations — collapse

Affiliations

- 1 Department of Physics and Atmospheric Science, Dalhousie University, Halifax, Nova Scotia, B3H 4R2, Canada.
- 2 Department of Radiation Oncology, Dalhousie University, Halifax, Nova Scotia, B3H 4R2, Canada.
- 3 Department of Medical Physics, Nova Scotia Health Authority, QEII Health Science Centre, Halifax, Nova Scotia, B3H 1V7, Canada.

PMID: 32966652 DOI: [10.1002/mp.14475](#)

FULL TEXT LINKS



ACTIONS



SHARE



PAGE NAVIGATION

< Title & authors

Wiley does not require written permission for use in the thesis. The following is from their website:

wiley.com/network/researchers/latest-content/how-to-clear-permissions-for-a-thesis-or-dissertation

WILEY

THE WILEY NETWORK | INSTRUCTORS & STUDENTS | JOURNAL EDITORS | LIBRARIANS | PROFESSIONALS | **RESEARCHERS** | SOCIETY LEADERS

TOPICS ▾

CONTENT TYPE ▾

Search Researchers



Do I need to request permission to use my own work as my dissertation?

If you are the author of a published Wiley article, you have the right to reuse the full text of your published article as part of your thesis or dissertation. In this situation, **you do not need to request permission from Wiley for this use.**

If your institution still requires a reuse license in this case, follow the steps below to request your license via RightsLink.